Microstructure and mechanical properties of face-centered cubic high/medium entropy alloys: From a viewpoint of heterogeneity on atomic-scale

2021

Shuhei Yoshida

Microstructure and mechanical properties of

face-centered cubic high/medium entropy alloys:

From a viewpoint of heterogeneity on atomic-scale

By

Shuhei Yoshida

A Dissertation Submitted to Kyoto University for

Doctor of Philosophy (Engineering)

Department of Materials Science and Engineering

Kyoto University

2021

To Rena and Yu

Table of Contents

Chapter 1: Introduction to high/medium entropy alloys

1.1. Definition of high entropy alloys

The exploration of new materials is always of great significance for the progress of materials science and the ecological use of limited resources on the earth. The design of conventional alloys such as Fe-alloys and Al-alloys is based on one principal element with the addition of relatively small amounts of some minor elements for modifying its microstructure and properties. In other words, the conventional studies of metallic materials have been mainly focusing on the edge part (corner) of equilibrium phase diagrams. In contrast, the emergence of high entropy alloys (HEAs), proposed by Yeh *et al*. [1] and Cantor *et al*. [2] independently in 2004, has vastly expanded the possibility of new multi-component metallic alloys and aroused the curiosity of many materials scientists in recent years [3–10]. HEAs are normally defined as the alloys composed of five or more principal elements with concentrations of 5 to 35 at. % and corresponding to the center parts of phase diagrams as illustrated in **figure 1.1**. The origin of the name, "*high entropy*" alloys is their large configurational entropy defined by the following equation.

$$S^{\text{config}} \approx -R \sum_i c_i \ln c_i \tag{1.1}$$

where R is the gas constant, and c_i is the concentration of constituent elements. For instance, the configurational entropy of an equiatomic HEA with a single-phase composed of five elements is calculated as $1.6R$, which is much larger than that of conventional dilute alloys with $S^{\text{config}} \approx 0$.

HEAs have been reported to possess many promising mechanical properties as structural materials applicable at a wide range of temperature, such as excellent cryogenic strength and toughness [11,12], outstanding wear resistance [13], and excellent thermal
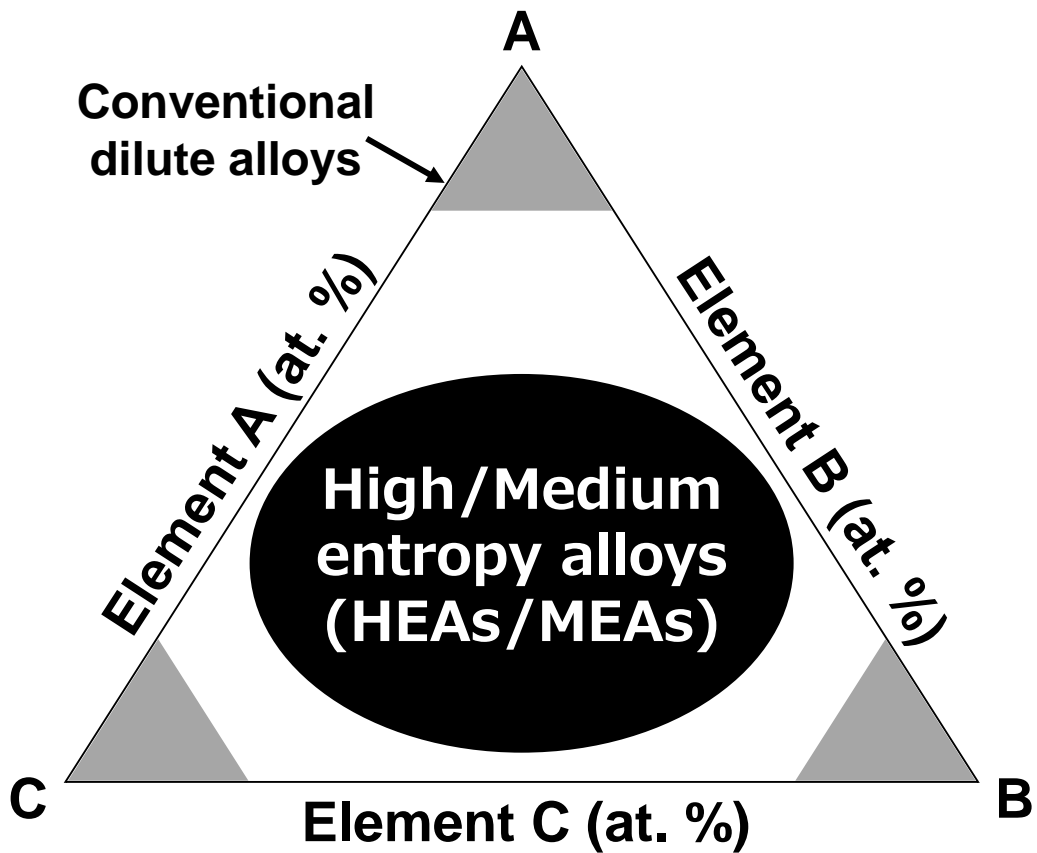
Figure 1.1: Example of a phase diagram of (pseudo) ternary system showing the concentration regions of conventional dilute alloys at the corners and HEAs/MEAs at the center parts.

stability [14]. Generally, it has been believed that these outstanding properties in HEAs are related to the following so-called "core effects" of HEAs, which characterize the nature of HEAs [3]: (1) high entropy effect, (2) cocktail effect, (3) sluggish diffusion kinetics, and (4) severe lattice distortion effect. In the following section, the current understanding and issues of each effect are reviewed.

1.2. Core effects

1.2.1. High entropy effect

In HEAs, it has been said that single-phase crystal structure such as simple face-centered cubic (FCC) and body-centered cubic (BCC) structure is stabilized owing to the large configuration entropy of HEAs, and single-phase solid solution could be easily obtained by increasing the number and concentration of alloying elements. The Gibbs' free energy of systems, G, at finite temperature, T, is generally defined by

$$G = H - TS \tag{1.2}$$

where H and S are mixing enthalpy and entropy of the systems. If S is large, the effect of the entropy term, $-TS$, in **eq. (1.2)** becomes dominant at high temperatures and reduces
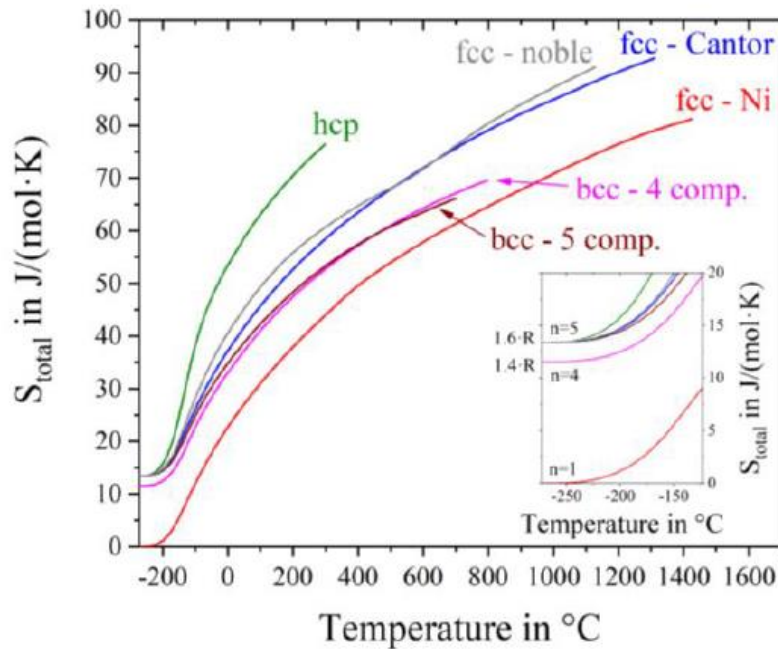
Figure 1.2: Experimentally determined total entropy, S_{total}, as a function of temperature in pure Ni (fcc-Ni), $Co_{22}Cr_{24}Fe_{22}Mn_{11}Ni_{21}$ HEA (fcc-Cantor), $Au_{16}Cu_{17}Ni_{17}Pd_{34}Pt_{16}$ (fcc-noble), $Mo_{27}Nb_{27}Ta_{23}W_{23}$ (bcc-4 comp.), $Hf_{21}Mo_{20}Nb_{21}Ti_{17}Zr_{21}$ (bcc-5 comp.), and $Ho_{18}Dy_{16}Y_{28}Gd_{20}Tb_{18}$ (hcp) [15]. n and R are the numbers of alloying elements and the gas constant, respectively.

G leading to the stabilization of single-phase microstructure. The above explanation has been frequently used to emphasize the effect of entropy in HEAs in many reports.

However, several recent reports have cast doubt on the role of entropy. Haas *et al*. [15] directly measured the entropy depending on the temperature in pure Ni and various single-crystalline HEAs with FCC, BCC, and HCP single-phase microstructure as presented in **figure 1.2**. Generally, entropy in metals can be separated into configurational entropy and thermal entropy. The former is approximated by **eq. (1.1)** and independent of temperature. The latter reflects the contribution of phonons and electrons and is temperature-dependent. They found that the contribution of thermal entropy on total entropy is several times larger than that of the configurational entropy at high temperature in all the materials regardless of the concentration of alloying elements. Although it is true that the configurational entropy slightly contributes to the reduction of total free energy, their results imply that the enthalpy term, *H*, in **eq. (1.2)** also plays an important role. In another study done by Senkov *et al*. [16] reported that complex multiphase structures including intermetallics could be more likely to form with increasing the number of alloying elements based on their calculation results of a large-scale thermodynamical screening with CALPHAD method. All the results explained above suggest that the high entropy effect can be true only when the mixing enthalpy is close to 0 (i.e., ideal solid solutions) [17]. This is exactly the same as the knowledge of thermodynamics in conventional dilute alloys.

1.2.2. Sluggish diffusion effect

The diffusion kinetics of HEAs (3) was firstly reported by Tsai *et al*. [18] in a CoCrFeMnNi equi-atomic HEA. They compared its activation energy normalized by

melting temperature for lattice diffusion with those of pure metals and austenitic stainless steels. Then, they concluded that the diffusion kinetics in the HEA is sluggish since the activation energy normalized by melting temperature was higher than those of pure metals and austenitic stainless steels. Dąbrowa *et al*. [19] also recently confirmed similar diffusion kinetics in Al-Co-Cr-Fe-Ni HEAs. However, the activation energy of diffusion in HEAs before normalized by melting temperature is comparable to those in conventional alloys and pure metals. Thus, the existence of sluggish diffusion in HEAs has been under intensive debate.

Sugita *et al*. [20] experimentally measured the average formation and migration energy of vacancies in CoCrFeMnNi HEA. Generally, the formation and migration energy of metals and alloys are proportional to their melting temperature. According to their results, the energy values in the HEA were along the same trend of conventional metals (**Figure 1.3 (a)**). Abe [17] also reported very similar results obtained by thermodynamics calculation.
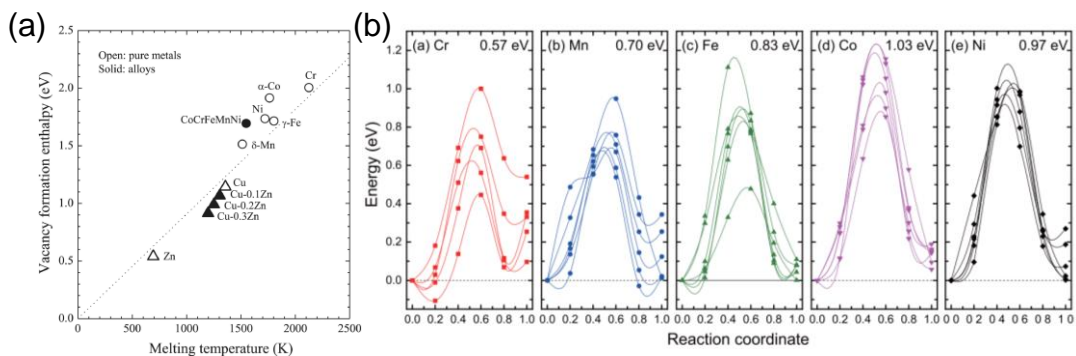
Figure 1.3: (a) Relationship between melting temperature and vacancy formation energy of CoCrFeMnNi HEA determined by positron annihilation spectroscopy, plotted together with various metals and alloys for comparison [20]. (b) Vacancy migration energy of Cr, Mn, Fe, Co, and Ni in CoCrFeMnNi HEA calculated by spin-polarized DFT, in which each curve was obtained at a different lattice site with different local chemical environment [22].

6

Despite that the above results seemingly deny the existence of sluggish diffusion in HEAs, the absolute values of diffusivity in HEAs are clearly smaller than conventional materials [18,21]. One key may be the variation of the local potential energy of vacancies. Tsai *et al*. [18] employed a simple chemical model to explain that the variation of the potential energy can be very large in HEAs, resulting in difficulty in vacancy migration depending on the local chemical environment. Mizuno *et al*. [22] calculated the vacancy migration energy in CoCrFeMnNi HEA by using density functional theory (DFT) and also showed that vacancy migration energy varied largely depending on the local chemical environment (**Figure 1.3 (b)**). These facts imply that vacancies can be trapped at specific sites with low potential energy leading to slower diffusion kinetics compared with conventional materials. Further investigation is necessary to clarify this issue.

1.2.3. Severe lattice distortion effect

The crystal lattice of HEAs has been believed to be severely distorted owing to the difference in the atomic size of constituent elements as illustrated in **figure 1.4**. Oh *et al*. [23,24] investigated lattice distortion by using extended X-ray absorption fine structure (EXAFS) and DFT and confirmed that the variation of bond length in CoCrFeMnNi HEA is much larger than that in conventional materials, resulting in high atomic pressure and severe lattice distortion. In addition, they also confirmed that the severe lattice distortion is strongly correlated with the difference in electronegativity of the constituent elements. Such a lattice distortion state should interact with dislocations in crystal lattices and contribute to strengthening. However, due to the lack of systematic study, the underlying physics on the effect of severe lattice distortion effect on the strength of HEAs is unclear at this moment. This issue will be solved in the proceeding chapters.
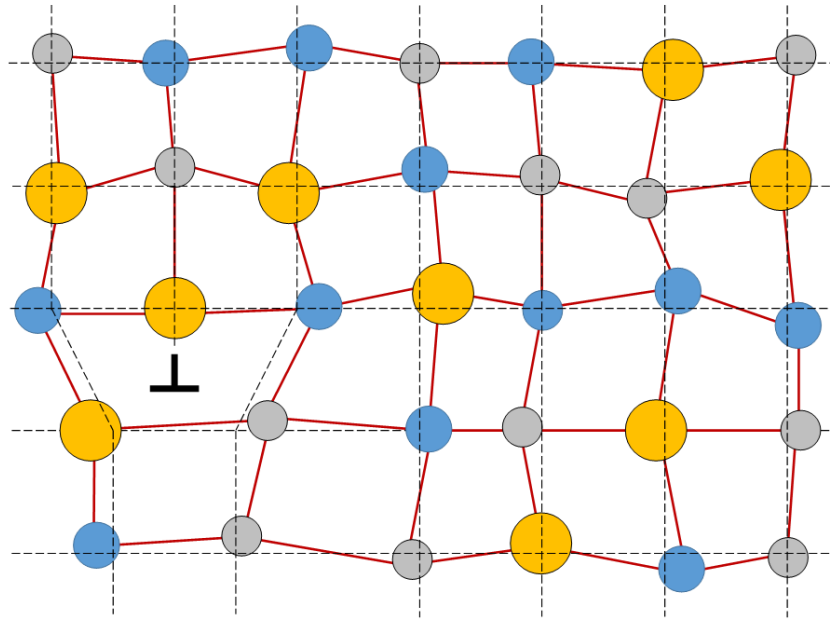
Figure 1.4: Schematic illustrations of the locally-distorted lattice in multicomponent solid solution alloys with a dislocation. The lattice expressed by dotted lines is the average lattice determined by the mean lattice constant and crystal structure.

1.2.4. Cocktail effect

As the same as conventional solid solution alloys, the properties of HEAs can be modified by mixing with additional alloying elements. This is the so-called Cocktail effect. For example, to realize light-weighted HEAs, light elements such as Al have been added to FCC HEAs [14,25–27]. Li *et al*. [28–31] adjusted adjusting the concentration of Mn, Ni, C in a Co-Cr-Fe-Mn-Ni-C HEA and reported that martensitic phase transformation happened (e.g., **figure 1.5**) to result in a good strength-ductility balance. They attributed it to the lowered stacking fault energy (SFE) of the corresponding alloys. Although these results can be explained by the cocktail effect, one should be always cautious that, in HEAs, there can be new phenomena other than the properties predicted by the simple rule of mixture.
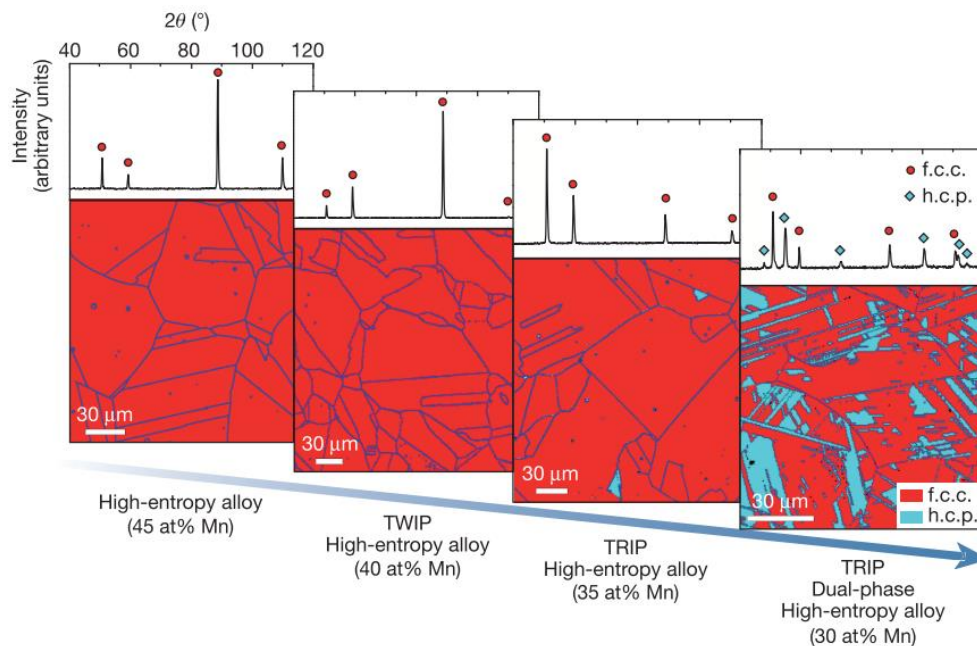
Figure 1.5: X-ray diffraction profiles and electron back-scattering diffraction (EBSD) phase map of $Fe_{(80-x)}Mn_xCo_{10}Cr_{10}$ (x = 45, 40, 35, and 30 at.%) HEA [28].

1.3. Medium entropy alloys

In the past few years, the medium entropy alloys (MEAs), which are defined as the alloys composed of two to four principal elements in equi-atomic compositions, have also gotten attention. Wu *et al*. [32] fabricated the subsystems of CoCrFeMnNi HEA (e.g., CoCrFeNi, CoCrNi, and FeNi) and investigated their phase stability and recrystallization behavior. They found that the subsystems alloys also exhibit FCC single-phase microstructure at high temperature as the same as the HEA. As pointed out in Section 1.2.1, this might be because the chemical interaction among the constituent elements was weak (i.e., near-zero mixing enthalpy). Gludovatz *et al*. [33] measured the mechanical properties of CoCrNi MEA, and they found that CoCrNi MEA was superior to CoCrFeMnNi HEA and various classes of materials in terms of the strength-ductility balance and the fracture toughness as shown in **figure 1.6**. At this moment, the reason for

9

the excellent mechanical properties is the low SFE of the CoCrNi MEA, which has been

believed to be responsible for deformation twinning and deformation-induced martensitic

phase transformation [34,35]. By adjusting the chemical composition of the CoCrNi

MEA, it is possible to change the SFE and deformation mechanism [36–38] as in the case

of HEAs and other FCC materials. In addition, the effect of severe lattice distortion has

been expected to be larger in the CoCrNi MEA than that in other HEAs [39]. Thus, higher

lattice friction stress may contribute to the mechanical properties (This will be discussed

in Chapters 2 and 3 in detail.). Another feature is the diffusion kinetics in MEAs. Jin *et*

al. [21] showed that the diffusion kinetics in various MEAs was also sluggish. Above all,

many of the characteristics of MEAs are quite similar to HEAs. Therefore, although the
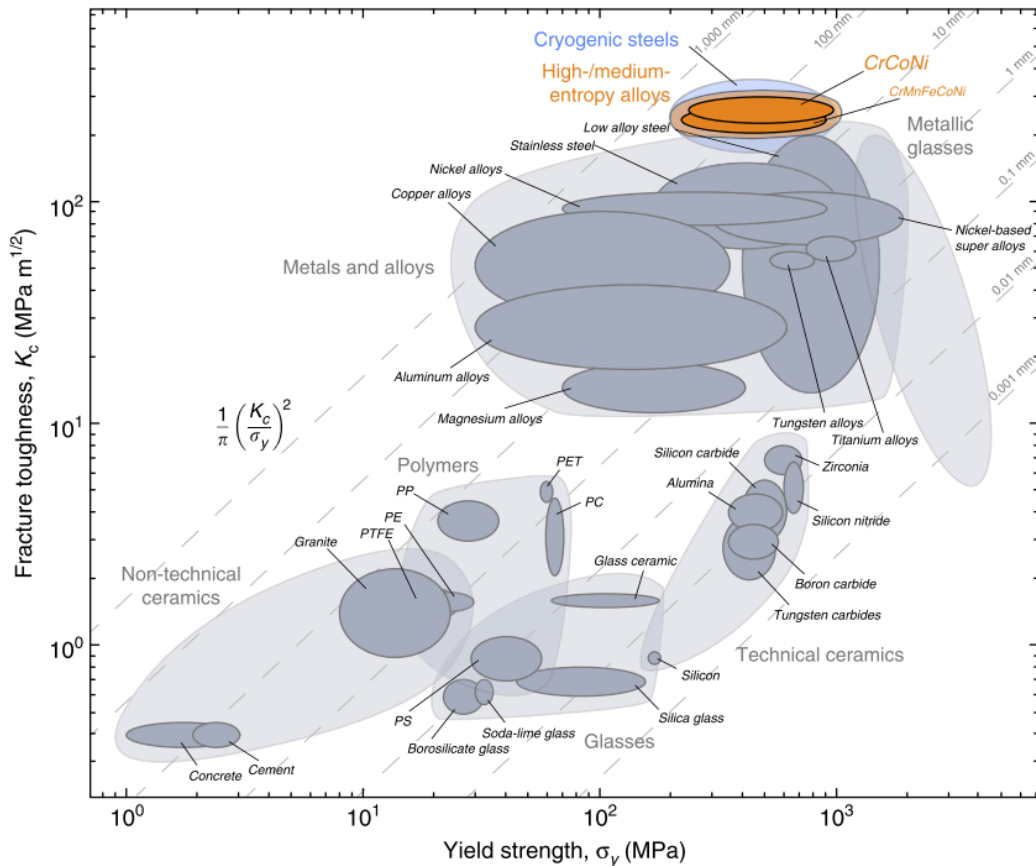
Figure 1.6: Ashby map of fracture toughness (K_c) v. s. yield strength (σy) of the CoCrNi MEA, CoCrFeMnNi HEA, and various classes of materials [33].

number of alloying elements is different, both HEAs and MEAs are considered to be essentially the same class of materials, and the same physics is expected to be behind the characteristics.

1.4. Key issues and the main focus of this dissertation

Despite that the term "entropy" is included in the name of HEAs and MEAs, the entropy of the materials (i.e., number of alloying elements) does not explain their characteristics, but the combination of alloying elements can play a more important role. However, due to the lack of systematic research on the microstructure and mechanical properties, the essential nature of HEAs and MEAs is still unclear. By deepening the understanding of the nature of HEAs and MEAs beyond the core effects, a universal framework that is capable of explaining the physical properties of various metals and alloys regardless of solute concentration can be realized. Thus, in this dissertation, various HEAs, MEAs, other high-alloy systems, dilute systems, and pure metals having FCC single-phase are systematically compared particularly focusing on their microstructure and mechanical properties, and the essential nature of HEAs and MEAs is clarified.

1.5. Structure of this dissertation

The structure of this dissertation is divided as follows. In Chapter 1, the present chapter, previous studies were briefly reviewed, and the key issues to be solved and the focus of this dissertation were explained. In Chapter 2, the friction stress and Hall-Petch relationship of various HEAs and MEAs with FCC single-phase are investigated, and the strengthening mechanism in HEAs and MEAs are clarified by comparing experimental

data and some theoretical models. In Chapter 3, characteristic deformation microstructure evolution and its relation to macroscopic deformation behavior are investigated, and the reasons for the superior mechanical properties of FCC HEAs and MEAs are revealed. In Chapter 4, the static recrystallization behavior of FCC HEAs and MEAs processed by severe plastic deformation (SPD) and subsequent annealing is investigated, and the characteristics of recrystallization in HEAs and MEAs are discussed. In addition, fully-recrystallized ultrafine-grained (FRex-UFG) microstructures having the smallest mean grain size ever reported is achieved. In Chapter 5, all the key results in this dissertation are summarized, and the essential nature of HEAs and MEAs is discussed. Finally, future directions of research are presented.

Chapter 2: Effect of elemental combination on Friction stress and Hall-Petch relationship

2.1. Introduction

Severe lattice distortion has been said to be the main reason for the high strength of HEAs [39,40]. In highly-concentrated systems including MEAs and HEAs, the crystal lattice is significantly (and heterogeneously) distorted everywhere because all constituent elements have different atomic radii. Consequently, the local position of each atom may be largely shifted from the average lattice position determined from the average lattice constant and crystal structure, depending on the local arrangement of elements, so that different lattice distortions arise locally [24]. This lattice distortion state has been confirmed by both experimental and calculation studies. Okamoto *et al*. [41] employed synchrotron X-ray diffraction and a first-principle calculation to determine MSAD as a parameter for evaluating the level of the local lattice distortion. They predicted that Cr and Mn made MSAD large, which implied that these two elements had great impacts on the strengthening of Ni-based FCC solid solution alloys. Oh *et al*. [23] investigated the distribution of atomic bonding length by combining the first-principle calculation with X-ray absorption fine structure spectroscopy (XAFS). Their results suggested that Cr and Mn had wider bonding length distributions than those of other constituent elements in the CoCrFeMnNi HEA. Therefore, it is possible to qualitatively understand that Cr act as a large-sized atom in Ni-containing FCC equi-atomic alloys such as CoCrFeMnNi HEA, and the concentration of Cr has a huge impact on the strength of such alloy systems [23,41,42]. However, a quantitative understanding of the severe lattice distortion effect on the strength of FCC HEAs and MEAs is lacking. One of the reasons for making it difficult to deal with the effect of lattice distortion is that there has been no theoretical model effectively explaining the strength of HEAs.

For conventional binary alloys, Fleisher [43,44] and Labusch [45] theoretically formulated the solid solution strengthening effect. Especially, Labusch concerned relatively concentrated systems having solute concentrations up to 20 at. % based on the statistical theory that had been used to understand the superconductivity of materials. Their models have been validated by countless experimental data [46], and have sometimes been modified to apply to dilute multicomponent alloys [47].

Recently, Wu *et al*. [48] tried to apply the Labusch model to medium entropy alloys (MEAs), which are defined as the alloys composed of four or fewer principal elements with equimolar or near-equimolar concentration. They arbitrarily distinguished solutes and solvents in the MEAs that were subsystems of CoCrFeMnNi HEA and assumed that the strength of the alloys could be expressed by a linear combination of the Labusch model. Finally, they compared the calculated strength with their experimental data and found that the strength could not be perfectly explained by the Labusch model.

Several other attempts have been made to establish a new model that can predict the strength of high-alloy systems like HEAs and MEAs. Okamoto *et al*. [41] found a correlation between the mean square atomic displacement (MSAD) (lattice distortion in other words) and the strength of subsystems of the CoCrFeMnNi HEA, by using the first-principle calculation. Chen *et al*. [40] also obtained a similar correlation in BCC HEAs and MEAs. Although some of the previous studies successfully predicted the strength of HEAs and MEAs, underlying physics including the contribution of lattice distortion had not been fully understood yet due to the lack of experimental data.

In the present study, the detailed strengthening mechanism and essential nature of high-alloy systems such as HEAs and MEAs are studied by experimentally investigating the effect of elemental combinations on the friction stress and Hall-Petch relationship for

various MEAs. Fully-recrystallized specimens of various kinds of MEAs having FCC single-phase with wide ranges of different mean grain sizes were fabricated by the use of high-pressure torsion (HPT) and subsequent annealing processes. Tensile tests are performed at room temperature, and precise Hall-Petch relationships are systematically obtained for the alloys. The friction stresses of the alloys are evaluated from the obtained Hall-Petch relationship [42]. Afterward, the Labusch model for solution hardening is modified to establish an effective model for predicting the strength of high-alloy systems, and the experimental data are compared with the model. Finally, strengthening mechanisms that are responsible for the high strength of high-alloy systems such as HEAs and MEAs are discussed.

2.2. Materials and methods

2.2.1. Starting materials

Five equi-atomic subsystems of the CoCrFeMnNi HEA, i.e., CoCrFeNi, CoFeMnNi, CoFeNi, CoMnNi, FeMnNi, CoCrNi, and Ni-40Co ($Ni_{60}Co_{40}$) (at. %)as well as three non-equi-atomic subsystems $(CoNi)_{(100-x)}Cr_x$ (x = 5.0, 20 at. %) and $Co_{20}(CrNi)_{80}$ (at. %) were selected as the starting materials for the experiments carried out in the present study. Ingots of the alloys were produced by arc-melting of constituent elements with a purity higher than 99.9 wt. % in a water-cooled copper mold under a protective Ar atmosphere. Since Mn was oxidized easily, the pieces of pure Mn were cleaned in a solution of 25 vol. % nitric acids and 75 vol. % C_2H_5OH at room temperature just before melting. Additionally, because of the high vapor pressure of Mn, pure Mn was sandwiched between the pieces of other constituent metals to minimize evaporation. Even after such procedures, there was a loss of Mn during melting, so that an extra amount of

Mn (+ 5.0 wt. %) was added to compensate for the weight loss in melting and casting of each Mn-containing alloy. The arc-melted buttons were flipped and re-melted at least five times to improve compositional homogeneity.

The arc-melted buttons were also subsequently cold-rolled by 80 - 90% reduction in thickness and homogenized (fully-recrystallized) at 1200 ºC for 24 h under a vacuum environment (~ 8.0×10^{-4} Pa) using a vacuum tube furnace to remove macro-segregations in the alloys.

2.2.2. Chemical composition analysis

Energy dispersive X-ray (EDX) spectroscopy was employed to analyze elemental distributions in the homogenized specimens. The specimens were cut from the homogenized materials by a wire cutting machine (Brother, HS-70A) into a dimension of 10 mm (in length) $\times$ 10 mm (in width) $\times$ 1 mm (in thickness). Afterward, the specimens were mechanically polished by 1000 - 4000 grid-sized fine sandpapers and then 1 - 3 μm diamond pastes to achieve mirror-like surfaces.

EDX measurements were performed in a field-emission scanning electron microscope (FE-SEM) (JEOL, JSM-7100) equipped with an EDX spectrometer. The working distance was set at 15 mm for the EDX measurements. Line-scanning along the normal direction (ND) of the rolled sheets was applied to analyze the chemical composition of the alloys. The acceleration voltage in SEM was maintained at 25 kV.

2.2.3. Deformation and annealing

Disc-shaped specimens with a diameter of 10 mm and a thickness of 0.80 mm for HPT were prepared by cutting the homogenized materials. The HPT process was

performed at room temperature under a pressure of 6.0 GPa at a speed of 0.20 rpm (rotation per minute). The total rotation angle applied was 1800º (five rotations). The shear strain, γ, applied to the disc specimens during the HPT process can be calculated as

$$\gamma = \frac{2\pi r}{t} N,$$ (2.1)

where r is the radial position in the disc, N is the number of rotations, and t is the thickness of the disc. Based on **eq. (2.1)**, the maximum shear strain applied to the materials by five rotations of HPT can be as large as $\gamma = 196$.

After the heavy deformation by HPT, specimens were annealed at various temperatures ranging from 700 ºC to 1100 ºC for various periods ranging from 20 s to 7.2 ks.

2.2.4. Phase analysis of annealed specimens

X-ray diffraction (XRD) technique was used to investigate the crystal structure of the specimens after HPT and subsequent annealing. The specimens for the XRD measurement were mechanically polished by 1000 - 4000 grid sized fine sandpapers and then 1 - 3 μm diamond pastes to achieve mirror-like surfaces.

The XRD measurements were performed using PANalytical-X'Pert PRO with Cu-Kα radiation (wavelength: $\lambda = 1.540598$ nm). The tube voltage and tube current were set at 45 kV and 40 mA, respectively. XRD data were collected over a 2θ angle range of 30 - 100 º at a scanning rate of 0.013 º s⁻¹.

2.2.5. Microstructural characterizations

Specimens for microstructural observation were mechanically polished by using 1000 – 4000 grid sized fine sandpapers and then diamond pastes (1.0 – 3.0 μm) to achieve mirror-like surfaces. Afterward, the specimens were electrically polished in a solution of 10 vol. % $HclO_4$ and 90 vol. % C_2H_5OH at 30 V for 15 s at room temperature.

Microstructural observations were performed by using an FE-SEM (JEOL, JSM-7100 / 7800F) operated at 25 kV and equipped with backscattered electron (BSE) and electron backscattering diffraction (EBSD) detectors. Observations were carried out on the section perpendicular to the normal direction of the disc at the position around 3.0 mm from the center of the disc specimens. The observed position corresponded to the gauge part of the tensile specimens. The working distance was set at 3.0 – 10 mm for BSE and 15 mm for EBSD. The data collection of EBSD was conducted using the software produced by TSL solution (TSL-OIM data collection, analysis ver. 5.31), and the OIM analysis software (Tex SEM Laboratories, ver. 7.0) was used to analyze the collected data. Grain sizes of the specimens were determined by the line intercept method on SEM-BSE images and EBSD grain boundary maps showing high-angle grain boundaries with misorientations larger than 15°.

2.2.6. Tensile tests

Tensile tests were performed on a universal tensile test machine (SHIMADZU, AG-100 kN Xplus) at room temperature at a quasi-static strain rate of 8.3×10^{-4} s^{-1} for characterizing the mechanical properties of the alloys. Small-sized tensile specimens with a gauge length of 2.0 mm and a gage cross-section of 1.0×0.50 mm were cut from the annealed specimens having FCC single-phase so that the center of the gauge part

coincided with the position at a radial distance of 3.0 mm from the center of the disc samples. It was already confirmed in the previous study that the small-sized specimens could give reliable stress-strain behaviors equivalent to those obtained from standard size specimens of the same materials [42]. Due to the difficulty in attaching the extensometer or strain gauge on the small-sized specimens, the displacement of the gage section was precisely measured by a CCD video camera extensometer (SVS625MFCP), and the strain was calculated by the use of a digital image correlation (DIC) technique. Surfaces of all the tensile specimens were painted with white and black inks to produce a random dot pattern (speckle pattern) acting as markers easily tracked during deformation for the DIC analysis. In-situ DIC measurements were achieved from a set of strain snapshots collected automatically by using Vic-2D software [49].

2.3. Results

2.3.1. Chemical composition of homogenized materials

Chemical compositions of the as-homogenized alloys experimentally measured by SEM-EDX are summarized in **table 2.1**.

Table 2.1: Chemical compositions of the as-homogenized alloys experimentally studied in this work. Compositions were measured by means of SEM-EDX.

Alloy	Co [at. %]	Cr [at. %]	Fe [at. %]	Mn [at. %]	Ni [at. %]
Ni-40Co	40.3 $\pm$0.18	-	-	-	Bal.
FeMnNi	-	-	33.8 $\pm$0.26	33.0 $\pm$0.80	Bal.
CoFeNi	33.6 $\pm$0.45	-	33.8 $\pm$0.07	-	Bal.
CoMnNi	33.6 $\pm$0.71	-	-	33.2 $\pm$0.78	Bal.
CoCrNi	33.4 $\pm$0.38	33.7 $\pm$0.10	-	-	Bal.
$(CoNi)_{80}Cr_{20}$	39.9 $\pm$0.39	20.3 $\pm$0.23	-	-	Bal.
$(CoNi)_{95}Cr_5$	47.2 $\pm$0.40	5.2 $\pm$0.16	-	-	Bal.
CoFeMnNi	25.1 $\pm$0.80	-	24.9 $\pm$0.35	24.8 $\pm$0.86	Bal.
CoCrFeNi	25.2 $\pm$0.43	25. $\pm$0.59	24.8 $\pm$0.25	-	Bal.
$Co_{20}(CrNi)_{80}$	19.9 $\pm$0.31	40.7 $\pm$0.25	-	-	Bal.

It was confirmed that the measured values in the table were very close to the designed compositions, and the standard deviations of the concentrations were small enough to neglect the segregation of the elements.

2.3.2. Microstructures after annealing process

Figure 2.1 (a – j) represent the XRD profiles of the equi-atomic and non-equi-atomic subsystems of CoCrFeMnNi HEA processed by HPT and subsequently annealed at various temperature (shown in **figure 2.1**) for 1.2 ks followed by water-quenching. All the specimens except for $Co_{20}(CrNi)_{80}$ showed only diffraction peaks of FCC single-phase without any diffuse scattering or super-lattice reflection. An extra peak was observed in $Co_{20}(CrNi)_{80}$ annealed at temperatures ranging from 750°C to 800 °C indicated by an arrow in **figure 2.1 (j)**.
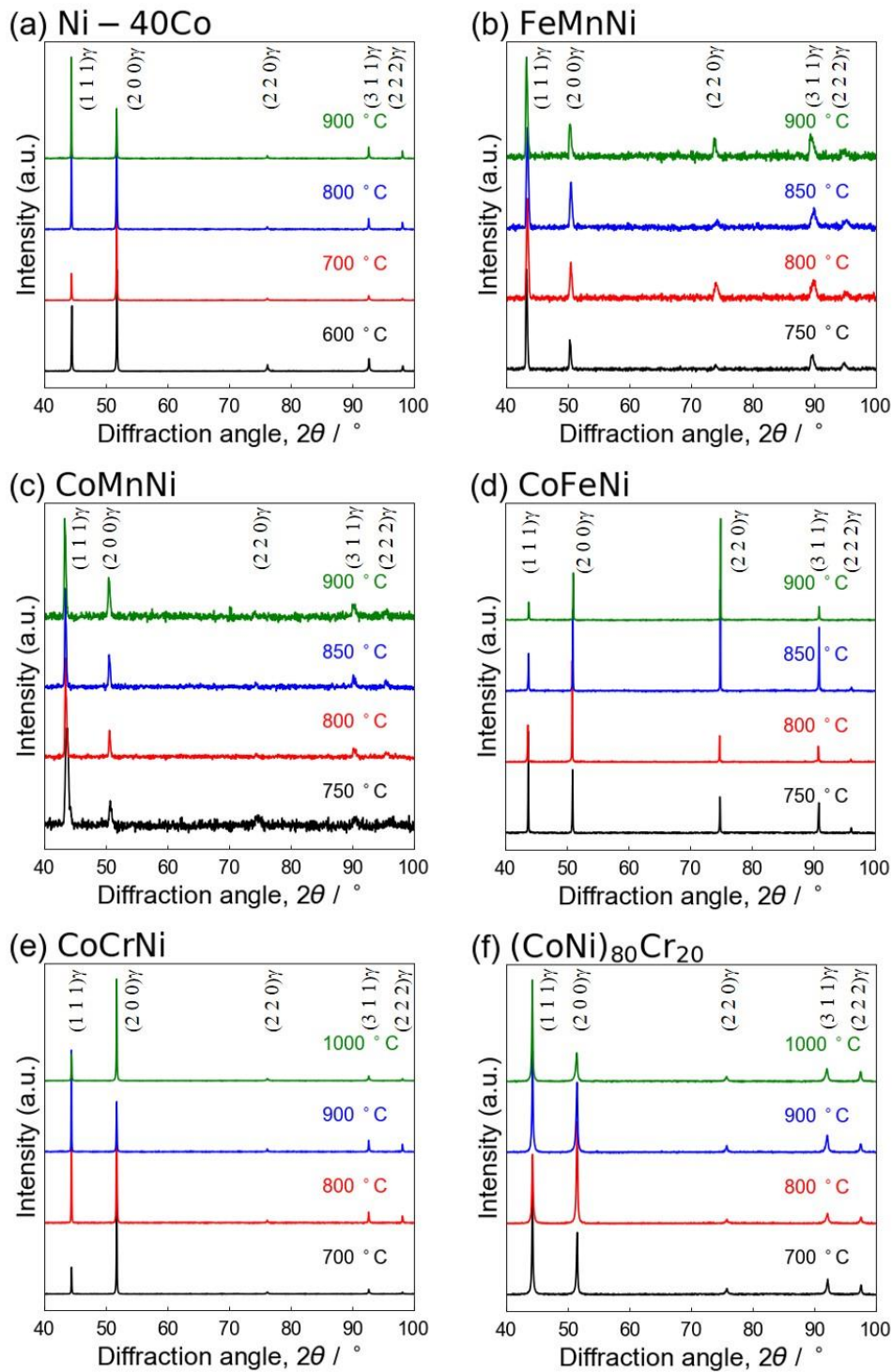
Figure 2.1: XRD profiles of the specimens of (a) Ni-40Co, (b) FeMnNi, (c) CoMnNi, (d) CoFeNi, (e) CoCrNi, (f) $(CoNi)_{80}Cr_{20}$, (g) $(CoNi)_{95}Cr_5$, (h) CoFeMnNi, (i) CoCrFeNi, and (j) $Co_{20}(CrNi)_{80}$ heavily deformed by HPT and then annealed at various temperatures (indicated in graphs) for 1.2 ks followed by water quenching. Diffraction peaks marked by (*h k l*) correspond to the peaks of (*h k l*) refection of FCC structure. Black arrows indicate (1 1 0) peaks of s phase with $D8_b$ structure or simple BCC structure.

22
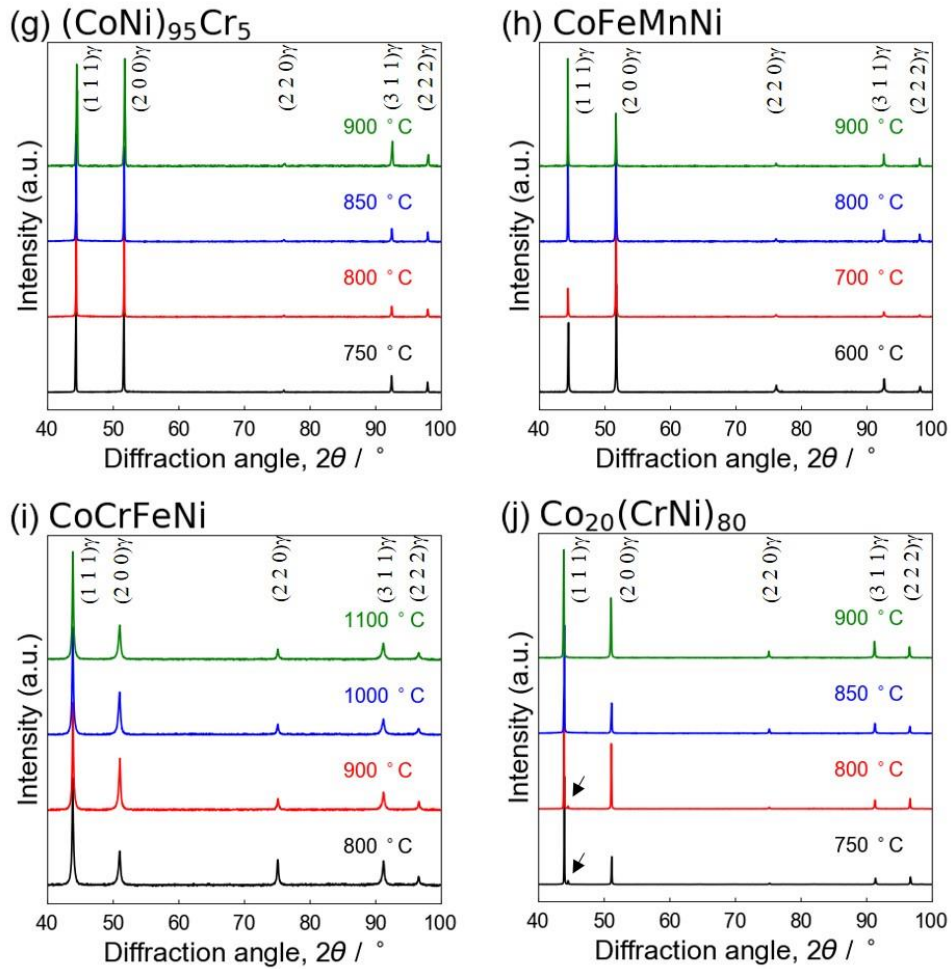
Figure 2.1 (Continued.): XRD profiles of the specimens of (a) Ni-40Co, (b) FeMnNi, (c) CoMnNi, (d) CoFeNi, (e) CoCrNi, (f) $(CoNi)_{80}Cr_{20}$, (g) $(CoNi)_{95}Cr_5$, (h) CoFeMnNi, (i) CoCrFeNi, and (j) $Co_{20}(CrNi)_{80}$ heavily deformed by HPT and then annealed at various temperatures (indicated in graphs) for 1.2 ks followed by water quenching. Diffraction peaks marked by (*h k l*) correspond to the peaks of (*h k l*) refection of FCC structure. Black arrows indicate (1 1 0) peaks of s phase with $D8_b$ structure or simple BCC structure.

Figure 2.2 (a – d) show EBSD phase maps of $Co_{20}(CrNi)_{80}$ annealed at temperatures ranging from 750°C to 900 °C followed by water quenching, where FCC phase and BCC phase were colored by red and yellow, respectively. Note that the unindexed (black) points were regions with low confidence index (CI) value in the EBSD measurement, indicating that the quality of the Kikuchi-line at the point was too low to index in the EBSD analysis. In **figure 2.2**, the black points mostly corresponded to grain boundaries where Kikuchi-patterns of both sides of grains overlap. There are yellow BCC phase regions finely dispersed in the specimens annealed at 750 °C and 800 °C. They appear to be corresponding to the extra peak of an unknown phase in **figure 2.1 (j)**. According to the previous study on the phase stability in Co-Cr-Ni ternary systems by Omori *et al*. [50], it was suggested that the second phase could be a σ phase with $D8_b$ crystal structure or simple BCC phase formed during annealing processes at lower temperatures (below 800
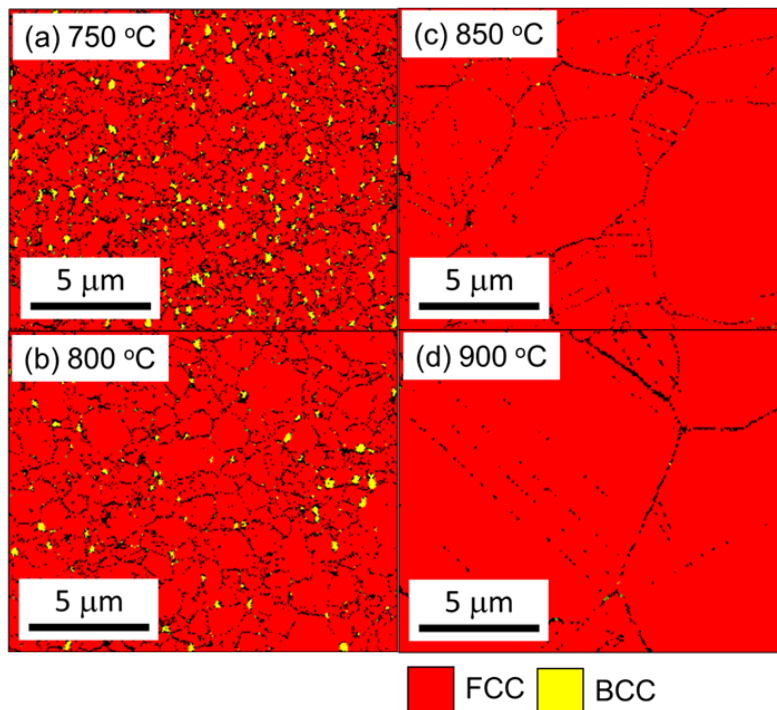
Figure 2.2: EBSD phase maps of the $Co_{20}(CrNi)_{80}$ specimens HPT-processed and annealed at (a) 750°C, (b) 800°C, (c) 850°C or (d) 900 °C for 600 s followed by water quenching. Red and yellow colored regions correspond to those showing FCC and BCC structures, respectively.

$^{\mathrm{o}}$C). Accordingly, the extra park in **figure 2.1 (j)** can be (1 1 0) reflection of σ phase or simple BCC phase. To avoid complexly, in the case of $Co_{20}(CrNi)_{80}$, only the specimens annealed at 850°C and 900 $^{\mathrm{o}}$C to have single-phase structures were used for the subsequent analysis.

Representative microstructures obtained by SEM-BSE observations of the studied alloys heavily deformed by HPT and subsequently annealed are shown in **figure 2.3 (a – t)**. Fully-recrystallized microstructures with various mean grain sizes were obtained. Large numbers of annealing twins were observed in most alloys. In some alloys (e.g., CoFeNi (e, f)), the density of annealing twins was relatively small possibly due to the effect of stacking fault energy (SFE). Mean grain sizes counting twin boundaries (*d*) are indicated in the figures. Ultra-fine grained (UFG) microstructures with mean grain size smaller than 1 μm were attained by changing the annealing temperature and holding time, which suggested high-density nucleation sites for recrystallization were introduced by the HPT process. The details of recrystallization behavior in HEAs and MEAs will be discussed later in Chapter 4.
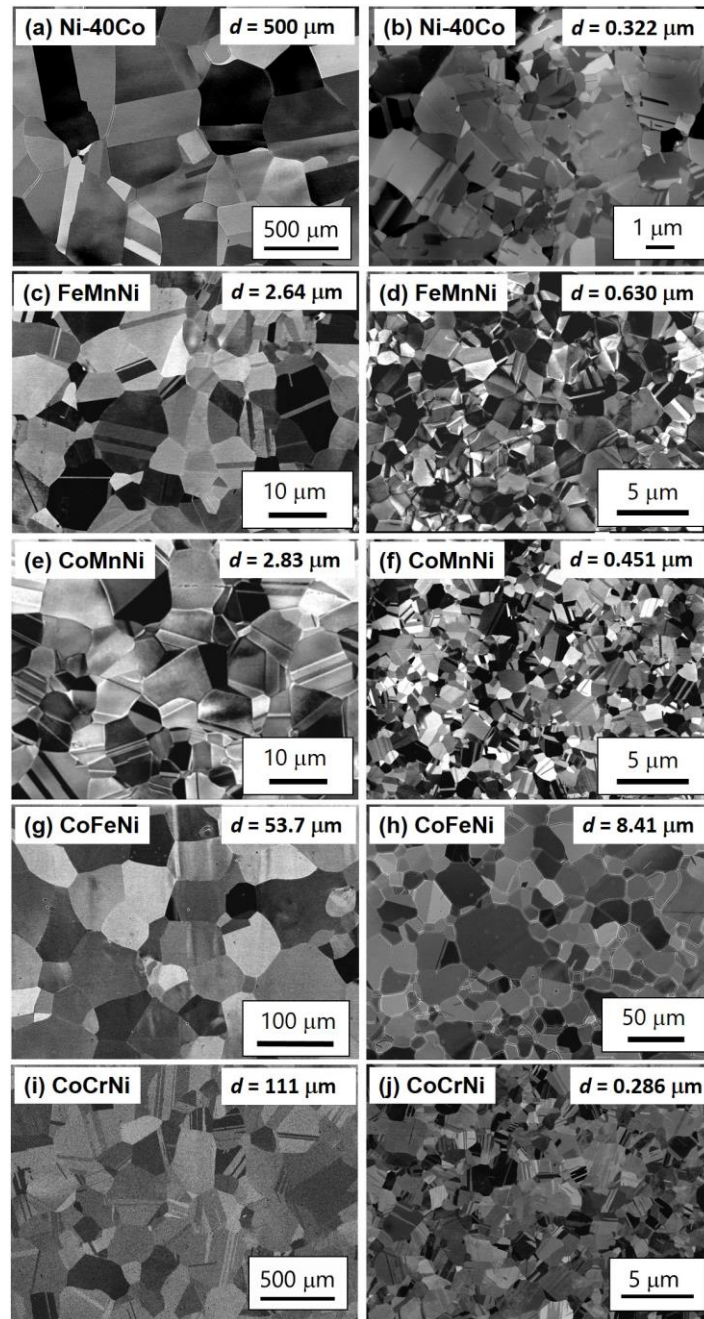
Figure 2.3: Representative SEM-BSE images of the studied alloys heavily deformed by HPT and subsequently annealed under different conditions. Ni-40Co annealed at (a) 600 °C for 30 s and (b) 800 °C for 30 s. FeMnNi annealed at (c) 850 °C for 600 s and (d) 750 °C for 120 s. CoMnNi annealed at (e) 850 °C for 1.2 ks and (f) 750 °C for 30 s. CoFeNi annealed at (g) 900 °C for 600 s and (h) 750 °C for 1.2 ks. CoCrNi annealed at (i) 1200 °C for 12 h and (j) 800 °C for 600 s. $(CoNi)_{80}Cr_{20}$ annealed at (k) 1000 °C for 600 s and (l) 800 °C for 30 s. $(CoNi)_{95}Cr_5$ annealed at (m) 900 °C for 600 s and (n) 750 °C for 30 s. CoFeMnNi annealed at (o) 900 °C for 30 s and (p) 750 °C for 30 s. CoCrFeNi annealed at (q) 1100 °C for 1.2 ks and (r) 800 °C for 30 s. and $Co_{20}(CrNi)_{80}$ annealed at (s) 850 °C for 7.2 ks and (t) 850 °C for 20 s. Mean grain sizes counting twin boundaries (d) are indicated.

Figure 2.3 (Continued.): Representative SEM-BSE images of the studied alloys heavily deformed by HPT and subsequently annealed under different conditions. Ni-40Co annealed at (a) 600 °C for 30 s and (b) 800 °C for 30 s. FeMnNi annealed at (c) 850 °C for 600 s and (d) 750 °C for 120 s. CoMnNi annealed at (e) 850 °C for 1.2 ks and (f) 750 °C for 30 s. CoFeNi annealed at (g) 900 °C for 600 s and (h) 750 °C for 1.2 ks. CoCrNi annealed at (i) 1200 °C for 12 h and (j) 800 °C for 600 s. $(CoNi)_{80}Cr_{20}$ annealed at (k) 1000 °C for 600 s and (l) 800 °C for 30 s. $(CoNi)_{95}Cr_5$ annealed at (m) 900 °C for 600 s and (n) 750 °C for 30 s. CoFeMnNi annealed at (o) 900 °C for 30 s and (p) 750 °C for 30 s. CoCrFeNi annealed at (q) 1100 °C for 1.2 ks and (r) 800 °C for 30 s. and $Co_{20}(CrNi)_{80}$ annealed at (s) 850 °C for 7.2 ks and (t) 850 °C for 20 s. Mean grain sizes counting twin boundaries (*d*) are indicated.

2.3.3. Mechanical properties and Hall-Petch relationship

Figure 2.4 (a - j) show engineering stress-strain curves of the studied alloys with various mean grain sizes, obtained by the tensile tests at room temperature. In all the materials, the yield strength increased with decreasing the mean grain size. This is the well-known Hall-Petch effect [51,52] in which the yield stress (σ_Y) of polycrystalline materials is described as

$$\sigma_Y = \sigma_0 + kd^{-\frac{1}{2}}, \tag{2.2}$$

where σ_0 is the friction stress, k is the constant (the Hall-Petch slope), and d is the mean grain size of the material. It was noteworthy, moreover, that many of the specimens with UFG microstructures exhibited discontinuous yielding, as has been previously reported in other UFG materials with FCC crystal structure [53–56]. Generally, there is a trade-off relationship between strength and tensile ductility in metallic materials, and most of the alloys used also showed the same tendency. However, interestingly, some of the alloys (e.g., (a) FeMnNi and (e) $(CoNi)_{95}Cr_5$) were found not to follow the trade-off relationship of strength and ductility. This might be related to the change in deformation mechanisms leading to different work-hardening behaviors depending on the mean grain size, which can be future work.
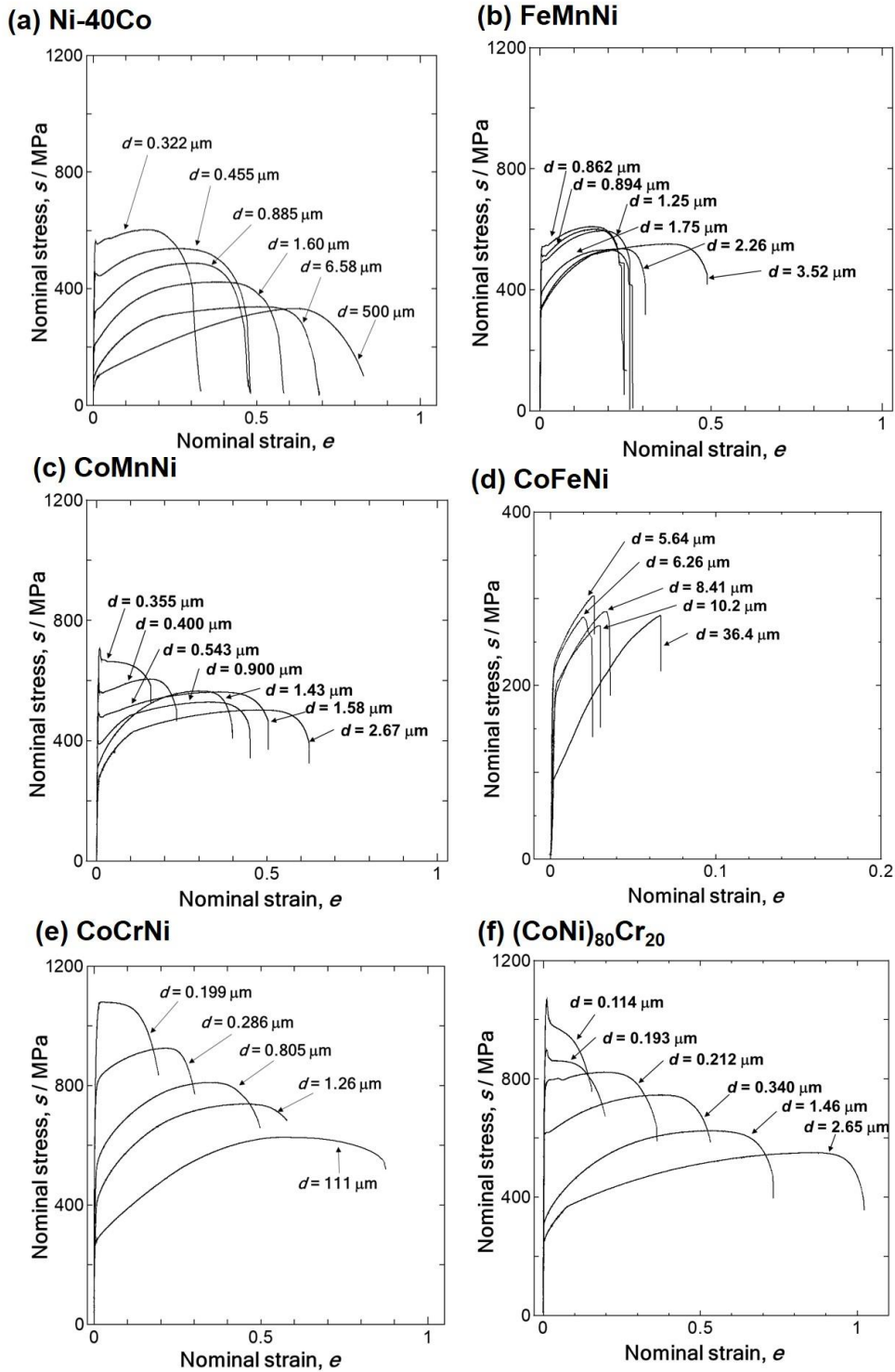
Figure 2.4: Engineering stress-strain curves of the studied alloys with various mean grain sizes, obtained by the tensile tests at room temperature. (a) Ni-40Co, (b) FeMnNi, (c) CoMnNi, (d) CoFeNi, (e) CoCrNi, (f) $(CoNi)_{80}Cr_{20}$, (g) $(CoNi)_{95}Cr_5$, (h) CoFeMnNi, (i) CoCrFeNi, and (j) $Co_{20}(CrNi)_{80}$, respectively, all heavily deformed by HPT and subsequently annealed under different conditions to achieve various grain sizes.
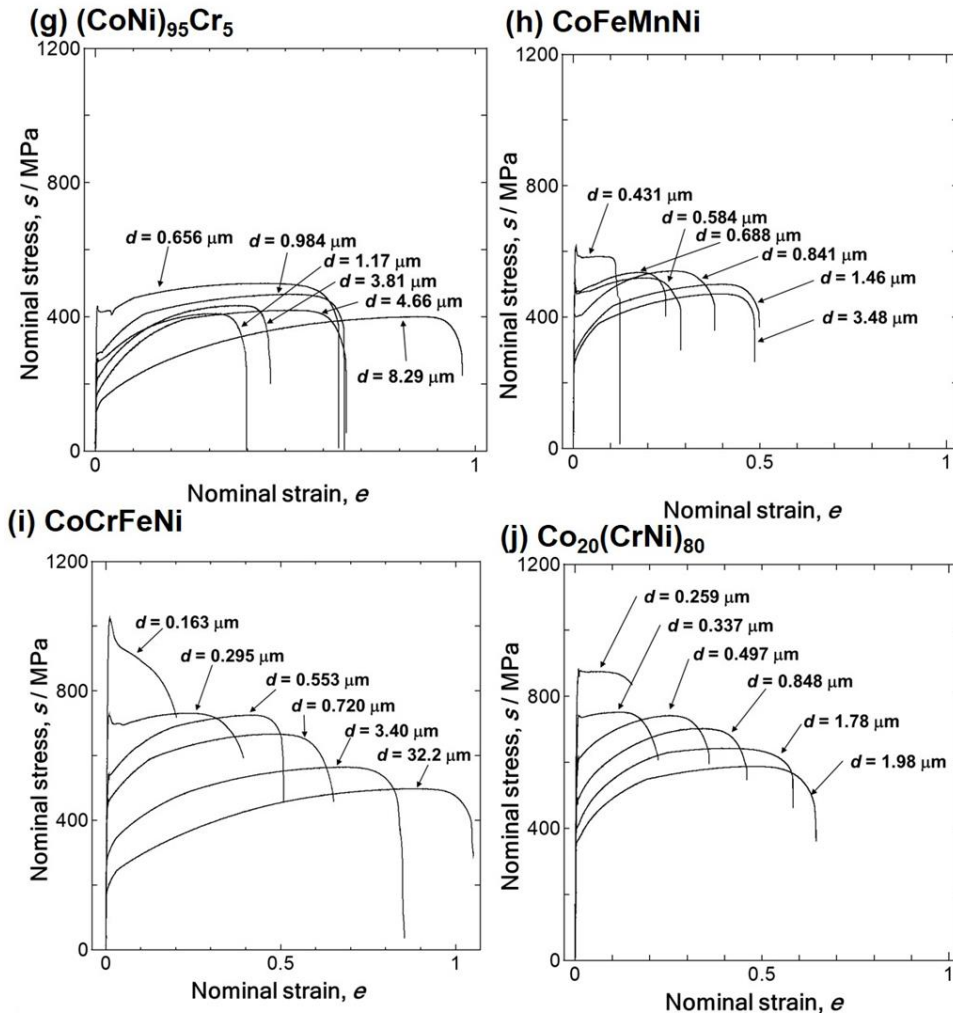
Figure 2.4 (Continued.): Engineering stress-strain curves of the studied alloys with various mean grain sizes, obtained by the tensile tests at room temperature. (a) Ni-40Co, (b) FeMnNi, (c) CoMnNi, (d) CoFeNi, (e) CoCrNi, (f) $(CoNi)_{80}Cr_{20}$, (g) $(CoNi)_{95}Cr_5$, (h) CoFeMnNi, (i) CoCrFeNi, and (j) $Co_{20}(CrNi)_{80}$, respectively, all heavily deformed by HPT and subsequently annealed under different conditions to achieve various grain sizes.

Hall-Petch relationships obtained from the tensile tests of the alloys studied in the present study are shown in **figure 2.5 (a - j)**. Fairly precise and reliable Hall-Petch curves could be obtained after collecting a number of data plots from the present experiments using specimens with wide ranges of the mean grain sizes. The extra-hardening phenomenon, in which the Hall-Petch slope became larger in fine grain-size regions than that in coarse grain-size regions, was observed. The extra hardening phenomenon has been reported in other UFG materials [57,58], whereas the reason is still unclear. The friction stress, σ_0 of each alloy was obtained by fitting the data plots with **eq. (2.2)**, and the fitting lines are presented as solid lines in **figure 2.5**. Young's modulus, E, Shear modulus, G, obtained σ_0, k and the grain size ranges of the alloys used for fitting are summarized in **table 2.2** together with the values for pure Ni and CoCrFeMnNi HEA previously reported [11,59,60].
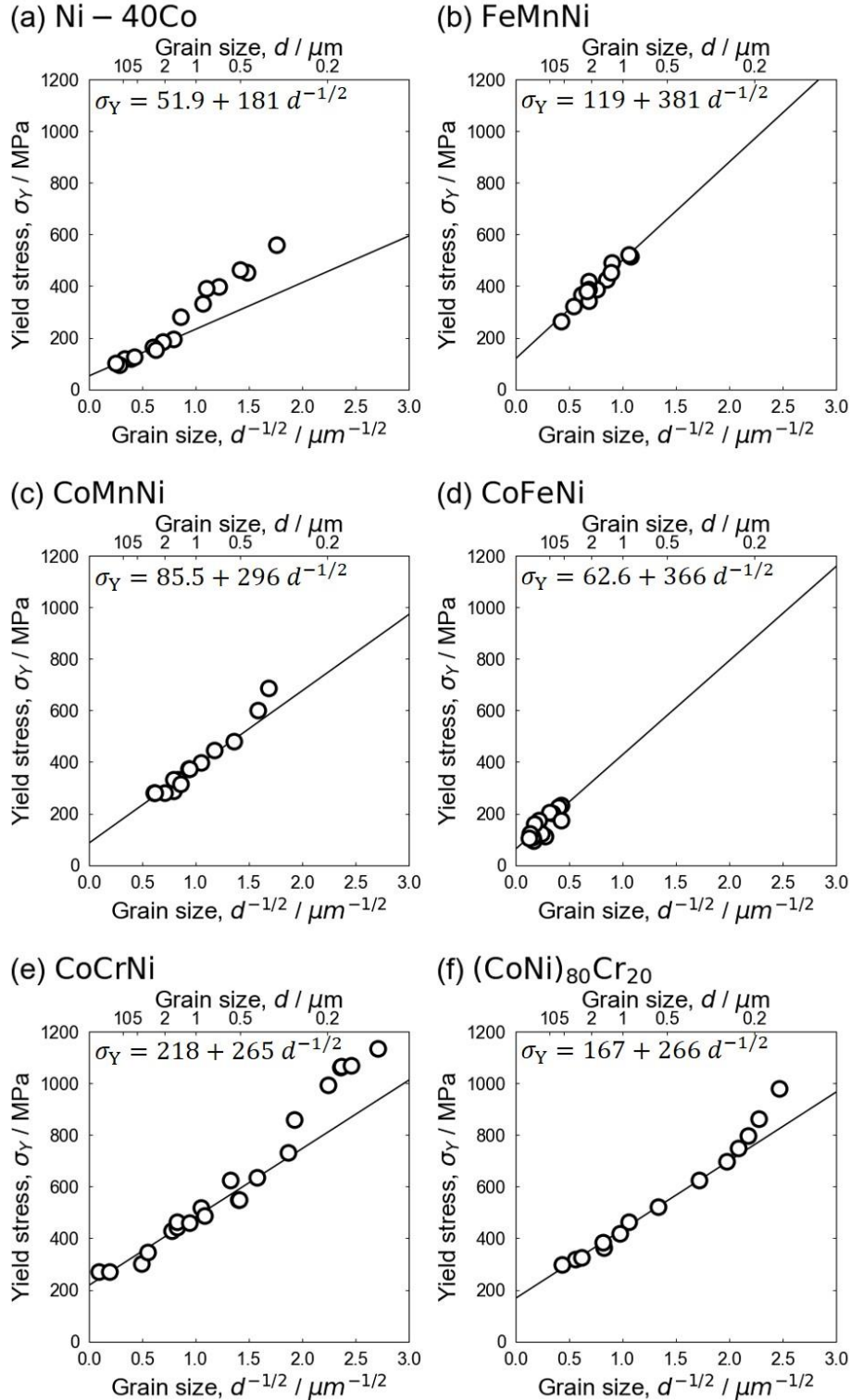
Figure 2.5: Hall-Petch relationships of the alloys studied: (a) Ni-40Co, (b) FeMnNi, (c) CoMnNi, (d) CoFeNi, (e) CoCrNi, (f) $(CoNi)_{80}Cr_{20}$, (g) $(CoNi)_{95}Cr_5$, (h) CoFeMnNi, (i) CoCrFeNi, and (j) $Co_{20}(CrNi)_{80}$. The solid black lines are fitting lines based on **eq. (2.5)** in the grain size ranges shown in **table 2.2**. Concrete Hall-Petch equations obtained are shown in the figures.

32
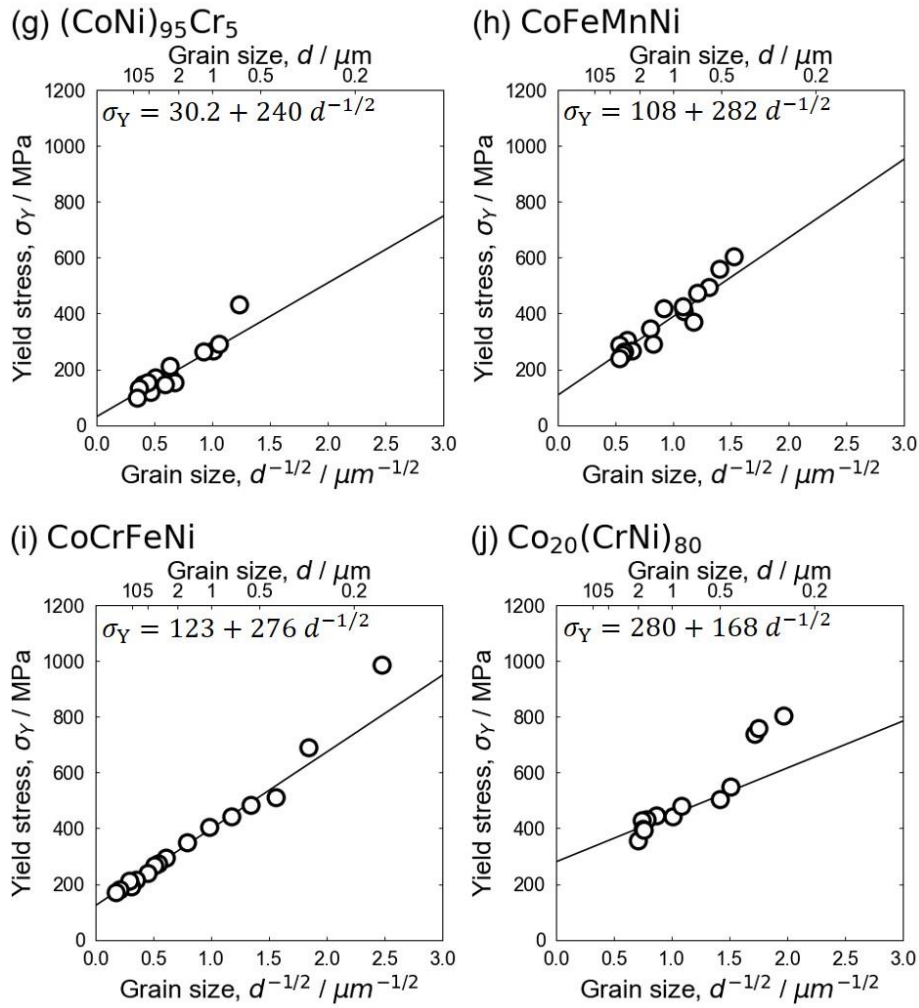
Figure 2.5 (Continued.): Hall-Petch relationships of the alloys studied: (a) Ni-40Co, (b) FeMnNi, (c) CoMnNi, (d) CoFeNi, (e) CoCrNi, (f) $(CoNi)_{80}Cr_{20}$, (g) $(CoNi)_{95}Cr_5$, (h) CoFeMnNi, (i) CoCrFeNi, and (j) $Co_{20}(CrNi)_{80}$. The solid black lines are fitting lines based on **eq. (2.5)** in the grain size ranges shown in **table 2.2**. Concrete Hall-Petch equations obtained are shown in the figures.

Table 2.2: Young's modulus determined from the stress-strain curves, Shear modulus extracted from Ref. [48], friction stress at room temperature, Hall-Petch slope determined by the Hall-Petch relationship, grain size range used for fitting of **eq. (2.2)**, and extrapolated strength at 0 K ($\tau(0\ K)$) based on Ref. [60] for the studied MEAs, CoCrFeMnNi HEA and pure Ni.

Alloy	E [GPa]	G [GPa]	σ_0 [MPa]	k [μm$^{-1/2}$]	d [μm]	$\tau(0\ K)$ [MPa]	Ref.
Pure Ni	199	76	21.8	180	30.0 - 385	13.5	[48,59,60]
Ni-40Co	213	86	51.9	181	1.60 – 500	43.5	[42,48]
FeMnNi	182	73	119	381	0.848 – 5.52	103	[48]
CoMnNi	190	77	85.5	296	0.719 – 2.68	103	[48]
CoFeNi	161	60	62.6	366	5.64 – 68.3	83.5	[48]
CoCrNi	226	87	218	265	0.286 - 111	183	[42,48]
$(CoNi)_{80}Cr_{20}$	223	86	167	266	0.256 – 5.35	113	[48]
$(CoNi)_{95}Cr_5$	219	85	30.2	240	0.895 – 8.29	60.1	[48]
CoFeMnNi	186	77	108	282	0.431 – 3.48	101	[48]
CoCrFeNi	210	82	123	276	0.553 – 32.2	152	[48]
$Co_{20}(CrNi)_{80}$	240	87	280	168	0.497 – 1.98	203	[48]
CoCrFeMnNi	202	80	125	494	4.40 - 155	149	[11,48,60]
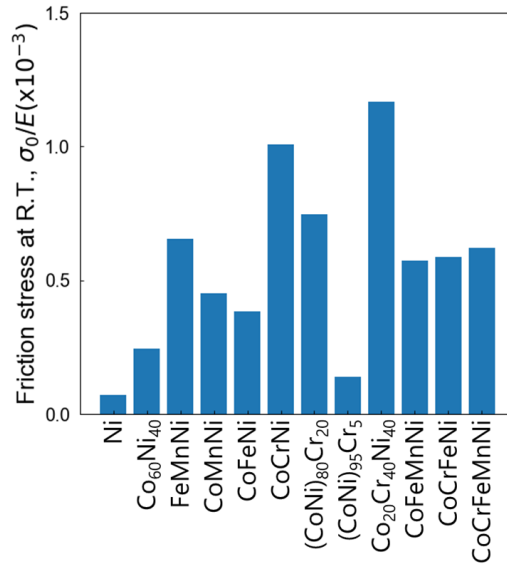
Figure 2.6: Friction stresses (σ_0) of various alloys at room temperature (R. T.). The values of friction stress were extracted from the Hall-Petch relationship shown in **figure 2.5** and **table 2.2**, and then normalized by Young's modulus (E) to eliminate the effect of elastic modulus.

All experimentally obtained values of the friction stress at room temperature for the present alloys are compared in **figure 2.6**, where the σ_0 values were divided by Young's modulus, E, to remove the effect of elastic modulus. It was confirmed that $Co_{20}(CrNi)_{80}$ showed the highest friction stress ($\sigma_0 = 280$ MPa, $\sigma_0 / E = 1.17 \times 10^{-3}$) among the alloys. It should be noted that the increase in the number of alloying elements does not simply result in an increase in strength (σ_0).

2.4. Discussion

In high-alloy systems, different alloying elements occupy different lattice sites, and the crystal lattice is significantly (and heterogeneously) distorted everywhere owing to the difference in the atomic radius of constituent elements. Consequently, the local position of each atom may be largely shifted from the average lattice position determined

from the average lattice constant of crystal structure, depending on the local arrangement of elements, so that different lattice distortions arise locally. Thus, HEAs and MEAs is essentially considered heterogeneous on an atomic-scale. As described in the previous section, the friction stresses of FCC HEAs and MEAs are significantly higher than those of conventional dilute alloys and pure metals. The origin of the high friction stress is considered in the following part, correlating to the atomic-scale heterogeneity in HEAs and MEAs.

2.4.1. Interaction between dislocations and alloying elements

The dislocations in FCC crystals can be dissociated into two Shockley partial dislocations forming intrinsic stacking faults in between. In pure metals, the width of the stacking fault maintains a constant value as far as the character of dislocations is unchanged and there is no interaction with other dislocations. In contrast, due to the atomic-scale heterogeneity, the width of stacking faults in HEAs and MEAs may vary at each location, as shown in **figure 2.7**. Such fluctuation of stacking fault width in CoCrFeMnNi HEA has been experimentally observed by Smith *et al.* [61]. This indicates that the SFE in HEAs and MEAs can be locally changed depending on the local chemical environment around each segment [61], and shapes of partial dislocations are spontaneously adjusted to minimize the total free energy of the system [62,63]. Therefore, the friction stress can be interpreted as required stress for dislocations to break such an energetically favorable shape (i.e., energetically favorable state) and start moving with the assistance of stress and/or thermal activation.
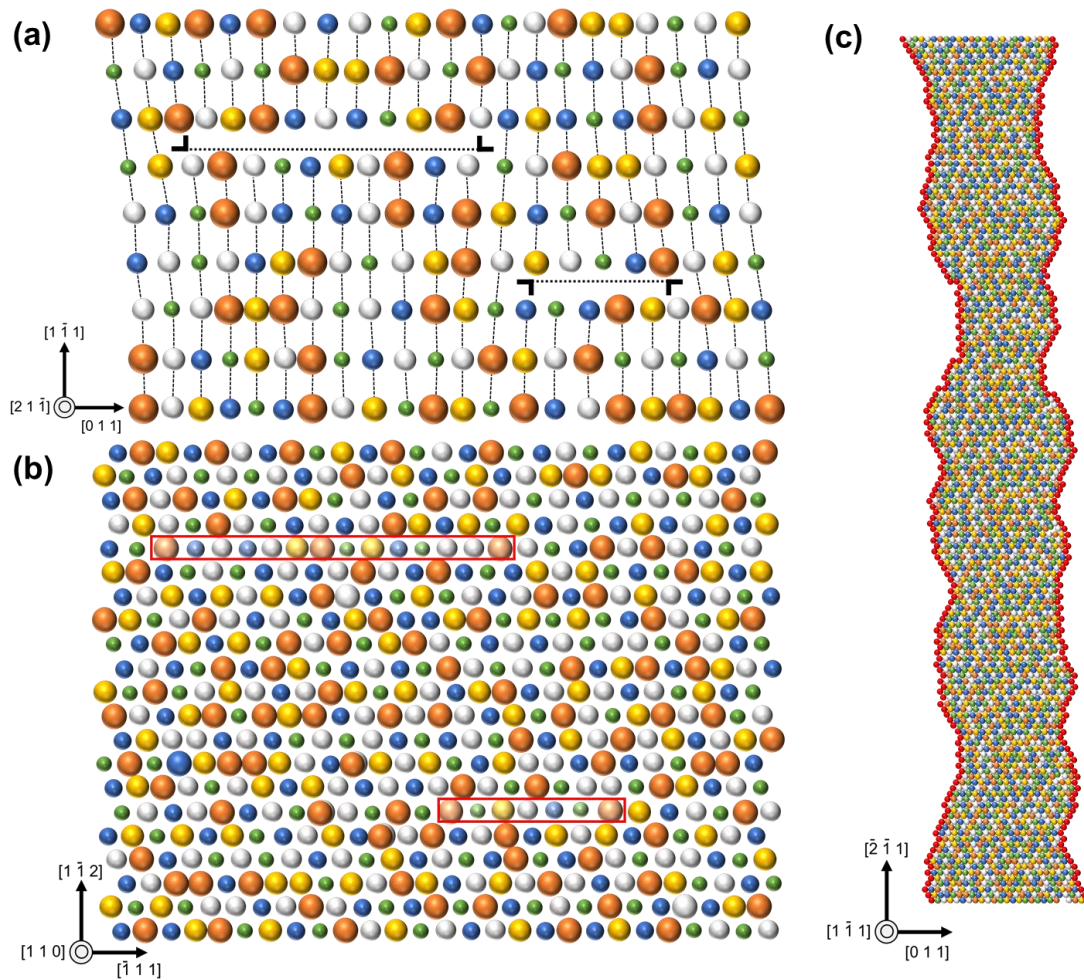
Figure 2.7: Schematic illustrations showing dislocation core structures at two different locations in crystal lattices of FCC HEAs and MEAs, viewed from (a) [2 1 -1], (b) [1 1 0], and (c) [1 -1 1] directions. Each atom having different color corresponds to different kinds of elements. Regions where stacking faults exist between Shockley partial pairs are indicated by dashed lines in (a), red rectangles in (b), and red outlines in (c). Depending on the local chemical environment, the width of a stacking fault can be different as shown in (c).

The above description is indeed equivalent to what Labusch considered when he formulated the theory of solution strengthening in solid solution alloys having relatively higher solute concentrations [45,60,64,65]. When solute atoms are embedded in a solvent matrix, there is misfit around the solutes that mainly originated from the difference in their atomic sizes and elastic modulus. In the theory, it was assumed that the elastic field of dislocations always interacts with multiple weak obstacles (i.e., misfit of solute

elements), and dislocations change their core structures and line shapes to achieve a local minimum of free energy in the system (**Figure 2.8 (a)**). According to the assumptions above, the solid solution strengthening effect in dilute alloys with FCC structure is formulated as

$$\frac{\tau(0\ \mathrm{K})}{G} \propto \left({\eta'_{\mathrm{loc}}}^2 + \alpha^2 \varepsilon_{\mathrm{loc}}^2\right)^{\frac{2}{3}} \rho^{\frac{2}{3}}, \tag{2.3}$$

where $\tau(0\ \mathrm{K})$ is the critical resolved shear stress (CRSS) for dislocation slip at 0 K, G is the shear modulus, η'_{loc} is the local modulus misfit, $\varepsilon_{\mathrm{loc}}$ is the local atomic size misfit (local lattice distortion), α is a constant depending on the type of dislocation considered (Labusch assumed $\alpha = 16$), and ρ is the number density of the obstacles on a slip plane. It is reasonable, in binary systems, to assume $\rho \sim c$, the concentration of solutes. The validity of the Labusch model has been supported by a number of experimental data in conventional binary FCC alloys [46], and some researchers extended the idea to dilute
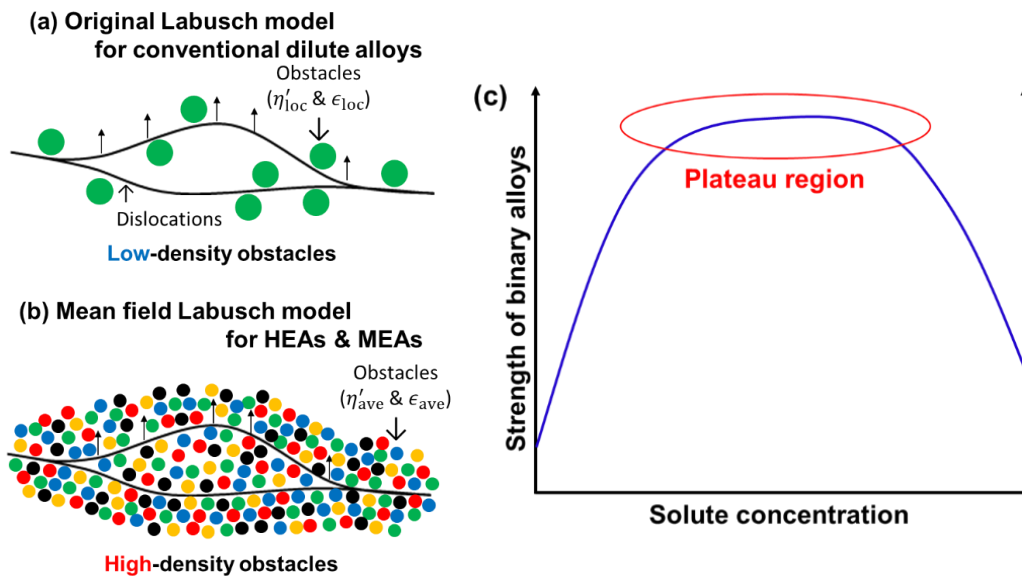
Figure 2.8: Schematic illustrations showing distributions of obstacles around a dislocation on a slip plane in (a) conventional dilute systems and (b) high-alloy systems such as MEAs and HEAs, respectively. (c) Relationship between the strength of an isomorphous system and solute concentration.

multicomponent systems [47]. Some attempts have been also made to apply the Labusch theory to HEAs and MEAs [48]. However, it was found that the values derived from the theory were both qualitatively and quantitatively inconsistent with the experimental results. This suggests that the Labusch model cannot be simply applicable to HEAs and MEAs, in which it is impossible to define solutes and solvents.

Recently some research groups developed new theoretical models applicable to HEAs and MEAs, based on the Labusch model. In the proceeding parts, the experimentally-obtained friction stress values are compared with two of the new theoretical models applicable to HEAs and MEAs.

2.4.2 Mean-field Labusch model (Toda-Caraballo model)

Now, it is considered that a mean-field of obstacles where dislocations are surrounded by high-density weak obstacles having mean values of atomic size misfit and modulus misfit (**Figure 2.8 (b)**). So that it is possible to replace η'_{loc} and ε_{loc} by the average modulus misfit parameter, η'_{ave}, and the average atomic size misfit parameter (the average lattice distortion), ε_{ave}, respectively. Now it is assumed that the number density of mean obstacles becomes a constant value, $\rho \sim$ const., near the equi-atomic composition, independent of the kind of alloying elements. This assumption may be reasonable by considering an analogous of isomorphous binary systems showing a peak or plateau of the strength around 50 at.% concentration, where the strength is almost independent of the solute concentration, as shown in **figure 2.8 (c)**. Thus, **eq. (2.3)** can be modified as

$$\frac{\tau(0 \text{ K})}{G} \propto \left(\eta'^2_{\text{ave}} + \alpha^2 \varepsilon^2_{\text{ave}}\right)^{\frac{2}{3}}, \tag{2.4}$$

Also, since η'_{ave} is small enough compared to $\alpha\varepsilon_{\text{ave}}$ in many FCC metals (the contribution of atomic size misfit to the strength is 250 – 1000 times larger than that of modulus misfit, according to the simple calculation by Fleischer [43,44]), **eq. (2.4)** can be simplified as

$$\frac{\tau(0 \text{ K})}{G} \propto \varepsilon^{\frac{4}{3}}_{\text{ave}}. \tag{2.5}$$

Wu *et al*. [60] already reported the shear modulus, *G*, and temperature dependence of the yield strength in various kinds of HEAs and MEAs. In this study, the friction stress, σ_0, at room temperature (the strength of materials excluding the effect of the grain size) was determined from the intercepts of the Hall-Petch relationships at room temperature experimentally acquired, and the experimentally obtained values of σ_0 were extrapolated to 0 K by using the results reported by Wu *et al*. [60], assuming that the Hall-Petch slope was independent of temperature in low-temperature region. It should be noted that the temperature dependence of Hall-Petch slopes, *k*, was mainly originated from the temperature dependence of elastic modulus [66]. In a conventional dislocation pile-up model proposed by Hall and Petch [51,52], Hall-Petch slope is considered as proportional to the square-root of shear modulus ($k \propto \sqrt{G}$). According to the experimental estimation previously done [67], the shear modulus of CoCrFeMnNi HEA increased by about 10 % with decreasing temperature from room temperature to 0 K. Assuming that the conventional dislocation pile-up model can be applied for the HEA, the effect of temperature can be estimated as about 5 %. Since this difference is very small, the effect of temperature on Hall-Petch slopes is considered to be negligible. Wu *et al*. [60] reported

that the temperature dependence of the yield strength of the alloys (σ_Y) with finite grain sizes could be expressed as

$$\sigma_Y(T) = \sigma_{ath} + \sigma_{th} \exp(-T/C), \qquad (2.6)$$

where σ_{ath} and σ_{th} are athermal part (including the effect of grain size) and thermal part of the strength, respectively, and C is a fitting parameter. To determine the temperature dependence of the friction stress ($\sigma_0(T)$), σ_{th} and C were set as the same as they reported. Because they did not provide the values of grain sizes including twin boundaries, σ_{ath} was adjusted so that the yield strength at 300 K calculated by the equation coincided with the value of the friction stress obtained at room temperature. For example, they reported that σ_{th} and C of CoCrNi MEA were 489 MPa and 228 K. Therefore, the temperature dependence of the friction stress could be expressed as $\sigma_0(T) = \sigma_{ath} + 489 \exp(-T/228)$ [MPa], and $\sigma_0(T = 300\ K) = 131 + \sigma_{ath}$ [MPa] was obtained. Since the actual friction stress at room temperature was 218 [MPa], it was possible to determine that $\sigma_{ath} = 87$ [MPa]. Thus, the friction stress at 0 K was estimated as $\sigma_0(T = 0\ K) = 576$ [MPa]. Note that, due to the lack of data in the article by Wu *et al.*, G, σ_{th}, and C, parameters of $(CoNi)_{(100-x)}Cr_x$ (x = 5, 20 at. %) were estimated by a simple rule of mixture between the values of CoNi and CoCrNi, and G, σ_{th} and C of Ni-40Co and $Co_{20}(CrNi)_{80}$ were assumed to be the same as those for CoNi and CoCrNi, respectively. Afterward, $\tau(0\ K)$ was determined by dividing σ_0 at 0 K by the Taylor factor for FCC materials having random texture (= 3.06) because the recrystallization texture of FCC metals was usually very weak [68].

Toda-Caraballo *et al.* [69,70] proposed an effective model for estimating the average lattice constant, a, and the average atomic size misfit parameter, ε_{ave}, of HEAs and MEAs.
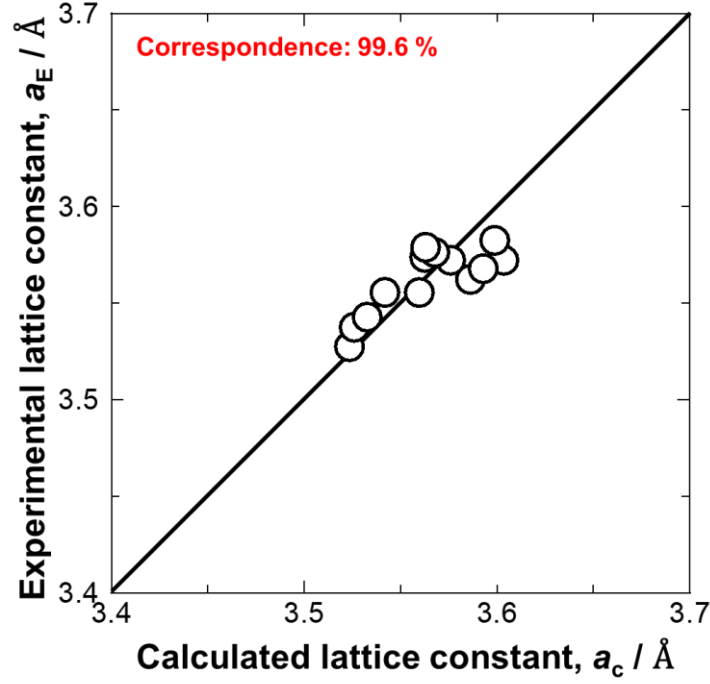
Figure 2.9: Comparison between the average lattice constant calculated by the Toda-Caraballo model (**Eq. (2.7) and (2.8)**), a_c, and the lattice constants experimentally obtained by XRD profiles shown in **figure 2.1**, a_E, of the alloys studied. The lattice constants obtained by XRD agreed well with those predicted by the Toda-Caraballo model with an accuracy of more than 99 %.

In their model, the interatomic distance between element i and first-neighboring element j is expressed as

$$s_{ij} = \frac{s_{ii}^2 K_i x_i + s_{jj}^2 K_j x_j}{s_{ii} K_i x_i + s_{jj} K_j x_j},$$ (2.7)

where s_{ii} is the atomic size of pure elements, K_i is the bulk modulus of pure elements and x_i is the concentration of the elements. The average lattice constant of the alloy, a, is calculated as

$$a = f \sum_{ij} s_{ij} x_i x_j,$$ (2.8)

where f is a constant depending on the crystal structure assuming a rigid sphere model (e.g., $f = \sqrt{2}$ for FCC). **Figure 2.9** shows a comparison between the average lattice constant calculated by the Toda-Caraballo model (**Eq. (2.7) and (2.8)**), a_c, and lattice

42

constants experimentally obtained by XRD (**Figure 2.1**), a_E of the alloys studied. The

lattice constant obtained by XRD agreed with that predicted by the Toda-Caraballo model

with an accuracy of more than 99 %. This fact validated the applicability of the Toda-

Caraballo model to the alloys used in the present study. If a small amount (Δx_i^j) of

element i in the average matrix of the alloys is replaced by element j, the average lattice

constant, a, will be slightly changed to ($a + \Delta a_i^j$), and this small variation of the average

lattice constant, da / dx_i^j, can be analytically calculated as

$$\frac{da}{dx_i^j} = \frac{(a + \Delta a_i^j) - a}{\Delta x_i^j}. \tag{2.9}$$

Note that the average lattice constant obtained by **eq. (2.7) and (2.8)** is continuous and

differentiable against the concentration, which means that the materials used are single-

phase solid solutions in the arbitrary concentration regions where any discontinuous

change in the lattice constant (by phase transformation, for example) does not happen.

Moreover, the average atomic size misfit of the alloy, ε_{ave}, can be obtained as

$$\varepsilon_{\text{ave}} = \sum_{ij} \left| \frac{1}{a} \frac{da}{dx_i^j} \right| x_i x_j \tag{2.10}$$

In the present study, the ε_{ave} for the MEAs and HEAs were calculated by using **eq. (2.9)**

and (2.10) based on the parameters presented in **table 2.3**.

Table 2.3: Interatomic distance, s_{ii}, and bulk modulus, K_i, of each element used for the Toda-Caraballo model [71], and atomic volume of each element used for the Leyson-Varvenne model [63,72].

Elements	s_{ii} [Å]	K_i [GPa]	V [Å^3]
Cr	2.60	160	12.3
Mn	2.58	120	12.24
Fe	2.56	170	12.09
Co	2.54	180	10.82
Ni	2.52	180	10.81

Figure 2.10 (a) shows a relationship between the average atomic size misfit (lattice distortion) calculated by the Toda-Caraballo model and the strength of the alloys at 0 K normalized by the shear modulus (G). The experimentally obtained values of σ_0 were extrapolated to 0 K by using the data of various FCC HEAs and MEAs reported by Wu *et al.* [60]. Afterward, $\tau(0\ K)$ was determined by dividing σ_0 at 0 K by the Taylor factor
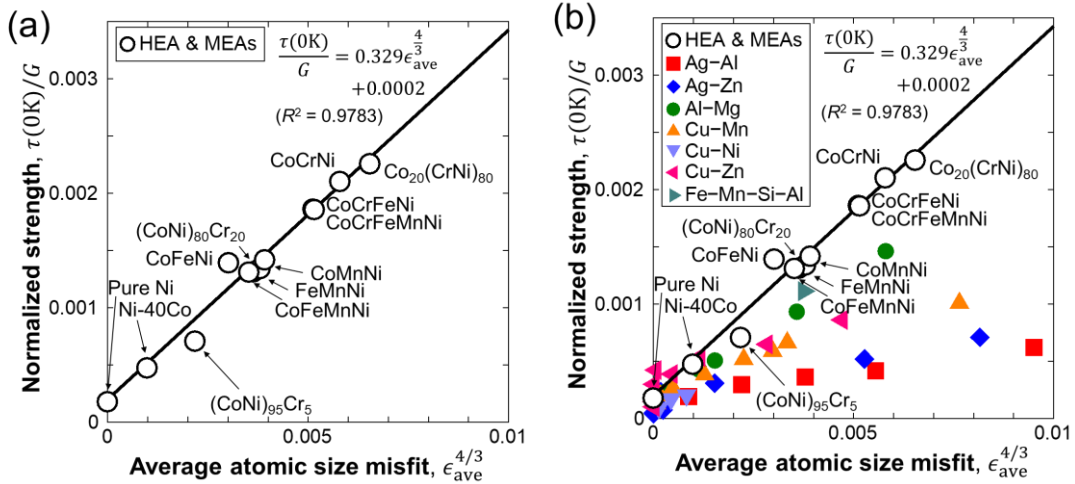
Figure 2.10: (a) Relationship between the average atomic size misfit parameter (the average lattice distortion) calculated by the Toda-Caraballo model and the strength (the friction stress at 0 K estimated by **eq. (2.6)** and divided by the Taylor factor of random texture) normalized by shear modulus (G) of the alloys studied in the present study. The data of pure Ni [48,59,60] and CoCrFeMnNi HEA [11,48,60] are also plotted in the figure. The solid black line is a fitting line determined based on the mean-field Labusch model (**Eq. (2.5)**). (b) The same plot as (a), including the data of various dilute alloys (Ag-Al, Ag-Zn, Al-Mg, Cu-Mn, Cu-Ni, Cu-Zn) [73,74] and Fe-Mn-Si-Al TWIP steel [75]) obtained from previous literature.

for FCC materials having random texture (= 3.06). The solid black line is a fitting line based on the mean-field Labusch model (**Eq. (2.5)**) assuming that elements are randomly distributed in the alloys. It is clear that **eq. (2.5)** fits well with the normalized strength with a correlation of more than 97 %. The consequence indicates that crystal lattices of equi-atomic multicomponent alloys are entirely distorted due to the difference of atomic sizes of the constituent alloying elements, and dislocations in such crystal lattices are considered to be always affected by the elastic fields originated from the lattice distortion state, i.e., dislocations are surrounded by the high-density weak obstacles with average atomic size misfit and modulus misfit (as illustrated in **figure 2.8 (b)**).

In **figure 2.10 (b)**, the data of some dilute alloys (Ag alloys and Cu alloys), which were obtained from previous literature [73–75], are plotted together with the present experimental data shown in **figure 2.10 (a)**. The shear modulus values of the dilute alloys were roughly estimated by the simple rule of mixture for the values of constituent pure elements, and the effect of the grain size was not excluded because of the lack of data. In addition, the average atomic size misfit parameters of the dilute alloys that reflect "*average*" lattice distortion were determined by **eq. (2.10)**, which was different from the definition of the local atomic size misfit parameters reflecting "*local*" lattice distortion ($\varepsilon_{\mathrm{loc}} = \dfrac{1}{a}\dfrac{da}{dc}$), which has been usually used for the conventional Labusch model (**Eq. (2.3)**). Thus, it is possible to simply compare the strength of different materials as a function of the average atomic size misfit (average lattice distortion). It is very interesting that values of the average atomic size misfits for the dilute alloys distribute in a wide range up to 0.01, which is comparable to the distribution of the misfit values for the MEAs and HEA, although it has been believed that the reason for the high strength of HEAs is

due to the "*severe*" lattice distortion effect. In fact, the atomic size differences in some dilute alloys (8 % in Ag-Zn and 12 % in Al-Mg pairs, for instance) are much larger than that in CoCrFeMnNi HEA (3 % in the maximum for a Cr-Ni pair). This means that the local lattice distortion in dilute alloys can be much larger than that in HEAs and MEAs. However, the density of obstacles is very small in dilute alloys, so that similar average atomic size misfit parameters are obtained after averaging the local lattice distortions in an overall slip plane based on **eq. (2.10)**. It should be noted, on the other hand, that the strength of the MEAs and HEA is found to be much higher than that of the dilute alloys even at an equivalent average lattice distortion (average atomic size misfit) in **figure 2.10 (b)**. In other words, the slope of **eq. (2.10)** in the HEAs and MEAs is larger than that in dilute alloys. However, since the mean-field Labusch model does not provide the meaning of the slope which can be influenced by various materials properties, the reason for the difference in the slopes is unclear at this moment. Another model in the next section can give reasons (See also Appendix A).

2.4.3 Leyson-Varvenne model

Leyson *et al.* [76,77] developed an analytical theory of solution strengthening in random FCC alloys based on the Labusch model. In the theory, the interaction energy ($U^n(\boldsymbol{r})$) between dislocations and an atom of alloying elements n (embedded in a matrix) located at $\boldsymbol{r}$ was characterized as a first step. Generally, $U^n(\boldsymbol{r})$ is the summation of the contribution of (1) chemical ($U^n_{\text{Chem}}(\boldsymbol{r})$) and (2) elastic interaction energy ($U^n_{\text{Elast}}(\boldsymbol{r})$). (1) $U^n_{\text{Chem}}(\boldsymbol{r})$ can be calculated by density functional theory (DFT), considering the core structure of dislocations. Outside of the immediate core region, (2) $U^n_{\text{Elast}}(\boldsymbol{r})$ dominates and is approximated as

46

$$U_{\text{Elast}}^n(\boldsymbol{r}) = -p(\boldsymbol{r})\Delta V_n, \tag{2.11}$$

where $p(\boldsymbol{r})$ is the pressure field of dislocations analytically calculated by continuum elasticity theory, and ΔV_n is a parameter called misfit volume having a dimension of [m][3]. A recent study by Yin *et al.* showed that the misfit volume can be determined by both calculation [78,79] and experiments [72]. The misfit volume of the type-n solute ($n = 1$, 2, …, N) in an N-component alloy can be expressed in terms of derivatives of the atomic volume of the alloy ($V_{\text{alloy}} = a^3/4$) with respect to composition. The atomic volume of the alloy can be expressed by the composition of any N - 1 components because of the restriction of $\sum_n c_n = 1$. Thus, the misfit volume of any type-n components can be calculated as

$$\Delta V_n = \frac{\partial V_{\text{alloy}}}{\partial c_n} - \sum_m^N c_m \frac{\partial V_{\text{alloy}}}{\partial c_m}, \tag{2.12}$$

If the lattice constants and chemical compositions of multiple alloys having slightly different chemical composition are given, ΔV_n is directly determined.

Now, as illustrated in **figure 2.11 (a)** [63], it is considered that one straight dislocation, of which the line direction is parallel to the Z-axis, dissociated into two partial dislocations on one of {1 1 1} planes (perpendicular to the Y-axis) in an N-component FCC crystal. The dislocation interacts with the alloying element A located at (x_i, y_j, z_k) embedded in the matrix. The change in interaction energy in a segment of an dislocation having a length ζ moving w away from the original position (In other words, for instance, there is a relative location change of the alloying element A from (x_i, y_j, z_k) to $(x_i - w, y_j, z_k)$ in **figure 2.11 (a)** (**Figure 2.11 (b)** [63]) is expressed as

47
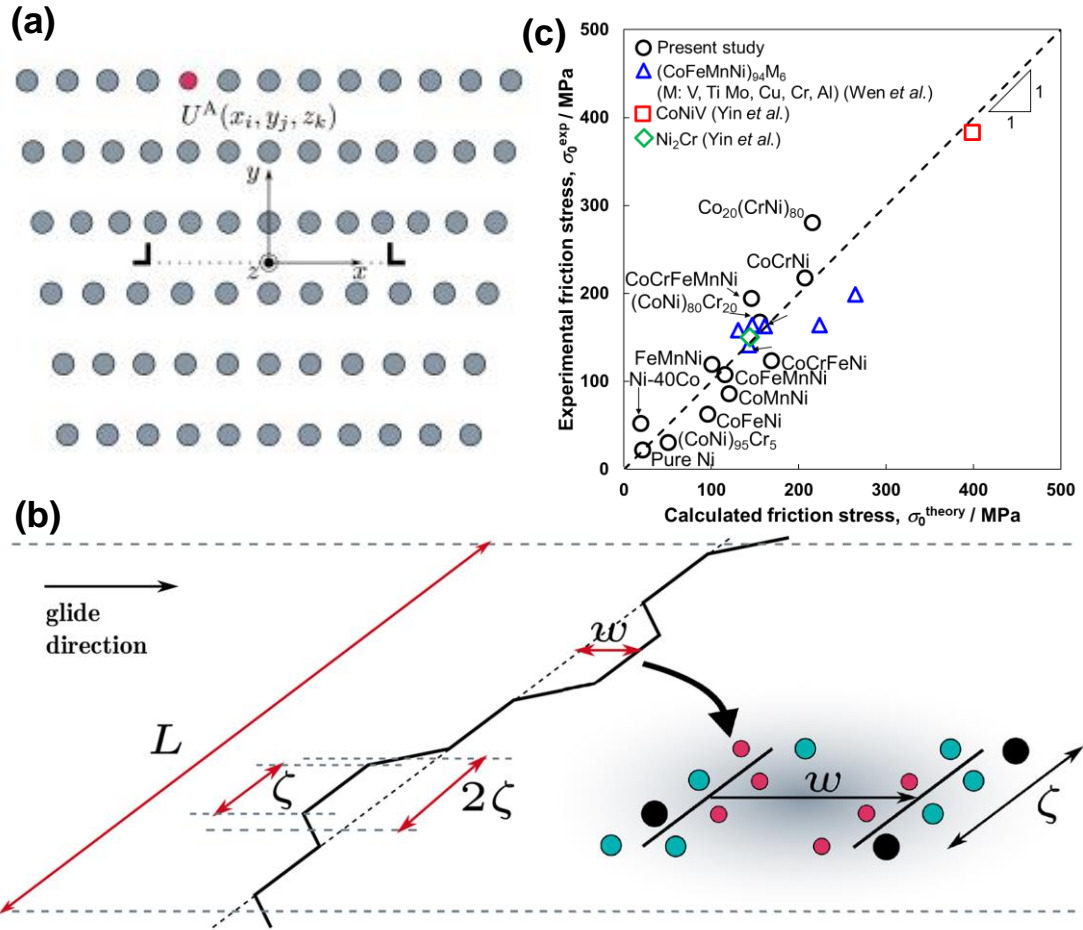
Figure 2.11: (a) A dissociated dislocation lying on one of the {1 1 1} planes in an FCC crystal (perpendicular to the Y-axis) and having a dislocation line along the Z-axis. The alloying element A located at (x_i, y_j, z_k) possesses the interaction energy of U^A. (b) A dislocation with a length of L interacting with alloying elements. The dislocation changes its shape by displacing segments having a length of ζ with a distance of w according to the balance between local potential energy distribution and line tension energy. (c) Comparison between the friction stress values at room temperature with a strain rate of 8.3×10^{-4} s^{-1} determined by the experiments in this study and calculation based on the Leyson-Varvenne model. The data of (CoFeMnNi)$_{94}$M$_6$ (M: V, Ti, Mo, Cu, Cr, Al) [89], CoNiV [90], and Ni$_2$Cr [72] are also plotted together for comparison.

$$\Delta U_{Tot}(\varsigma, w) = \sum_{i,j,k}^{n} s_{ijk}^n \left[U^n(x_i - w, y_j, z_k) - U^n(x_i, y_j, z_k) \right], \qquad (2.13)$$

where $s_{ijk}^n = 1$ if a type-n element is at (x_i, y_j, z_k) and 0 otherwise. The distribution of

alloying elements is now assumed to be random (following the normal distribution). In

this case, the standard deviation (average fluctuation of potential energy) is calculated as

$$\sigma_{\Delta U_{Tot}}(\varsigma, w) = [\langle \Delta U_{Tot}^2(\varsigma, w) \rangle - \langle \Delta U_{Tot}(\varsigma, w) \rangle^2]^{\frac{1}{2}}. \tag{2.14}$$

This results in

$$\sigma_{\Delta U_{Tot}}(\varsigma, w) = \left(\frac{\zeta}{\sqrt{3}b}\right)^{\frac{1}{2}} \Delta \tilde{E}_p(w), \tag{2.15}$$

where

$$\Delta \tilde{E}_p(w) = \left[\sum_{i,j}^{n} c_n \left\{ \left(\bar{U}^n(x_i - w, y_j) - \bar{U}^n(x_i, y_j) \right)^2 + \sigma_{\Delta U_{ij}^n}^2(w) \right\} \right]^{\frac{1}{2}}, \tag{2.16}$$

where $\bar{U}^n(x_i, y_j)$ is the $U^n(x_i, y_j, z_k)$ averaged along the Z direction (the line direction of the dislocation), and $\sigma_{\Delta U_{ij}^n}(w)$ is the standard deviation of $\Delta U_{ij}^n(w) = U^n(x_i - w, y_j, z_k) - U^n(x_i, y_j, z_k)$. Depending on the fluctuation of the potential energy distribution expressed by **eq. (2.15)**, the dislocation adjusts the line shape to minimize the total energy of the system. Then, the total energy of the dislocation per unit length is the summation of the interaction energy change and line tension energy (Γ), given by

$$\Delta E_{tot}(\varsigma, w) = \frac{1}{2\zeta} \left[\frac{\Gamma w^2}{2\zeta} - \left(\frac{\zeta}{\sqrt{3}b}\right)^{\frac{1}{2}} \Delta \tilde{E}_p(w) \right]. \tag{2.17}$$

Minimization on ς in **eq. (2.17)** yields characteristic segment length ς_c at which ΔE_{tot} is minimized as

$$\varsigma_c(w) = \left(4\sqrt{3} \frac{\Gamma^2 w^4 b}{\Delta \tilde{E}^2{}_p(w)} \right)^{\frac{1}{3}}. \tag{2.18}$$

Minimization on w in **eq. (2.17)** requires to solve

$$\frac{\partial \Delta \tilde{E}_p(w)}{\partial w} = \frac{\Delta \tilde{E}_p(w)}{2w}. \tag{2.19}$$

This equation cannot be solved analytically but can be solved numerically. Then, characteristics bowing-out distance, w_c, at which ΔE_{tot} is minimized is obtained.

Now, it is assumed that the variation of the local potential energy of dislocations per unit length is approximated as

$$E(x) = \frac{1}{2} \frac{\sigma_{\Delta U_{Tot}}(\varsigma_c, w_c)}{\sqrt{2}\varsigma_c} \left[1 - \cos\left(\frac{\pi x}{w_c}\right) \right]. \tag{2.20}$$

The total energy barrier for dislocation motion per unit length is the energy cost of moving from a favorable to an unfavorable position over a distance w_c minus the gain in the line tension energy expressed as

$$\Delta E_b = \frac{\sigma_{\Delta U_{Tot}}(\varsigma_c, w_c)}{\sqrt{2}\varsigma_c} - \frac{\Gamma w_c^2}{4\zeta_c^2} = 1.22 \left(\frac{w_c^2 \Gamma \Delta \tilde{E}^2_{\ p}(w_c)}{b} \right)^{\frac{1}{3}}. \tag{2.21}$$

Then, it is considered that resolved shear stress of τ' is applied to the system at 0 K. When $E(x) - \tau' bx = 0$ where dislocations start moving, critical resolved shear stress (CRSS), $\tau(0 \text{ K})$ is expressed as

$$\tau(0 \text{ K}) = 1.01 \left(\frac{\Delta \tilde{E}^4_{\ p}(w_c)}{b^5 w_c^5 \Gamma} \right)^{\frac{1}{3}}. \tag{2.22}$$

At finite temperature (T) and finite strain rate $(\dot{\varepsilon})$, CRSS is reduced due to the help of thermal activation, given as

$$\tau(T, \dot{\varepsilon}) = \tau(0 \text{ K}) \left[1 - \left(\frac{k_B T}{\Delta E_b} \ln \frac{\dot{\varepsilon}_0}{\dot{\varepsilon}} \right)^{\frac{2}{3}} \right], \tag{2.23}$$

where k_B is the Boltzmann constant. $\dot{\varepsilon}_0 \sim 10^4 \ s^{-1}$ is a constant related to the thermal vibration frequency of atoms near the melting point (in metals, typically $\nu_0 \sim 10^{13} \ s^{-1}$) and expressed by Orowan's equation as $\dot{\varepsilon}_0 = \rho b d_s \nu_0$, where ρ and d_s are dislocation density and the slip distance of dislocations (equivalent to grain sizes). By calculating the

interaction energy between dislocations and alloying elements and putting it to **eq. (2.21),**
(2.22), and (2.23), the CRSS of materials at finite temperature and strain rate is obtained.

However, DFT calculation usually requires a high cost. So that, Varvenne *et al.*
[63,80] derived a simplified theory (so-called "reduced" theory). They found that the
contribution of $U^n{}_{\text{Chem}}$ is very small in the final results. Thus, they only considered the
effect of $U^{\text{Elast}}{}_n$. In the case, **eq. (2.16)** is simplified as

$$\Delta \tilde{E}_p(w_c) = -\left[\sum_{i,j}\{p(x_i - w_c, y_j) - p(x_i, y_j)\}^2\right]^{\frac{1}{2}} \times \left[\sum_n c_n\left(\Delta \bar{V}_n^2 + \sigma_{\Delta V_n}^2\right)\right]^{\frac{1}{2}}, \quad (2.24)$$

where $\sigma_{\Delta V_n}^2$ is the standard deviation of ΔV_n, which is assumed to be negligible. By putting
eq. (2.24), **eq. (2.22) and (2.21)** are simplified as

$$\tau(0 \text{ K}) = 0.051\alpha^{-\frac{1}{3}}Gb^{-4}\left(\frac{1 + v}{1 - v}\right)^{\frac{4}{3}}f_1(w_c)\left[\sum_n c_n\Delta \bar{V}_n^2\right]^{\frac{2}{3}}, \quad (2.25)$$

$$\Delta E_b = 0.274\alpha^{\frac{1}{3}}Gb\left(\frac{1 + v}{1 - v}\right)^{\frac{2}{3}}f_2(w_c)\left[\sum_n c_n\Delta \bar{V}_n^2\right]^{\frac{1}{3}}, \quad (2.26)$$

respectively. α is the line tension parameter of dislocations in the material, and f_1 and f_2
are functions related to SFE. The difference of the slopes among various alloys shown in
figure 2.10 (b) is considered to be related to these parameters (See Appendix A). The
calculations in FCC HEAs and MEAs yielded $\alpha = 0.06125$, and $f_1(w_c)$ and $f_2(w_c)$ are
approximated as 0.35 and 5.70, respectively [63]. This theory successfully predicted the
strength of various solid solution alloys with FCC structures [36,37,84,85,63,72,78–83].
The model was also found to be applicable to the edge dislocations in BCC HEAs [86,87].
In addition, it should be noted that this model can be mathematically proven to be
equivalent to the mean-field Labusch model (See Appendix A) and the correlation

between the CRSS and mean square atomic displacement proposed by Okamoto *et al.* [41,88] under reasonable assumptions.

Figure 2.11 (c) shows the comparison between the experimental and theoretical values of friction stress at room temperature with a strain rate of 8.3×10^{-4} s^{-1}. The theoretical values were calculated by the Leyson-Varvenne model (**Eq. (2.25), (2.26), and (2.23)**) based on the atomic volumes shown in **table 2.3** assuming Taylor factor of random texture (= 3.06). It should be noted that the friction stress of pure Ni was added to the values calculated by the model as intrinsic friction stress of FCC crystal lattices (Mainly dominated by the phonon-drag effect [46]). In addition to the experimental data in the present study, the friction stress values of $(CoFeMnNi)_{94}M_6$ (M: V, Ti, Mo, Cu, Cr, Al) [89], CoNiV [90], and Ni_2Cr ($Ni_{66.6}Cr_{33.3}$) [72] (at.%) at room temperature were extracted from literature and plotted together. Good agreement was found between the experimental and theoretical values, implying that the elastic interaction between dislocations and alloying elements was a dominant factor determining the friction stress in FCC HEAs and MEAs.

2.4.4. Other possible contributing factors for strengthening

In conventional dislocation theory, dislocations in crystal lattices of random dilute alloys are thought to interact mainly with elastic fields around solute atoms caused by the effect of atomic size misfit and modulus misfit (as illustrated in **figure 2.12 (a)**), resulting in solid-solution strengthening. In this case, the local potential energy for a dislocation segment in dilute alloys, ΔE_{DA}, can be given as the superposition of the local Peierls potential energy in the solvent pure metal, ΔE_{PM}, and the energy contribution of lattice distortion caused by the solute atom, ΔE_{LD}, (**Figure 2.12 (c)**). The average potential

energy along the dislocation line, $< \Delta E_{\mathrm{DA}} >$, can be obtained as a composite of ΔE_{PM} and ΔE_{LD} ($\langle \Delta E_{\mathrm{DA}} \rangle = \sqrt{\langle (\Delta E_{\mathrm{PM}})^2 \rangle + \langle (\Delta E_{\mathrm{LD}})^2 \rangle}$) (**Figure 2.12 (e)**). (See Appendix B for the mathematical background of the additivity.) Due to the contribution of ΔE_{LD}, dislocations have to overcome potential energy (ΔE_{DA}) larger than the case of pure metals (ΔE_{PM}) resulting in strengthening. It should be noted that these discussions can be valid if solid solutions are "random" and solute-solute interaction is negligible.

Similar to the dilute alloys, an effect of "severe" lattice distortion seems to mainly contribute to strengthening in HEAs and MEAs as considered the effect of lattice distortion using the mean-field Labusch model and Leyson-Varvenne model. Although there was good agreement between the experimental and theoretical values in **figure 2.11 (c)**, a small deviation ($\sim 10^1$ MPa) from the theory was found in some of the alloys. There are several possible reasons, such as the effect of (1) dislocation core structure [63] contributing to f_1 and f_2 in **eq. (2.25) and (2.26)**, (2) chemical interaction between dislocations and alloying elements (U^n_{Chem}) [80], (3) temperature dependence of dislocation line tension energy [81] contributing to α in **eq. (2.25) and (2.26)**, and (4) inaccuracy of atomic volumes (misfit volumes) of each element, which can be refined by precise experimental measurements [72].
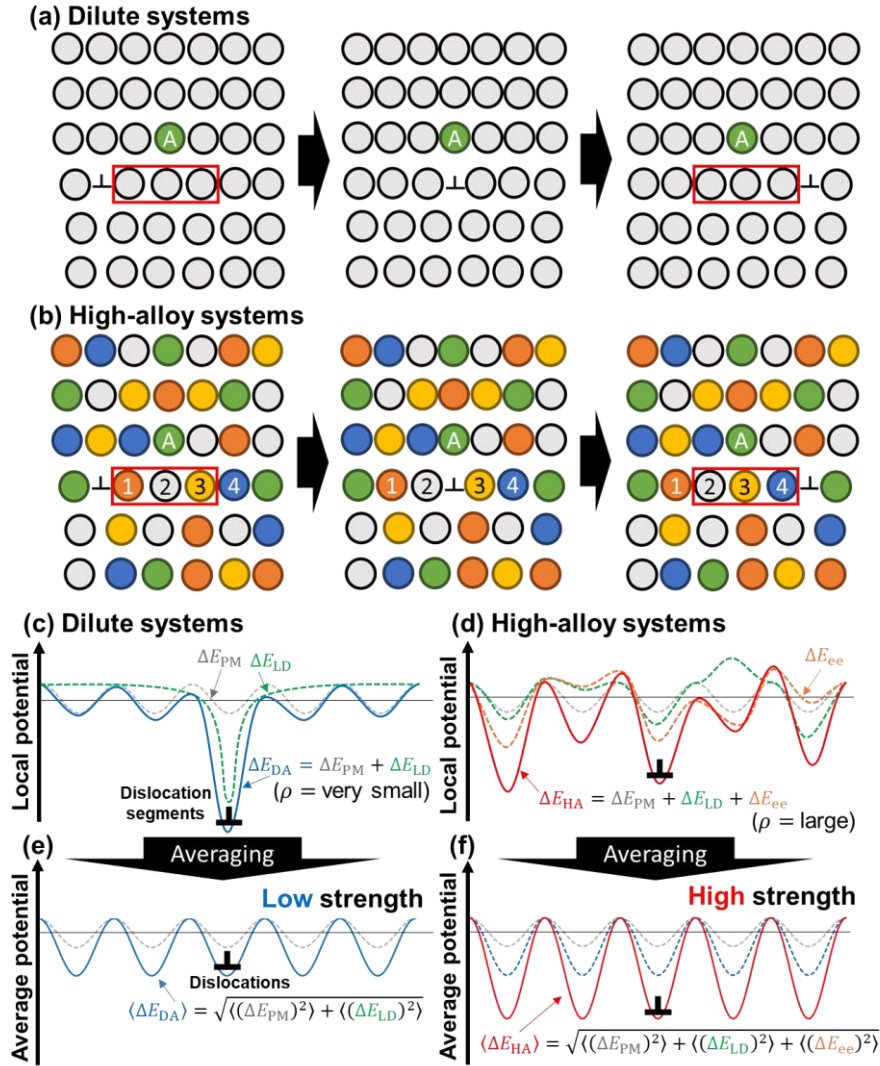
Figure 2.12: Schematic illustrations showing changes in the arrangement of neighboring atoms caused by a dislocation slip in FCC crystal lattices of (a) a dilute solid solution and (b) a high-alloy system like HEAs and MEAs, respectively. Local Peierls potential energy profiles around a dislocation segment* are schematically illustrated in (c) for the dilute system (corresponding to (a)) and (d) for the high-alloy system (corresponding to (b)). (* it is considered that the potential is different at segment by segment even along one dislocation line since the arrangement of atoms also differs along the dislocation.) ΔE_{DA} (blue line in (c)) and ΔE_{HA} (red line in (d)) are the local Peierls potential energy for a dislocation segment in dilute and high-alloy systems, respectively. ΔE_{PM}, ΔE_{LD}, and ΔE_{ee} shown in (c) and (d) indicate the energy contribution for ΔE_{DA} and ΔE_{HA} by lattice friction in pure FCC metals, lattice distortion, and the effect of element-element interaction, respectively. Distributions of the average total potential energies for dislocation (($<\Delta E_{DA}>$ for dilute alloys and $<\Delta E_{HA}>$ for high alloys), which were obtained by averaging the local potential energies shown in (c) and (d) along the dislocation line, are shown in (e) and (f), respectively. The angle brackets indicate the average values of physical quantities. Equations for convoluting $<\Delta E_{DA}>$ and $<\Delta E_{HA}>$ are inserted in the figures.

Another possibility is (5) the heterogeneity of elemental distribution (i.e., deviation from the ideal random state), which has been under passionate debate recently [72,91,100–102,92–99]. In general, elements are not always distributed randomly but inhomogeneously to minimize elastic and electromagnetic interaction energy between constituent elements in an equilibrium state. In case of that there is an attractive interaction between elements, for instance, they tend to form order by periodically arranging different elements. If the periodicity persists in a scale of several atoms, the phenomenon is called short-range ordering (SRO). On the other hand, if the periodicity persists in a scale of grains, the phenomenon is called long-range ordering (LRO), where crystal structure can be described by defining sublattices. In case of that there is a repulsive interaction between elements, the same kinds of elements tend to form clusters in a solid solution, which is called clustering. Particularly, the case of clustering persisting in a scale of several atoms is called short-range clustering (SRC). When a dislocation passes through the inside of ordered or clustered regions, the most stable arrangement of elements (SRO or SRC state) can be destroyed by shifting one atomic plane along Burger's vector which causes extra resistance to the dislocation motion leading to strengthening. Since various kinds of elements with higher concentrations are mixed in high-alloy systems, the interaction between constituent elements (element-element interaction) in concentrated solid solutions can be inherently diverse. For example, Inoue *et al*. (Unpublished) found direct evidence of SRO with a structure similar to $L1_2$ or $L1_0$ in CoCrNi MEA (annealed at 700 ℃ for 2 weeks) by using atom probe tomography. However, they also found that the mechanical properties of the MEA with SRO were identical to those without SRO (with a weaker SRO level). Similarly, other groups also reported that the mechanical properties of CoCrNi MEA [72] and CoCrFeMnNi HEA

[102] were independent of annealing temperature. Since the stability of the SRO state is temperature-dependent, these results imply that the effect of SRO on the mechanical properties is negligible in the subsystems of CoCrFeMnNi HEA presented in this study. In contrast, Zhang *et al*. [93] reported that yield strength of CoCrNi MEA could increase if furnace-cooling (very slow cooling rate) was employed, and they attributed it to the formation of SRO in the MEA. Further study is necessary to clarify the effect of processing conditions on the formation kinetics of SRO and its impact on the mechanical properties of HEAs and MEAs in the future.

Even if the effect of SRO is negligible, element-element interaction[*] (chemical interaction among alloying elements) can contribute to strengthening in another way. ([*]The interaction among alloying elements was named as element-element interaction, different from "solute-solute interaction" because it is impossible to distinguish between solutes and solvents in HEAs and MEAs.) This is not simply because the element-element interaction often increases the value of $\varepsilon_{\mathrm{ave}}$. For example, now, it is considered that an FCC crystal lattice of a high-alloy system containing an edge dislocation illustrated in **figure 2.12 (b)**, where neighbors of the atom A (of an element) are the elements 1, 2, and 3 in the initial state, and it is assumed that there are attractive interactions between atom A and element 1 and repulsive interaction between atom A and element 4. After the dislocation passing through, the neighbors of atom A changes to the elements 2, 3, and 4 shifting one atomic plane along Burger's vector, where atom A leaves the element 1 and meets the element 4. In such a case, extra activation energy, ΔE_{ee}, essentially derived from the change in bonding energy and lattice strain energy caused by the change of the local arrangement of elements, should be required for dislocations to move in the crystal lattice in addition to ΔE_{PM} and ΔE_{LD}, as shown in **figure 2.12 (d)**. It should be noted that the

interaction with only first-neighboring elements was considered to simplify the discussion, but, in some elemental combinations, higher-order neighbors should be taken into account [103]. Similar consideration was formulated for the dislocation cross slip in FCC binary alloys with various solute-concentration by Nöhring and Curtin, recently [103,104].

In dilute alloy systems, the change in the atomic arrangement around solute atoms before and after a dislocation passes through rarely happens because the majority of atoms are the solvent element, and the effect of the inhomogeneity of solid solution on the strength can be limited. In this case, it is enough to consider only the effect of lattice distortion, as Labusch did [45]. Exceptions are the alloys showing relatively strong solute-solute interaction and SRO or SRC such as Al-Mg alloys [105]. On the other hand, in high-alloy systems, since the concentration of alloying elements is high, even weak element-element interaction can have a significant impact on the strength. The local rearrangement of elements around the dislocation core would lead to a larger fluctuation of local potential energy for a dislocation segment in high-alloy systems, $\Delta E_{\mathrm{HA}} = \Delta E_{\mathrm{PM}} + \Delta E_{\mathrm{LD}} + \Delta E_{\mathrm{ee}}$, (**Figure 2.12 (d)**). By averaging them along the dislocation line, it is possible to obtain average potential energy for a dislocation in high-alloy systems, $\langle \Delta E_{\mathrm{DA}} \rangle = \sqrt{\langle (\Delta E_{\mathrm{PM}})^2 \rangle + \langle (\Delta E_{\mathrm{LD}})^2 \rangle + \langle (\Delta E_{\mathrm{ee}})^2 \rangle}$, (**Figure 2.12 (f)**), which is larger than that ($<\Delta E_{\mathrm{DA}}>$) in dilute alloys even having similar average lattice distortions to the high-alloy systems, resulting in an additional strengthening effect in high-alloy systems. This effect has been omitted in conventional dislocation theory, but Nag *et al.* [106] recently constructed a theoretical model considering the effect of the element-element interaction. They clearly showed that the element-element interaction can increase the yield strength of HEAs and MEAs by ~ 10^1 MPa depending on chemical composition. This agrees with

the order of magnitude of the deviation from the Leyson-Varvenne model in **figure 2.11 (c)**. A similar idea has been employed to understand the sluggish diffusion kinetics of HEAs. Tsai *et al.* [18] considered the change in the local interaction energy of elements when a vacancy migrated to rearrange neighboring atomic configurations around the vacancy and found that the standard deviation of the change in the local potential energy in CoCrFeMnNi HEA was much larger than those in austenitic stainless steels and other pure metals. Finally, they concluded that the larger fluctuation of local potential energy led to the slower vacancy migration kinetics compared to conventional dilute systems and pure metals, i.e., the sluggish diffusion kinetics in HEAs. Consequently, the migration of crystal defects (vacancies (0-dimensional) and dislocations (1-dimensional)) accompanying the local element-element interaction plays an important role to determine the essential nature of high-alloy systems such as MEAs and HEAs, which leads to inhibiting the migration of crystal defects compared to conventional dilute alloys and pure metals, resulting in, for example, the significant strengthening and the sluggish diffusion kinetics corresponding to the migration of dislocations and vacancies, respectively.

2.5. Conclusion

The mechanism and essential nature of strengthening in various equi-atomic multicomponent systems (high entropy alloys and medium entropy alloys) composed of Co, Cr, Fe, Mn, and Ni were experimentally studied. Fully-recrystallized specimens with FCC single-phase microstructures with various grain sizes could be successfully obtained in various MEAs by HPT and subsequent annealing. Systematic tensile tests confirmed the accurate and reliable Hall-Petch relationships, where extra-hardening phenomena accompanying discontinuous yielding in their stress-strain curves were observed in the

ultrafine-grained alloys. The strengthening mechanisms in high-alloy systems were discussed by comparing the friction stress experimentally obtained with the theoretical models. The important results obtained in the present study are as follows:

1) The experimental values of the friction stress for the HEA and MEAs were found to fit with the mean-field Labusch model and Leyson-Varvenne model very well, indicating that the strength of the alloys was closely correlated with their heterogeneously-distorted crystal lattices acting as high-density obstacles for dislocation motion. It was also found that the average lattice distortion in dilute alloys could be comparable to that in MEAs and HEAs although the higher lattice distortion in HEAs had been believed to be the reason for the higher strength than dilute alloys.

2) A strengthening mechanism due to element-element interaction was proposed, as an additional mechanism operating in high-alloy systems. Considering the atomic rearrangement mechanism, which was also considered for the slow vacancy migration kinetics in CoCrFeMnNi HEA, the inhibition of the movement of crystal defects (such as dislocations and vacancies) due to the element-element interaction can have a significant impact on the properties (such as strength and diffusivity) in high-alloy systems like HEAs and MEAs.

Above all, it is concluded that, in FCC HEAs and MEAs, the strength is mainly determined by the elastic interaction between dislocations and atomic size misfit (severe lattice distortion) and possibly chemical interaction among alloying elements (element-element interaction).

Chapter 3: Characteristic deformation microstructure evolution and deformation mechanisms

3.1. Introduction

Dislocations play an essential role in the plastic deformation of metallic materials. If shear stress larger than CRSS is applied to bulk materials, dislocations start moving, resulting in macroscopic yielding. Furthermore, as deformation proceeds, dislocations and other crystal defects (stacking faults and deformation twins (DTs)) spontaneously form characteristic morphology, so-called dislocation microstructure or deformation microstructure. Previous studies showed that, with increasing strain level, such dislocation microstructure evolved into some distinct patterns depending on the crystal structure, activated slip systems (deformation modes), crystal orientation, SFE, and grain size. For example, Huang *et al*. found that the dislocation microstructure of tensile deformed pure Al [107] and Cu [108] (with FCC structure) having large grain size could be classified into three types depending on the grain orientation against tensile axis (TA): (Type I) Grains are subdivided by long and straight dislocation cell boundaries along {1 1 1} planes; (Type II) Grains are subdivided by dislocation boundaries defining a three-dimensional cell structure; (Type III) Grains are subdivided by the similar structure as (I) but having boundaries deviated from {1 1 1} planes. This classification was found to be consistent with the deformation microstructure observed in single crystals having similar orientations. It was also suggested that Type II structure could be more elongated and aligned along TA with decreasing SFE [109]. The difference in these deformation microstructures was considered to be attributed to the difference in activated slip systems in each grain, leading to different dislocation reactions [110–112]. Le *et al*. [113] reported the deformation microstructure of tensile-deformed Al with various mean grain sizes. They found that, with decreasing grain size, Type I and III structure were gradually mixed, and the materials having a mean grain size smaller than several μm only showed

dislocation cells (DCs) and randomly-tangled dislocation structures. This implied that grain boundaries could affect the formation of deformation microstructure in fine-grained materials. Most importantly, these deformation structures are responsible for the work-hardening of metals. Hughes and Hansen [114] showed that the flow stress of metals could be explained by theoretical formulas in which inputs were structural parameters extracted from the actual deformation microstructure. Therefore, the careful characterization of the deformation microstructure is significantly important to understand the underlying physics of the plastic deformation in metals.

In contrast, compared with the results of pure FCC metals explained above, superior mechanical properties (strength-ductility balance) and different deformation microstructures have been reported in high-alloy systems, such as high-Mn steels [115,116], Hadfield steels [117–120], and high-nitrogen steels [121–124]. Gutierrez-Urrutia *et al*. [115,116] investigated the deformation microstructure in a tensile-deformed Fe-Mn-Al-C TWIP steel (SFE: $\gamma = 63$ mJm^{-2}). They reported planar slip of dislocations along specific {1 1 1} planes and the subsequent formation of planar dislocation structure (PDS) with Taylor lattices. With increasing the strain level, development of DCs in TA ~// <0 0 1> oriented grains and fine cell blocks (CBs), in which PDS were subdivided by incidental dislocation boundaries (IDBs), in other grains. In addition, DTs were observed in TA ~// <1 1 1> oriented grains. The work-hardening behavior of the TWIP steel was found to be directly linked to the deformation microstructure development. The equivalent results in a Fe-Mn-Al-Si TWIP steel ($\gamma < 40$ mJm^{-2}) were reported by Ueji *et al*. [125]. The deformation microstructure development in HEAs/MEAs has been also reported by several groups, recently. Laplanche *et al*. investigated the deformation microstructure of polycrystalline CoCrFeMnNi HEA [126] and CoCrNi MEA [34], and

these alloys also exhibited deformation microstructure development which was very similar to those in the TWIP steels (i.e., the formation of PDS, fine CBs, DCs, and DTs). Similar results have been also reported in single-crystalline FCC HEAs with similar crystal orientations [127–135]. It is generally believed that the formation of these planar dislocation structures like PDS and fine CBs is attributed to low SFE [136] or SRO [137], which makes dissociated screw dislocations lying on {1 1 1} planes difficult to cross-slip. However, some of the TWIP steels showing planar dislocation structure were found to be without any evidence of SRO and have SFE similar to pure Cu [116] that showed non-planar dislocation structures [108]. This implies that there should be additional factors contributing to deformation microstructure development which lead to the superior strength-ductility balance in FCC high-alloy systems, other than SFE. Despite the great effort described above, the quantitative understanding of the effect of alloying on the deformation microstructure development and its relation to the mechanical properties has not been attained due to the lack of systematic studies. Revealing such additional factors can be of great significance for the general understanding of the deformation mechanisms in metallic materials.

One important difference between high-alloy systems and dilute systems can be the magnitude of yield strength. In Chapter 2, it was revealed that the high yield strength of high-alloy systems like HEAs and MEAs was attributed to high friction stress (fundamental resistance to dislocation motion in a crystal lattice), reflecting the interaction between the elastic field of dislocations and atomic size misfit of alloying elements [45,46,63,64,72,76,80,138]. High-alloy systems are essentially heterogeneous on an atomic-scale because different alloying elements occupy different lattice sites, and the crystal lattice can be highly-distorted owing to the difference in the atomic size. This

leads to larger values of atomic size misfit (i.e., Severe lattice distortion) and higher friction stress in high-alloy systems compared with dilute systems. Thus, high friction stress can be characterized as one of the essential characteristics of high-alloy systems. Based on that, it was hypothesized that the high friction stress in high-alloy systems might be a key to reveal the additional factors affecting the deformation behavior of FCC metals. For FCC HEAs and MEAs having high friction stress such as CoCrFeMnNi HEA [139] and CoCrNi MEA [42], the Co-Ni binary system is a very suitable candidate for comparison because they have low friction stress close to pure Ni [42] and very similar materials properties (i.e., elastic constants, lattice constant, and homologous temperature) [60]. Also, their SFE can be controlled in a wide range by changing the atomic fraction of Co and Ni [140]. Thus, in the present study, the deformation behavior and deformation microstructure evolution in $Co_{60}Ni_{40}$ (at.%) alloy and $Co_{20}Cr_{40}Ni_{40}$ (at.%) MEA having the lowest and highest friction stress, respectively, among the subsystems of CoCrFeMnNi HEA [38,138,140–142] and having equivalent SFE and other materials properties were compared. The ultimate goal of this study is to clarify the special characteristics of deformation microstructure evolution in high-alloy systems and its relation to their macroscopic deformation behavior.

3.2. Materials and methods

3.2.1. Materials processing

Ingots of $Co_{60}Ni_{40}$ alloy and $Co_{20}Cr_{40}Ni_{40}$ MEA were fabricated by vacuum arc-melting of pure metals with a purity of more than 99.9 wt.% under inert gas (high-purity Ar) atmosphere. After the melting, they are cooled by a water-cooled copper mold, and they are flipped and re-melted five times to improve compositional homogeneity.

64

Afterward, the ingots were cold-rolled by 30 % reduction in thickness and subsequently homogenized at 1100 $^{\circ}$C for 24 h. Then, the materials were cold-rolled by 92% reduction in thickness and annealed at 750 $^{\circ}$C for 120 s and 850 $^{\circ}$C for 3.6 ks in the $Co_{60}Ni_{40}$ alloy and $Co_{20}Cr_{40}Ni_{40}$ MEA, respectively. After the processes, fully-recrystallized microstructures with FCC single-phase having the same mean grain size of about 3 μm (including annealing twins) were obtained in the alloys.

3.2.2. Microstructure observation of undeformed materials

Microstructure observation of undeformed materials was performed by using SEM (JSM-7800F, JEOL Ltd.) equipped with a BSE operated at an acceleration voltage of 25 kV and a probe current of 15 nA. The specimens for observation were mechanically polished by using SiC sandpapers with 1000 – 4000 grid sizes. Subsequently, they were electrically polished in a solution of 10 vo.% $HClO_4$ and 90 vol.% C_2H_5OH at 30 V for 15 s at room temperature to achieve a complete mirror surface.

3.2.3. Characterization of mechanical properties

Tensile tests were conducted at room temperature to evaluate the mechanical properties. Small-scaled dog-bone specimens with a gauge length of 2 mm and a gauge cross-section of 1 mm $\times$ 0.5 mm were cut from the recrystallized materials. Tensile deformation was applied with an initial strain rate of 8.3×10^{-4} s^{-1} until fracture. In-situ strain measurements were performed by employing the DIC method [143]. It should be noted that it was already confirmed in many previous studies that tensile tests with such small-scaled specimens and DIC methods give very reliable stress-strain curves equivalent to those measured by standard size specimens with extensometer (e.g.,

[42,138]). To investigate the deformation microstructure, tensile deformation was also interrupted at a nominal strain of 2, 10, 30, 50 %.

3.2.4. Microstructure observation of deformed materials

Deformation microstructure observation was conducted by using a transmission electron microscope (TEM) (JEM-2100 / 2100F) equipped with a bright field (BF) and annular dark field (ADF) detectors for scanning transmission electron microscopy (STEM), operated at 200 kV. The plane normal to the tensile specimen surface (plane parallel to TA) was observed. The specimens for the observation were mechanically polished until the thickness reached 50 μm by using SiC sandpapers with 1000 – 4000 grid sizes. Subsequently, they were electrically polished in a solution of 10 vo.% $HClO_4$, 20 vol. Glycerin, and 70 vol.% CH_3OH at 15 V at 243 K by using a twin-jet electropolishing machine (Tenupol-5, Struers Ltd.). The diffraction contrast of lattice defects was observed under the two-beam condition in both TEM and STEM [144–146]. The camera length of STEM detectors and the spot size of the electron beam were set as 40 cm and 1 nm, respectively, which were the optimal condition for deformation microstructure observation of the materials in the machine. The crystal orientation of each grain observed was determined based on the Kikuchi patterns formed by convergent electron beam diffraction analyzed by semi-automatic programs [147,148]. In each deformation condition, about 20-30 grains from two thin-foils were examined to obtain statistically reliable results.

3.2.5. Three-dimensional characterization of deformation microstructure

To reveal the three-dimensional morphology of dislocations in the tensile-deformed specimens, TEM-based electron tomography (ET) [149] was performed. In this technique, the diffraction contrast images of dislocations are acquired with a wide range of tilt angles. Then, the three-dimensional structure of dislocations is reconstructed by mathematical algorithms. As the diffraction contrast of dislocations is strictly dependent on diffraction conditions (g-vector), all the images need to be taken with the same g-vector in which targeted dislocations are visible. The recent development of the technique has been reviewed by several groups [150–152].

ET of 5 % deformed $Co_{20}Cr_{40}Ni_{40}$ MEA was conducted in FEI TECNAI G20 operated at 200 kV. The thin foils for ET were fabricated under the same condition described in Section 2.4. The specimen was attached to the high-angle triple-axis TEM holder (HATA-holder) (Mel-Build) with maximum tilt angles of $\pm$ 80° and $\pm$ 7.5^o in X- and Y-axis, respectively. A stable two-beam diffraction condition with a g-vector of g = <3 1 1> was kept during tilting. A series of weak-beam dark-field (WBDF) TEM images was acquired in a tilt-angle range of $\pm$ 50° along X-axis with an interval of 1.0^o. The acquired images were aligned by Inspect3D software (Thermo Fischer Scientific), and dislocation structures were then reconstructed by the weighted back-projection algorithm [153] with Avizo software (Thermo Fischer Scientific).

3.2.6. In-situ X-ray diffraction measurement during tensile deformation

To quantify the deformation behavior of the materials, in-situ XRD measurements during tensile deformation were conducted in a synchrotron radiation facility, the beamline 46XU at Super Photon ring – 8 GeV (SPring-8) in Hyogo, Japan. Dog-bone specimens having a gauge length of 10 mm and a gauge cross-section of 3 mm $\times$ 0.5 mm

67

were cut from the same recrystallized materials described in Section 2.1. Tensile deformation was applied in a load frame attached to a goniometer at room temperature with an initial strain rate of 8.3×10^{-4} s^{-1} until fracture. Incident X-ray beam with energy of 30 keV (wavelength of 0.0413 nm) and spot size of 0.3 mm (in length) $\times$ 0.5 mm (in width) was irradiated on the center of the gauge part of the tensile specimens. The beam was perpendicular to the plane normal to the tensile specimen surface. Transmission-diffracted X-ray beams were detected by a one-dimensional semiconductor detector (MYTHEM, Dectris) covering a 2θ range of 5° - 35°. It should be noted that the grains where diffraction occurred were oriented close to TA ~// <$h \ k \ l$> due to small values of 2θ. The exposure time (data acquisition time) was set to be 1.0 s to achieve a better signal-noise ratio, and diffraction profiles were continuously collected during deformation. The incident X-ray beam was precisely monochromated by a double mirror silicon monochromator. The camera length between the specimens and detector was adjusted by a computer-controlled four-axis goniometer. The system was calibrated by using a standard CeO$_2$ sample before measurement.

The peaks were fitted by the pseudo-Voigt function to obtain the peak position and integral intensity. Dislocation density and planar fault probability of the materials were estimated by the convolutional multiple whole profile fitting (CMWP) method [154]. For the analysis, {$h \ k \ l$} ($h \ k \ l$ = 1 1 1, 2 0 0, 3 1 1, 2 2 2, and 3 3 1) peaks of FCC structure were used. One should be cautious that the XRD line profiles of undeformed specimens can be broadened due to the chemical heterogeneity in high-alloy systems distorting crystal lattice. This can result in the overestimation of dislocation density. So that, the XRD profiles of deformed specimens were deconvoluted based on that of the undeformed

68

specimens to remove the effect of chemical heterogeneity, as proposed by Heczel *et al.* [155].

3.3. Results

3.3.1. Materials properties and microstructure of undeformed materials

The materials properties of the $Co_{60}Ni_{40}$ alloy and $Co_{20}Cr_{40}Ni_{40}$ MEA are listed in **table 3.1**.

Table 3.1: Materials properties of the $Co_{60}Ni_{40}$ alloy and $Co_{20}Cr_{40}Ni_{40}$ MEA measured experimentally and extracted from literature [60,138,140,141].

Materials properties	$Co_{60}Ni_{40}$ alloy	$Co_{20}Cr_{40}Ni_{40}$ MEA
Crystal structure	FCC single-phase	
Lattice constant, a / nm	0.3535	0.3559
Stacking fault energy, γ / mJm^{-2}	30 ± 5	
Homologous temperature at room temperature, T/T_m	0.170	0.173
Shear modulus, G / GPa	86	87
Mean grain size, d / μm	3.10	2.79
Hall-Petch slope, k / MPa m$^{1/2}$	181	168
Friction stress, σ_0 / MPa	52	280

The lattice constants in FCC structure were determined as 0.3535 nm and 0.3559 nm for the $Co_{60}Ni_{40}$ alloy and $Co_{20}Cr_{40}Ni_{40}$ MEA, respectively, based on the synchrotron XRD measurement before deformation. The friction stresses of the $Co_{60}Ni_{40}$ alloy and $Co_{20}Cr_{40}Ni_{40}$ MEA were determined as 52 MPa and 280MPa, respectively, based on the previous studies [42,138,142]. **Figure 3.1 (a) and (b)** show SEM-BSE micrographs of the initial microstructure of $Co_{60}Ni_{40}$ alloy and $Co_{20}Cr_{40}Ni_{40}$ MEA, respectively. Equiaxed grains with profuse annealing twin boundaries were seen in both the alloys. The
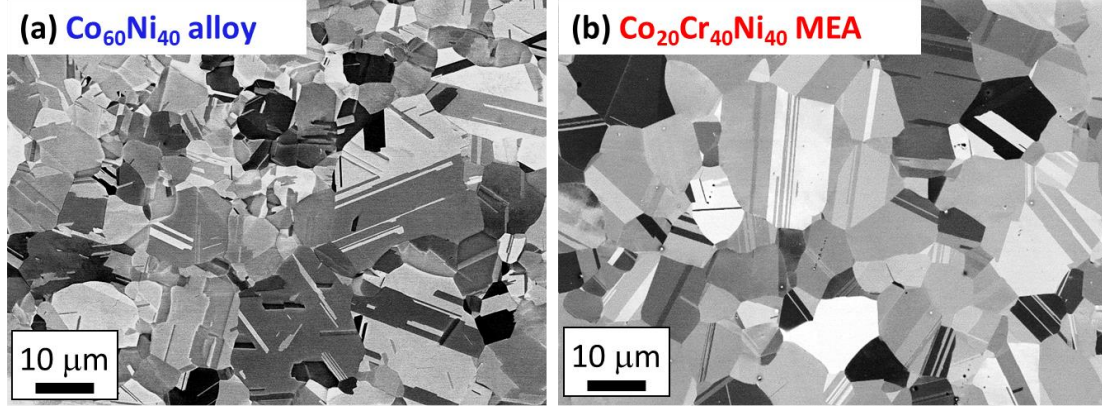
Figure 3.1: SEM-BSE micrographs of (a) $Co_{60}Ni_{40}$ alloy and (b) $Co_{20}Cr_{40}Ni_{40}$ MEA processed by cold-rolling by 92 % and subsequent annealing at 750 °C for 120 s and 850 °C for 3.6 ks, respectively.

texture of these materials was expected to be close to random due to the characteristics of the recrystallization texture in FCC metals [68]. The mean grain size of the $Co_{60}Ni_{40}$ alloy and $Co_{20}Cr_{40}Ni_{40}$ MEA were determined as 3.10 μm and 2.79 μm by the intercept method. Other materials properties (SFE, homologous temperature, shear modulus, and Hall-Petch slope) were extracted from the previous literature [60,72,138,156]. It should be noted that the accuracy of the SFE values of the materials in literature [140,141] was re-confirmed based on the separation distance of dissociated dislocations measured by WBDF-TEM [157]. **Figure 3.2 (a) and (b)** show the examples of dissociated dislocations in the $Co_{60}Ni_{40}$ alloy and $Co_{20}Cr_{40}Ni_{40}$ MEA. The separation distance of partial dislocations, *w,* could be directly measured based on the images. Also, the Burgers vectors of the dislocations can be determined. According to the theory [157], the relationship between the partial separation and SFE is expressed as

$$\gamma = \frac{Gb_p^2}{8\pi w}\left(\frac{2-v}{1-v}\right)\left(1 - \frac{2v\cos 2\beta}{2-v}\right), \tag{3.1}$$

where G, b_p, and v are shear modulus, Burgers vector of partial dislocations, and Poisson ratio, respectively. β is the angle between the direction of the Burgers vector and the line vector of a perfect dislocation. In **figure 3.2 (c)**, the measured values of *w* of the $Co_{60}Ni_{40}$

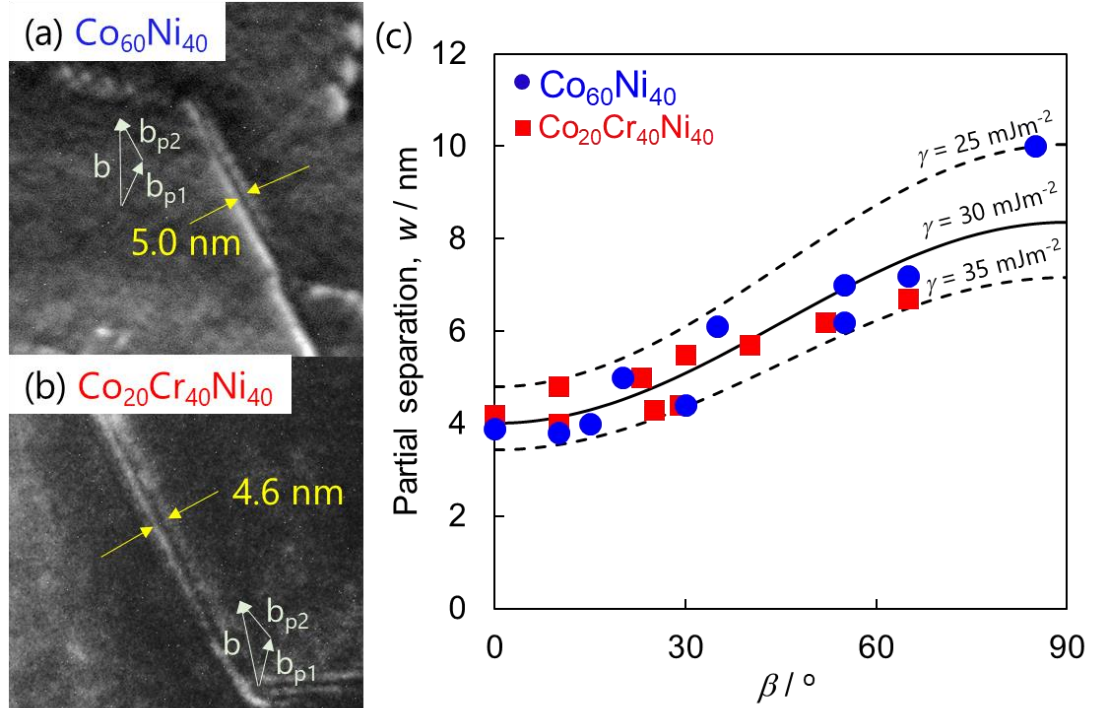**Figure 3.2**: Examples of WBDF-TEM images of dissociated dislocations in (a) $Co_{60}Ni_{40}$ alloy and (b) $Co_{20}Cr_{40}Ni_{40}$ MEA. The separation distance of partial dislocations and the Burgers vectors of two partials and perfect dislocations ($\boldsymbol{b} = \boldsymbol{b}_{p1} + \boldsymbol{b}_{p2}$) are indicated in the figures. (c) Measured separation distance of the partial dislocations in the $Co_{60}Ni_{40}$ alloy and $Co_{20}Cr_{40}Ni_{40}$ MEA as a function of β (angle between the Burgers vector and line vector of perfect dislocation). The solid and dashed curves were the ideal partial separation distance calculated by **eq. (3.1)** assuming $\gamma = 30 \pm 5$ mJm^{-2}.

alloy and $Co_{20}Cr_{40}Ni_{40}$ MEA were plotted together with the ideal curves for the $\gamma = 30 \pm 5$ mJm^{-2} cases. It was found that all the data fell in the range of $\gamma = 30 \pm 5$ mJm^{-2} in both alloys, as expected. Thus, it was concluded that the $Co_{60}Ni_{40}$ alloy and $Co_{20}Cr_{40}Ni_{40}$ MEA have the same SFE. It is also noteworthy that the average landscape of the generalized SFE and resulting twinability [158] in the materials are expected to be similar, according to the previous literature [159–162]. Based on the data above, it was clear that the materials properties of the $Co_{60}Ni_{40}$ alloy and $Co_{20}Cr_{40}Ni_{40}$ MEA were very close except for the friction stress.

3.3.2. Macroscopic tensile deformation behavior

Figure 3.3 (a) shows nominal stress – nominal strain curves of the $Co_{60}Ni_{40}$ alloy and $Co_{20}Cr_{40}Ni_{40}$ MEA, respectively. The yield strength (0.2% proof stress) of the $Co_{60}Ni_{40}$ alloy and $Co_{20}Cr_{40}Ni_{40}$ MEA were 140 MPa and 375 MPa, respectively. Since the Hall-Petch slopes of these materials are almost identical as shown in **table 3.1**, the difference in the yield strength (235 MPa) was well-coincide with the difference in the friction stress (228 MPa). The ultimate tensile strength of the $Co_{60}Ni_{40}$ alloy and $Co_{20}Cr_{40}Ni_{40}$ MEA were 419 MPa and 685 MPa, respectively. Generally, there is a trade-off relationship between the strength and ductility of materials. In other words, materials having higher strength tend to exhibit smaller ductility. However, despite the difference in the flow stress level, interestingly, both the alloys showed almost the same ductility (fractured at $e \sim 0.72$). **Figure 3.3 (b)** is the work-hardening rate curves of the $Co_{60}Ni_{40}$

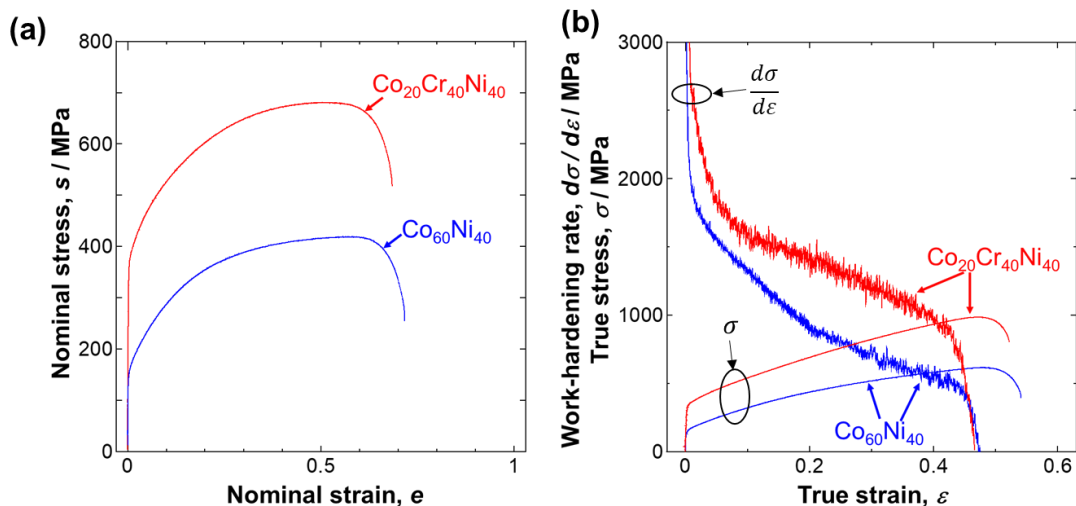**Figure 3.3**: (a) Nominal stress-nominal strain curves of the $Co_{60}Ni_{40}$ alloy (Blue) and $Co_{20}Cr_{40}Ni_{40}$ MEA (Red). (b) Work-hardening rate-true strain curves of the $Co_{60}Ni_{40}$ alloy (Blue) and $Co_{20}Cr_{40}Ni_{40}$ MEA (Red) plotted together with their true stress-true strain curves.

alloy and $Co_{20}Cr_{40}Ni_{40}$ MEA plotted together with the true stress – true strain curves. It was found that the work-hardening rate of the $Co_{20}Cr_{40}Ni_{40}$ MEA was higher than that of the $Co_{60}Ni_{40}$ alloy. The crossing points between the work-hardening rate curves and true stress – true strain curves are where necking occurs satisfying plastic instability condition [163] expressed as

$$\frac{d\sigma}{d\varepsilon} \leq \sigma, \qquad (3.2)$$

where σ and ε are true stress and true strain, respectively. Based on the **eq. (3.2)**, it was possible to understand that necking was retarded in the $Co_{20}Cr_{40}Ni_{40}$ MEA owing to the higher work-hardenability, resulting in a similar elongation as the $Co_{60}Ni_{40}$ alloy.

3.3.3. Orientation dependence of deformation microstructure evolution

To understand the reason for the difference in the work-hardenability in the materials, the deformation microstructure evolution in the materials was investigated.

(I) $Co_{60}Ni_{40}$ alloy

Figure 3.4 shows the deformation microstructure evolution in the tensile-deformed $Co_{60}Ni_{40}$ alloy with different applied strain levels. It was found that the microstructure could be classified into two types depending on the grain orientation against tensile axis (TA) as shown in **Figure 3.6 (a)**: (Type A) Randomly-tangled dislocations were seen at the early stage of deformation, and DCs with a size of several hundred nm developed with increasing the strain levels regardless of the orientation except for the grains oriented close to TA $\sim// <1\ 1\ 1>$; (Type A-T) DCs developed (Similar to the type A), and a small amount of DTs with a thickness of several tens nm were observed just before necking started ($e \sim 50$ %) in the grains oriented close to TA $\sim// <1\ 1\ 1>$. The appearance of DCs

was similar to the type II grains in tensile-deformed pure Cu, but the type I and III were not observed. This might be attributed to the effect of the small grain size as reported in pure Al [113]. However, further study is necessary to clarify the grain size dependence of deformation microstructure in low SFE materials, which is beyond the scope of this paper.
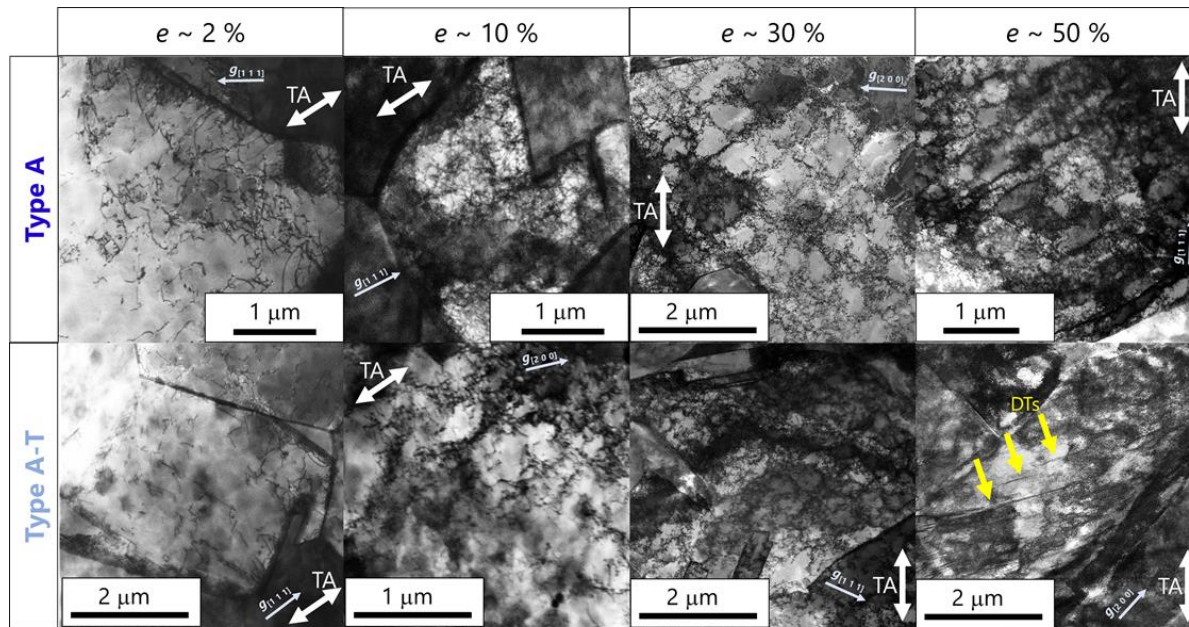
Figure 3.4: STEM micrographs of the two types of deformation microstructures (Type A and A-T) of the $Co_{60}Ni_{40}$ alloy depending on the applied strain up to $e \sim 50$ %. TA and g-vector ($g_{[h\,k\,l]}$) are indicated in each image. The plate-shaped defects in the image with Type A-T and $e \sim 50$ % indicated by yellow arrows are DTs.

(II) Co$_{20}$Cr$_{40}$Ni$_{40}$ MEA

Figure 3.5 presents the deformation microstructure evolution in the tensile-deformed Co$_{20}$Cr$_{40}$Ni$_{40}$ MEA with different strain levels. It was found that the microstructure could be classified into three types depending on the grain orientation as shown in **figure 3.6 (b)**: (Type A) Randomly-tangled dislocations were seen at the early stage of deformation, and DCs with a size of several tens nm developed with increasing the strain levels in TA ~// <1 0 0> oriented grains; (Type B) Planar slip of dislocations was seen at the early stage, and PDS were subsequently formed along one of {1 1 1} planes in all the grains except for those oriented to TA ~// <1 0 0> and TA ~// <1 1 1>; (Type B-T) PDS developed in one or two of {1 1 1} planes (similar to the type B), and DTs with a thickness of several nm started nucleating after the applied strain level of e ~ 10 % in TA ~// <1 1 1> oriented grains. It seemed that the number fraction of DTs increased with increasing the applied strain levels, while the thickness did not change. It should be noted that the PDS and DTs observed in type B and B-T grains were mainly lying on the {1 1 1} planes where there is the primary slip system, the <1 1 0> {1 1 1} slip system having the highest Schmid factor. The deformation microstructures in this alloy appeared to be very similar to those in both the single-crystals and poly-crystals of other FCC high-alloy systems with similar crystal orientation as described in Section 1.
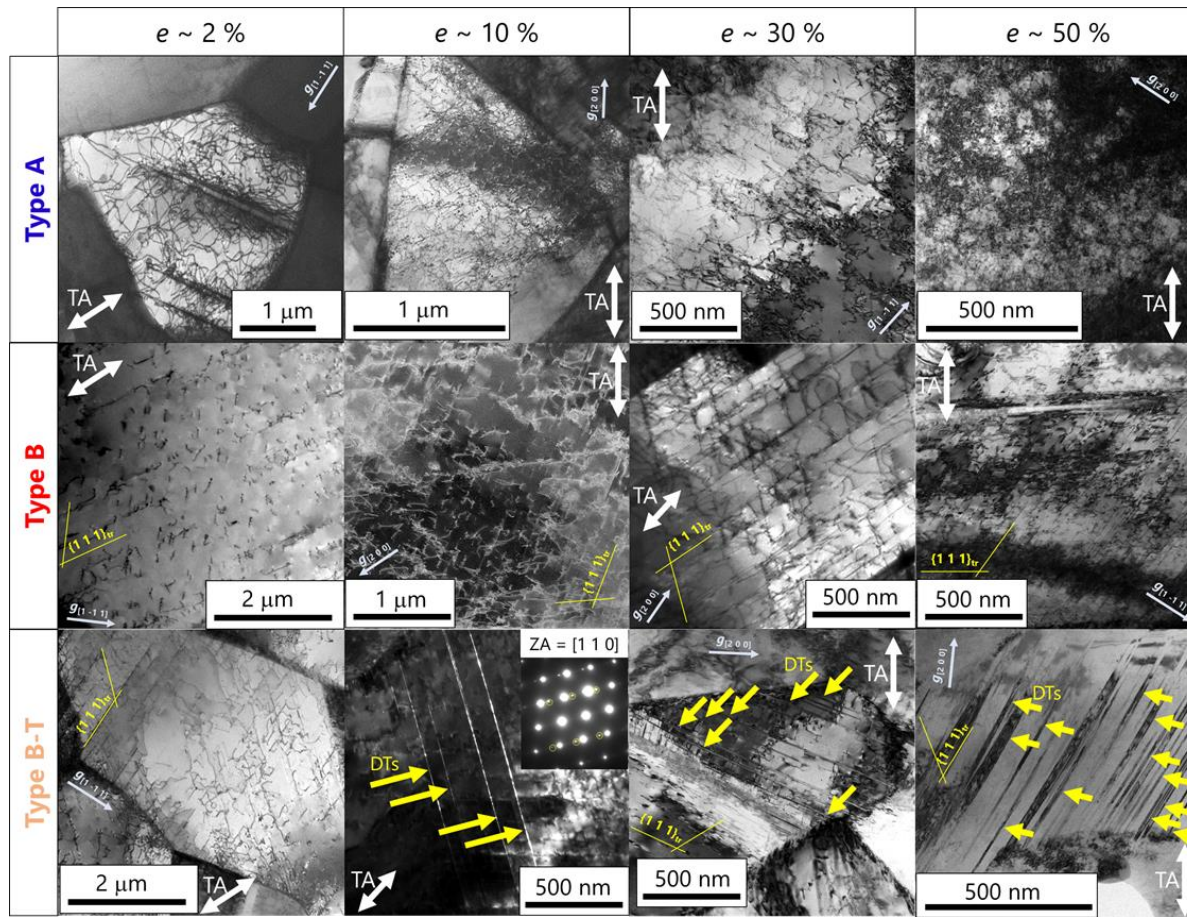
Figure 3.5: TEM/STEM micrographs of the three types of deformation microstructures (Type A, B, and B-T) of the $Co_{20}Cr_{40}Ni_{40}$ MEA depending on the applied strain up to $e \sim 50$ %. TA and g-vector ($g_{[h\,k\,l]}$) are indicated in each image. The plate-shaped defects in the images of Type B-T and $e \sim 10$ - 50 % indicated by yellow arrows are DTs. The inset in the dark-field TEM image of Type-B-T and $e \sim 10$ % displays a SAD pattern showing the presence of twins ($2n\,0\,0$ reflections of twins were indicated by yellow circles.).
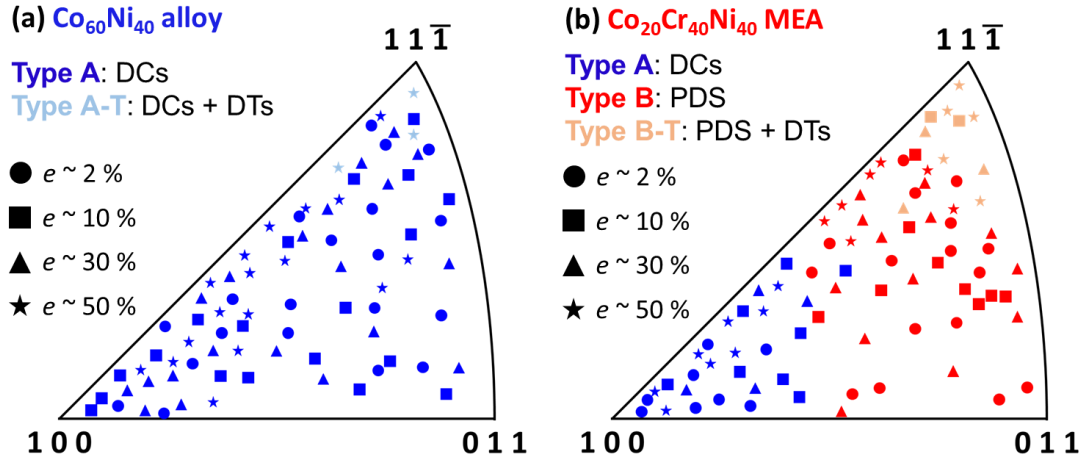
Figure 3.6: Types of deformation microstructures in (a) $Co_{60}Ni_{40}$ alloy and (b) $Co_{20}Cr_{40}Ni_{40}$ MEA classified depending on the grain orientation against TA and applied strain. Blue and light-blue data points indicate the grains having DCs and DCs + DTs, respectively. Red and orange data points indicate the grains having PDS and PDS + DTs, respectively.

3.3.4. Three-dimensional structure of PDS in the $Co_{20}Cr_{40}Ni_{40}$ MEA

The three-dimensional structure of PDS in the type B grains of the $Co_{20}Cr_{40}Ni_{40}$ MEA was revealed by ET. **Figure 3.7 (a-i)** show the WBDF-TEM images of the dislocation structure taken with different tilt-angles. Based on the images taken with different *g*-vectors, the Burgers vectors of the dislocations were determined according to the **$g \cdot b$** criteria [164]. It should be noted that dislocations in the material were dissociated into two Shockley partials and an intrinsic stacking fault (ISF) owing to the low SFE. For example, in **figure 3.7 (a)**, dislocations were identified as the following:

Slip system 1: $\quad \frac{a}{2}[1\,0\,\bar{1}]\,(1\,1\,1) \rightarrow \frac{a}{6}[2\,\bar{1}\,\bar{1}]\,(1\,1\,1) + ISF + \frac{a}{6}[1\,1\,\bar{2}]\,(1\,1\,1)$

Slip system 2: $\quad \frac{a}{2}[\bar{1}\,1\,0]\,(1\,1\,\bar{1}) \rightarrow \frac{a}{6}[\bar{1}\,2\,1]\,(1\,1\,\bar{1}) + ISF + \frac{a}{6}[\bar{2}\,1\,\bar{1}]\,(1\,1\,\bar{1})$

These dislocations were colored by red and blue in **figure 3.7 (a')**, and unknowns were colored by white. It was found dislocations belonging to these slip systems are confined in their slip planes forming PDS, implying the difficulty in cross-slip and dynamic

recovery during deformation. The edge-on views of the dislocations of the slip systems 1 and 2 aligned along the slip planes could be found in **figure 3.7 (f) and (c)**, respectively. Due to the planar structure of dislocations, these dislocations lying on the two different {1 1 1} planes intersected with each other resulting in the formation of the stair rod immobile dislocations [165]. For instance, one Lomer-Cottrell dislocation was found as indicated by the orange line in **figure 3.7 (a')**, possibly due to the dislocation reaction of

$$\frac{a}{6}[2\ \bar{1}\ \bar{1}]\ (1\ 1\ 1) + \frac{a}{6}[\bar{1}\ 2\ 1]\ (1\ 1\ \bar{1}) \rightarrow \frac{a}{6}[1\ 1\ 0]\ (0\ 0\ 1)$$

Generally, the formation of such immobile dislocations during deformation accelerates the dislocation multiplication, which leads to higher work-hardenability [165,166].
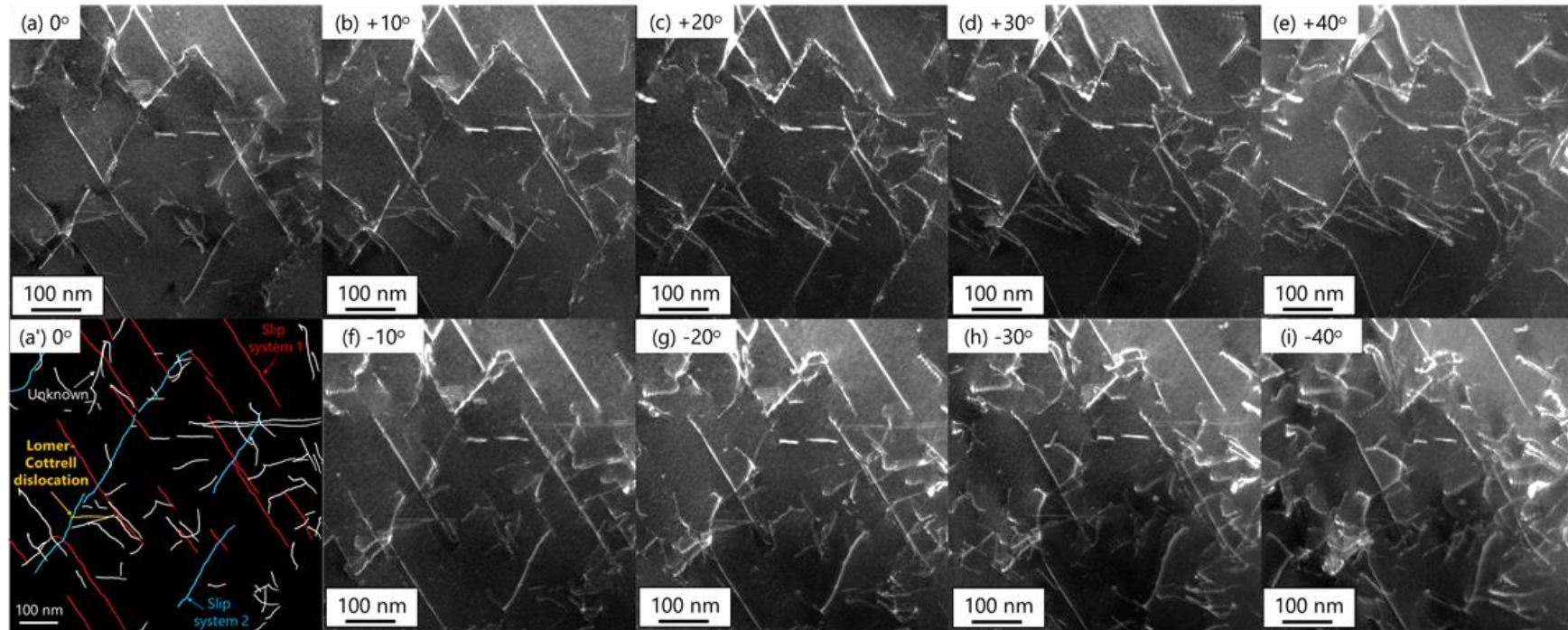
Figure 3.7: (a – i) WBDF images of the Type B microstructure in the $Co_{20}Cr_{40}Ni_{40}$ MEA with e ~ 5% taken under different tilt angles of the X-axis (± 40°). (a') Types of dislocations shown in (a) determined by TEM analysis. The red and blue lines are dislocations lying on two different slip planes. The orange line is a Lomer-Cottrell dislocation. The white lines are dislocations belonging to unknown slip systems.

3.3.5. Internal stress, texture, and defects density evolution during deformation

Since the structural information obtained by TEM was very local, macroscopic deformation behavior was investigated by using in-situ XRD measurement during tensile deformation. **Figure 3.8 (a) and (b)** show examples of {1 1 1} and {2 0 0} peaks in the XRD profiles of the $Co_{60}Ni_{40}$ alloy and $Co_{20}Cr_{40}Ni_{40}$ MEA during tensile deformation. No phase transformation was found in both alloys after deformation. Each peak shifted to the smaller angle side with increasing strain level, corresponding to elastic deformation of the grains oriented to TA ~// {h k l}. The amount of peak shift in the $Co_{20}Cr_{40}Ni_{40}$ MEA was larger than that in the $Co_{60}Ni_{40}$ alloy because of the difference in internal stress development. Peak-broadening was also confirmed with increasing applied strain due to the accumulation of lattice defects such as dislocations and deformation twins. The peak width of the $Co_{20}Cr_{40}Ni_{40}$ MEA was wider than that in the $Co_{60}Ni_{40}$ alloy because the density of dislocations and planar faults in the $Co_{20}Cr_{40}Ni_{40}$ MEA were higher than those in the $Co_{60}Ni_{40}$ alloy. In both alloys, the intensity of {1 1 1} peak increased with increasing applied strain, while that of {2 0 0} peak slightly decreased. It was noteworthy that the increment of the intensity of {1 1 1} peak in the $Co_{60}Ni_{40}$ alloy was much larger than that in the $Co_{20}Cr_{40}Ni_{40}$ MEA, suggesting different texture development.

Based on the shift of each peak, it is possible to investigate the elastic deformation in the grains having similar orientations [166]. The elastic strain (ε_{hkl}) in the grains oriented to TA ~// <h k l> is calculated as

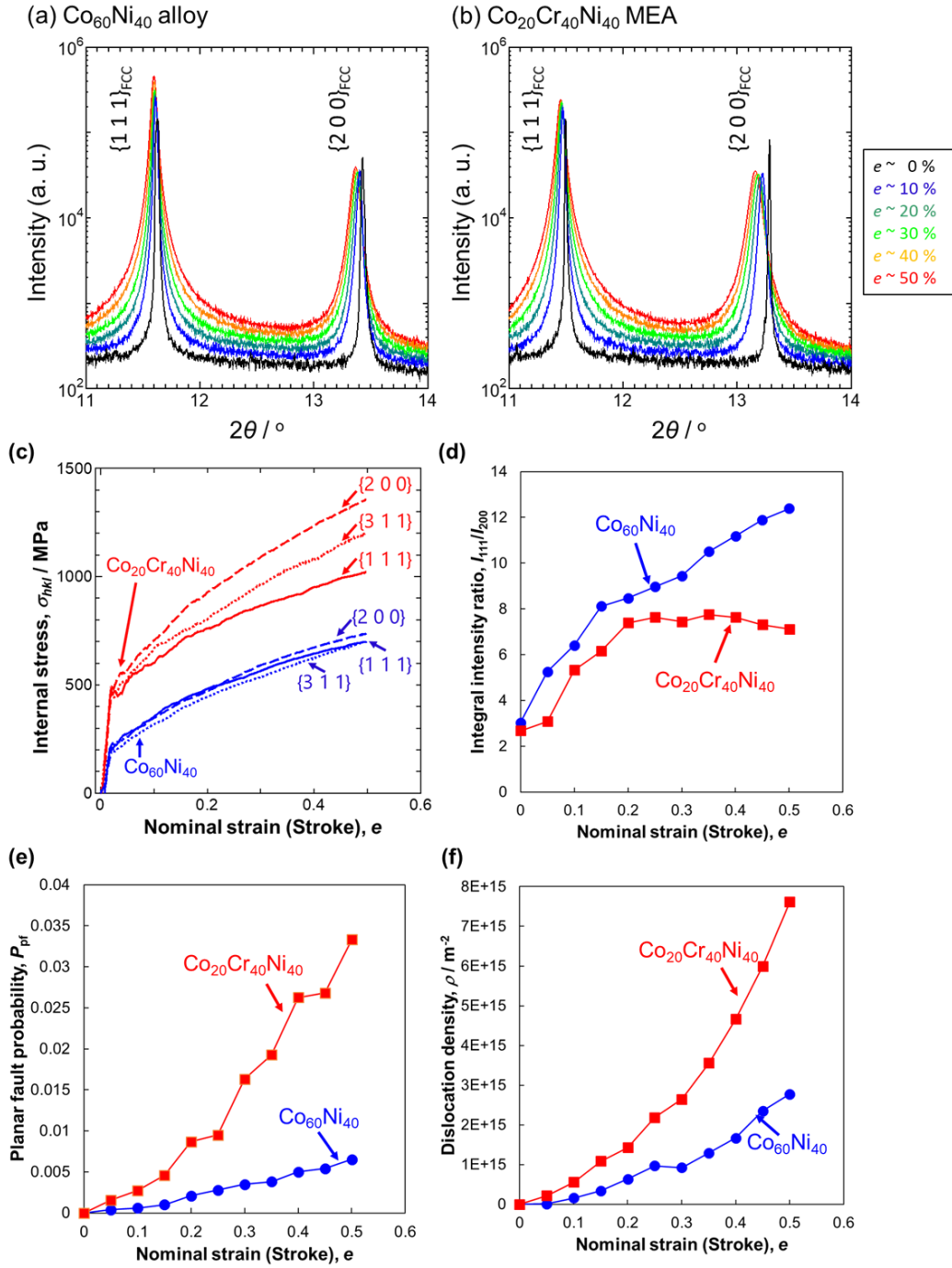$$\varepsilon_{hkl} = \frac{d_{hkl} - d_{hkl}^0}{d_{hkl}^0}, \qquad\qquad (3.3)$$

Figure 3.8: Examples of the XRD line profiles of (a) Co$_{60}$Ni$_{40}$ alloy and (b) Co$_{20}$Cr$_{40}$Ni$_{40}$ MEA. {1 1 1} and {2 0 0} peaks are enlarged from the whole profile. The y-axis is a log scale. The meaning of the colors is indicated in the figure. (c) Internal stress in the grains oriented to TA ~// <$h\,k\,l$> ($h\,k\,l$ = 1 1 1, 2 0 0, and 3 1 1), (d) Integral intensity ratio between 1 1 1 and 2 0 0 peaks, (e) Planar fault probability, and (f) dislocation density calculated by the CMWP method as a function of applied strain (calculated based on the stroke of the tensile test machine). The blue circles (or lines) and red squares (or lines) are corresponding to the data of the Co$_{60}$Ni$_{40}$ alloy and Co$_{20}$Cr$_{40}$Ni$_{40}$ MEA.

where d_{hkl} and d_{hkl}^0 are the lattice spacing of $\{h\,k\,l\}$ planes during deformation and before deformation, respectively. By multiplying diffraction elastic modulus (E_{hkl}), the internal stress (σ_{hkl}) in the grains oriented to TA ~// $<h\,k\,l>$ is calculated as

$$\sigma_{hkl} = E_{hkl}\varepsilon_{hkl}. \tag{3.4}$$

It should be noted that E_{hkl} can be determined by assuming that $\sigma_{hkl} = \sigma$ (applied stress) during elastic deformation [167]. E_{hkl} in the Co$_{60}$Ni$_{40}$ alloy and Co$_{20}$Cr$_{40}$Ni$_{40}$ MEA were estimated as presented in **table 3.2**. As E_{hkl} of the alloys are similar to each other, the elastic constants and anisotropy of these alloys are expected to be also similar [168]. The E_{hkl} values are also similar to other FCC high-alloy systems with low SFE reported previously (HEAs/MEAs and austenitic steels [167–170]).

Table 3.2: Diffraction elastic modulus (E_{hkl}) of the Co$_{60}$Ni$_{40}$ alloy and Co$_{20}$Cr$_{40}$Ni$_{40}$ MEA determined by in-situ XRD during tensile-deformation.

Materials	E_{111}	E_{200}	E_{311}
Co$_{60}$Ni$_{40}$ alloy	245 GPa	131 GPa	200 GPa
Co$_{20}$Cr$_{40}$Ni$_{40}$ MEA	254 GPa	139 GPa	191 GPa

In **figure 3.8 (c)**, the internal stress in the grains of the Co$_{60}$Ni$_{40}$ alloy and Co$_{20}$Cr$_{40}$Ni$_{40}$ MEA oriented to TA ~// $\{1\,1\,1\}$, $\{2\,0\,0\}$, and $\{3\,1\,1\}$ as a function of applied strain calculated based on the stroke of the tensile test machine was presented. It was found that the internal stress development in Co$_{60}$Ni$_{40}$ alloy was almost independent of $\{h\,k\,l\}$, while, in the Co$_{20}$Cr$_{40}$Ni$_{40}$ MEA, internal stress varied depending on the orientation. This suggested that deformation microstructure evolution in the Co$_{60}$Ni$_{40}$ alloy was homogeneous, while that in the Co$_{20}$Cr$_{40}$Ni$_{40}$ MEA was heterogeneous (i.e., Orientation dependent); This was very consistent with the results of deformation microstructure

observation (Section 3.3). **Figure 3.8 (d)** shows the ratio between the integral intensity of $\{1\ 1\ 1\}$ and $\{2\ 0\ 0\}$ peaks (I_{111}/I_{200}) in the $Co_{60}Ni_{40}$ alloy and $Co_{20}Cr_{40}Ni_{40}$ MEA as a function of the applied strain. It was found that I_{111}/I_{200} in the $Co_{60}Ni_{40}$ alloy monotonically increased with increasing the applied strain, while that in the $Co_{20}Cr_{40}Ni_{40}$ MEA saturated and slightly decreased after the strain level of about $e \sim 20$ %. The behavior suggested that the fraction of DTs in $Co_{20}Cr_{40}Ni_{40}$ MEA was larger than that in $Co_{60}Ni_{40}$ alloy, leading to the different texture development in these two alloys [168]. This was consistent with the deformation microstructure observation results. **Figure 3.8 (e)** displays the planar fault probability (P_{pf}), an indicator showing the abundance of planar faults on $\{1\ 1\ 1\}$ planes like stacking faults and DTs in FCC crystals, calculated by the CMWP as a function of the applied strain. P_{pf} monotonically increased with increasing with applied strain in both the alloys. P_{pf} of the $Co_{20}Cr_{40}Ni_{40}$ MEA increased more rapidly than that in the $Co_{60}Ni_{40}$ alloy. Just before necking ($e \sim 0.5$), the value of the $Co_{20}Cr_{40}Ni_{40}$ MEA ($P_{pf} = 0.033$) was about five times higher than that in the $Co_{60}Ni_{40}$ alloy ($P_{pf} = 0.0065$). This result was consistent with the fact that the fraction of the DTs in the $Co_{20}Cr_{40}Ni_{40}$ MEA was larger than that in the $Co_{60}Ni_{40}$ alloy. **Figure 3.8 (f)** presents the dislocation density in the $Co_{60}Ni_{40}$ alloy and $Co_{20}Cr_{40}Ni_{40}$ MEA calculated by CMWP as a function of applied strain. It was found that the dislocation density in the $Co_{20}Cr_{40}Ni_{40}$ MEA increased more rapidly than the $Co_{60}Ni_{40}$ alloy with increasing applied strain, leading to about three times higher value in the $Co_{20}Cr_{40}Ni_{40}$ MEA (7.6×10^{15} m^{-2}) compared with the $Co_{60}Ni_{40}$ alloy (2.8×10^{15} m^{-2}). This could be attributed to the accelerated dislocation multiplication in the $Co_{20}Cr_{40}Ni_{40}$ MEA owing to the formation of the stair rod immobile dislocations, as described in Section 3.4.

3.4 Discussion

3.4.1 Reasons for the difference in the microstructure evolution in $Co_{60}Ni_{40}$ alloy and $Co_{20}Cr_{40}Ni_{40}$ MEA

Even though the $Co_{60}Ni_{40}$ alloy and $Co_{20}Cr_{40}Ni_{40}$ MEA had the same materials properties except for the friction stress, these alloys exhibited different deformation microstructure evolution. Particularly, the formation of the planar structure of dislocations (type B and B-T) implied that the cross-slip of dislocations was more suppressed in the $Co_{20}Cr_{40}Ni_{40}$ MEA than the $Co_{60}Ni_{40}$ alloy. Conventionally, such differences in deformation microstructure evolution have been attributed to the difference in SFE or SRO. However, these cannot be the reasons since materials properties including SFE were unified in the alloys, and no evidence of SRO has been found in the $Co_{20}Cr_{40}Ni_{40}$ MEA. Thus, hereafter, the possible reasons for the difference in the deformation microstructure evolution in the two materials are discussed based on the difference in the friction stress, which is thought to be a key to understand the difference. As described in Section 1, the difference in the friction stress in the alloys is closely related to the heterogeneity in the atomic-scale. Thus, the atomic-scale heterogeneity could affect the deformation microstructure evolution as well as the friction stress of the alloys. There are several possible contributions as follows.

(I) Effect of atomic-scale heterogeneity on dislocation slip behavior
(I - i) Stress-induced variation of stacking fault width

In FCC crystals with low SFE, perfect dislocations are dissociated into two Shockley partial dislocations. Since these two partial dislocations have different Burgers vectors, the Schmid factors and resolved shear stress acting on leading and trailing dislocations

85

are not always identical. **Figure 3.9 (a) and (b)** present the TA orientation dependence on

the Schmid factor of leading (a / 6 [2 -1 -1] (1 1 1)) and trailing partial dislocations (a / 6

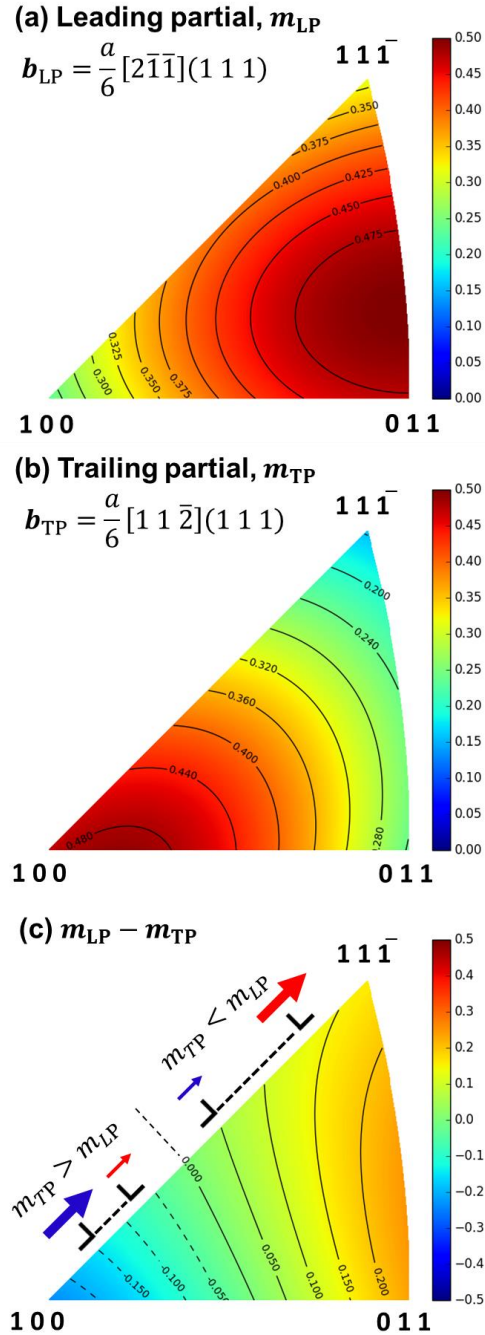[1 1 -2] (1 1 1)), respectively, dissociated from the perfect dislocations belonging to the

Figure 3.9: Schmid factor of (a) leading (m_{LP}) and (b) trailing partial dislocations (m_{TP}) belonging to the primary slip system ($b = a$ / 2 [1 0 -1] (1 1 1)) in FCC crystals depending on the grain orientation against TA. (c) Difference between (a) and (b). The scales for the color of the figures are also indicated.

primary slip system (a / 2 [1 0 -1] (1 1 1), where the perfect dislocations have the highest Schmid factor). If the Schmid factor of the leading partial (m_{LP}) is larger than that of the trailing partial (m_{TP}) (The positive part in **figure 3.9 (c)**), the width of stacking faults increases upon tensile loading due to the difference in the resolved shear stress acting on the partials. In other words, the SFE in the crystal decreases mechanically, and the cross-slip of screw dislocations becomes difficult. On the other hand, if m_{LP} is smaller than m_{TP} (The negative part in **figure 3.9 (c)**), the width of stacking faults decreases, and SFE increases upon tensile loading. Thus, the cross-slip of screw dislocations becomes easy. According to Copley and Kear [171], the effective SFE (γ_{Eff}) under a tensile stress of σ is calculated as

$$\gamma_{Eff} = \gamma_0 - \frac{m_{LP} - m_{TP}}{2} \sigma b_p, \qquad (3.5)$$

where γ_0 and b_p are SFE without loading and magnitude of Burgers vector of partial dislocations. **Figure 3.10 (a) and (b)** show the effective SFE of the $Co_{60}Ni_{40}$ alloy and $Co_{20}Cr_{40}Ni_{40}$ MEA, respectively, at yield point depending on the TA orientation. Owing to the difference in yield strength (i.e., the difference in friction stress due to the difference in the atomic-scale heterogeneity), the SFE in the $Co_{60}Ni_{40}$ alloy changed slightly, while the change in the $Co_{20}Cr_{40}Ni_{40}$ MEA was greater depending on orientation. Even after yielding where both the leading and trailing partials start moving together, the difference in the effective SFE depending on the orientation can expand owing to the difference in the velocity between the partials [171,172]. This is because the velocity of dislocations increases with increasing the resolved shear stress which is proportional to the Schmid factor. This dynamical effect can be formulated as [171]

$$\gamma_{Eff} = \gamma_0 - \frac{m_{LP} - m_{TP}}{m_{LP} + m_{TP}} \sigma b_p, \qquad (3.6)$$

Figure 3.10 (c) and (d) show the effective SFE of the $Co_{60}Ni_{40}$ alloy and $Co_{20}Cr_{40}Ni_{40}$ MEA, respectively, at the points exhibiting the maximum flow stress depending on the TA orientation. Compared with the data shown in **figure 3.10 (a) and (b)** the difference in the effective SFE distribution between the alloys expanded greatly. Owing to the higher flow stress (mainly due to the higher yield strength) in the $Co_{20}Cr_{40}Ni_{40}$ MEA, the variation of the effective SFE was much more severe than that in the $Co_{60}Ni_{40}$ alloy depending on the grain orientation. These calculation results indicate that the cross-slip
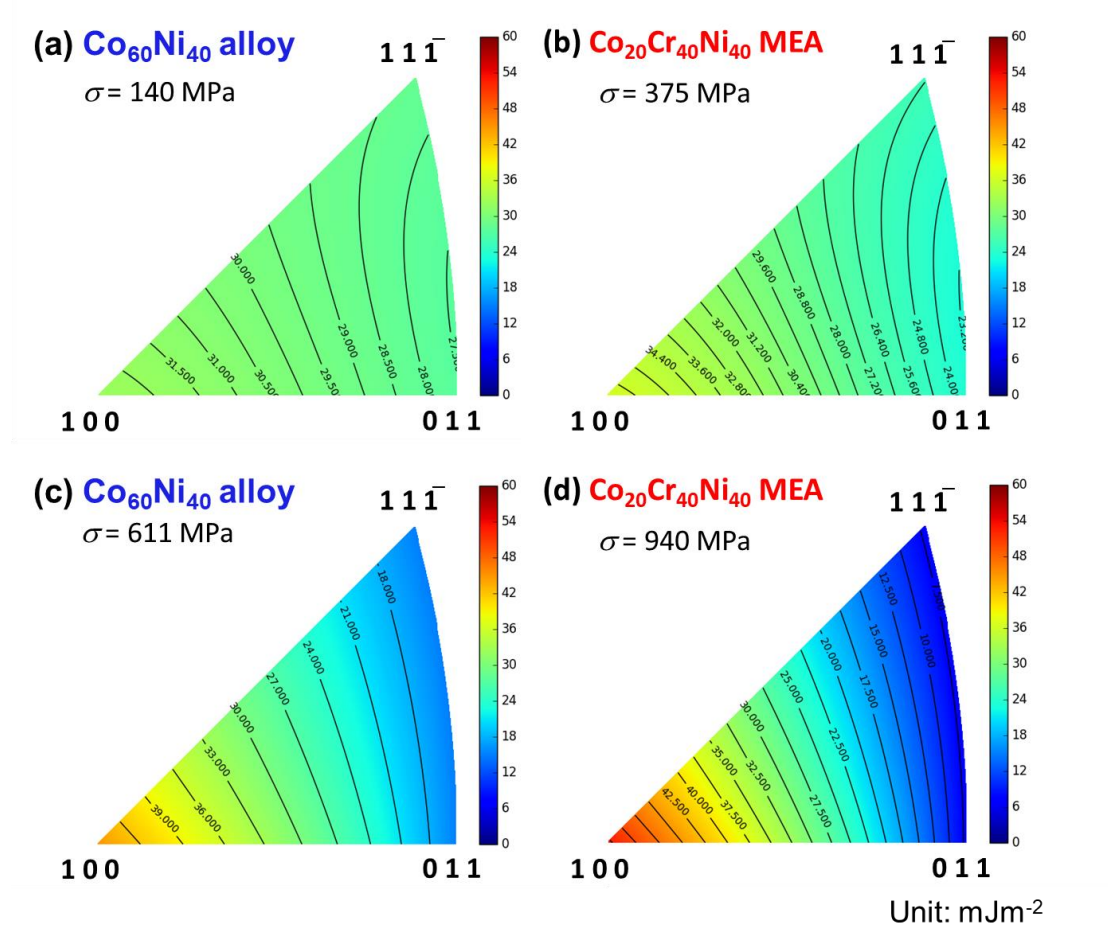

Figure 3.10: Effective SFE of (a) $Co_{60}Ni_{40}$ alloy and (b) $Co_{20}Cr_{40}Ni_{40}$ MEA at the yield point depending on the grain orientation against TA, calculated by **eq. (3.5)** based on the yield strength indicated in the figures. Effective SFE of (c) $Co_{60}Ni_{40}$ alloy and (d) $Co_{20}Cr_{40}Ni_{40}$ MEA at the maximum flow stress point depending on the grain orientation against TA, calculated by **eq. (3.6)** based on the stress levels (true stress) indicated in the figures, considering the dynamical effect. The scales for the color of the figures are also indicated.

of dislocations is promoted and inhibited in the TA ~// <1 0 0> oriented grains and others, respectively, leading to the type A and B microstructure observed in the $Co_{20}Cr_{40}Ni_{40}$ MEA. This can fully explain the orientation dependence of the deformation microstructure like type A and B microstructure observed in the $Co_{20}Cr_{40}Ni_{40}$ MEA and other high-alloy systems reported to date [115,116,127–135,117–124].

(I - ii) Chemical heterogeneity-induced variation of stacking fault width

Smith *et al.* [61] observed the core structure of dislocations in CoCrFeMnNi HEA by using STEM and found that the width of the stacking faults varied significantly compared with conventional FCC dilute alloys and pure metals. They also employed atomistic simulation and showed that, with increasing the number and concentration of alloying elements, the stacking faults became a wavy shape having various widths depending on the local chemical environment around each segment. Rao *et al.* [173] also reported the same behavior in $Co_{30}Fe_{16.67}Ni_{36.67}Ti_{16.67}$ alloy with FCC structure by using molecular dynamics simulation. Their results suggested that the variation of stacking fault width could be prominent at room temperature as well as low temperature, and the cross-slip of dislocations preferentially started from the parts having a smaller width. According to their description, only small segments of screw dislocations proceeded cross-slip due to the low applied stress. These results imply that the cross-slip of screw dislocations can be easy at the position with small stacking fault width, while the cross-slip can be restricted by the parts having larger width at the same time. Therefore, complete cross-slip of screw dislocations may be difficult in high-alloy systems like the $Co_{20}Cr_{40}Ni_{40}$ MEA.

To correlate the above idea with the orientation dependence of deformation microstructure evolution in the $Co_{20}Cr_{40}Ni_{40}$ MEA, now, it is considered that one screw

dislocation lying on the primary plane change its slip plane by cross-slip. **Figure 3.11 (a)** shows the TA orientation dependence of the Schmid factor ratio between the primary and cross-slip systems. The stereo triangle can be divided by 2 1 -1 – 0 1 1 boundary into two.
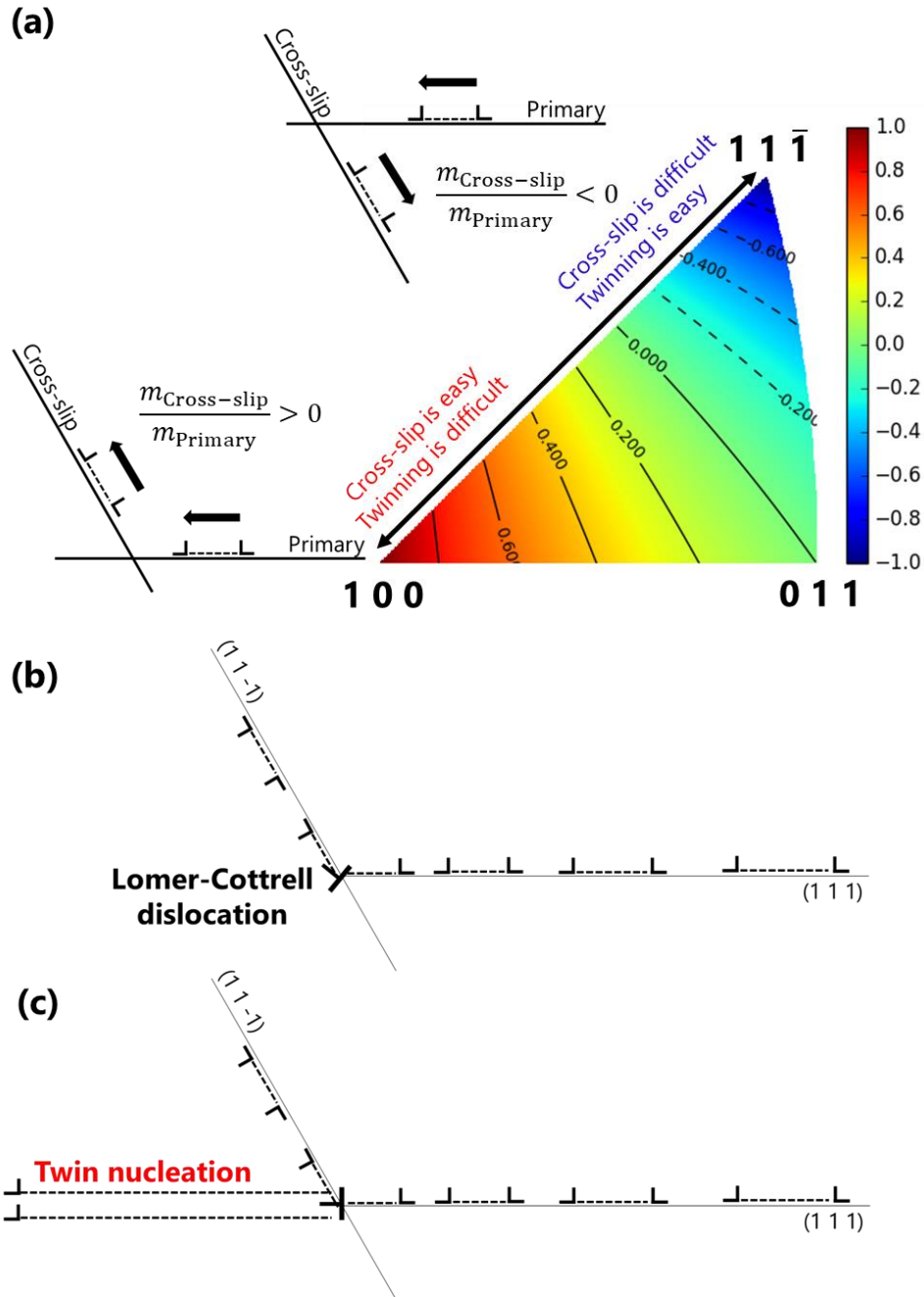

Figure 3.11: The ratio between the Schmid factors in the primary ($m_{Primary}$) and cross-slip systems ($m_{Cross-slip}$) depending on the grain orientation against TA. Schematic illustrations showing (b) the formation of a Lomer-Cottrell dislocation at the intersection of two slip planes and (c) the nucleation of a DT along the primary plane, according to the MTN model.

In the grains having the positive Schmid factor ratio, cross-slip favorably happens with obtuse angles, while, in those with the negative Schmid factor ratio, cross-slip favorably happens with acute angles. Since such cross-slip with acute angles is energetically and mechanically unfavorable, cross-slip tends to be difficult in the grains oriented to TA ~// <1 1 1> and easy in those oriented to TA ~// <1 0 0>. If cross-slip is suppressed by the variation of stacking fault width in the material, the region where cross-slip is difficult in **Figure 3.11 (a)** may expand toward <1 0 0>. This can also explain the orientation dependence of the deformation microstructure evolution in the $Co_{20}Cr_{40}Ni_{40}$ MEA.

(I-iii) Element-element interaction (Solute-Solute interaction)

As proposed in the previous study [138], the element-element interaction, chemical interaction among alloying elements (this has been termed as "solute-solute interaction" in conventional dilute systems), can play an important role in high-alloy systems. When dislocations glide along the slip plane, there should be changes in the bonding combination of elements at the core of dislocations by shifting one atomic plane along the Burgers vector. Such local rearrangement of elements requires extra-energy for dislocation motion in addition to the effect of atomic size misfit. This effect has been semi-quantitatively modeled by Nag *et al*. [106] recently. The theoretical studies by Nöhring and Curtin [103,104] showed such solute-solute (element-element) interaction can increase the activation energy for the cross-slip of screw dislocations in FCC solid solutions. A similar idea has been also proposed by Hong and Laird [174,175]. Thus, the element-element interaction may also contribute to the suppression of the cross-slip of screw dislocations in high-alloy systems. This mechanism can also expand the region where cross-slip is difficult in **Figure 3.11 (a)** toward <1 0 0>. Thus, the orientation

dependence of the deformation microstructure evolution in the $Co_{20}Cr_{40}Ni_{40}$ MEA can be also explained in the same manner as (I-ii).

(II) Effect of atomic-scale heterogeneity on twinning behavior

In this study, it was also found that DTs were likely to be formed in the grains oriented to TA ~// <1 1 1>, and the fraction of DTs in the $Co_{20}Cr_{40}Ni_{40}$ MEA was higher than the $Co_{60}Ni_{40}$ alloy. Considering the fact that the DTs were formed along the primary plane, among the various twinning models in FCC crystals [136,176,177], Miura-Takamura-Narita (MTN) model [178,179] could explain the twinning behavior as follows. Now, it is assumed that there are two slip systems (one is the primary slip system) intersecting with each other and a Lomer-Cottrell immobile dislocation is formed (**Figure 11 (b)**). Since such immobile dislocations can be obstacles for dislocation motion, dislocations tend to pile-up against the immobile dislocations, and stress concentration happens at the tip. In principle, there are two ways to relax high stress at the tip. One way is the cross-slip of dislocations. The other way is to generate DTs along the primary plane. As explained in (I-ii), cross-slip is unfavorable in the grains oriented to TA ~// <1 1 1>, and DTs nucleate along the primary plane to relax the high stress, instead [179]. This could be why DTs were observed in the grains oriented to TA ~// <1 1 1> in the $Co_{60}Ni_{40}$ alloy, $Co_{20}Cr_{40}Ni_{40}$ MEA, and other FCC metals [180]. It should be noted that this mechanism can explain the twin nucleation at grain boundaries in a consistent manner, as reported by Hong *et al*. [177]. Most importantly, in the cases of high-alloy systems like $Co_{20}Cr_{40}Ni_{40}$ MEA, cross-slip is suppressed due to the reasons discussed above (I-i, ii, and iii). Accordingly, cross-slip in the grains oriented to TA ~// <1 1 1> can be much more difficult in high-alloy systems than conventional dilute systems; Thus, DTs progressively

nucleated in the $Co_{20}Cr_{40}Ni_{40}$ MEA more than the $Co_{60}Ni_{40}$ alloy.

3.4.2. Characteristics of deformation mechanisms in FCC high-alloy systems

As explained in the previous section, the cross-slip of screw dislocations in the $Co_{20}Cr_{40}Ni_{40}$ MEA is more suppressed than the $Co_{60}Ni_{40}$ alloy, resulting in the formation of PDS, fine DCs, and DTs depending on the grain orientation. Compared with the $Co_{60}Ni_{40}$ alloy exhibiting mainly coarse DCs, the characteristic deformation microstructure evolution in the $Co_{20}Cr_{40}Ni_{40}$ MEA is advantageous in terms of achieving superior mechanical properties as follows.

(I) Internal stress development

Since the cross-slip of screw dislocations is suppressed in the $Co_{20}Cr_{40}Ni_{40}$ MEA, dislocations tend to pile-up against obstacles such as grain boundaries and immobile dislocations. It is well-known that the pile-up of dislocations causes stress concentration at the tip, and the internal stress in the grain increases [166]. Thus, the flow stress and work-hardenability of the $Co_{20}Cr_{40}Ni_{40}$ MEA could be enhanced compared with the $Co_{60}Ni_{40}$ alloy.

(II) Dislocation density evolution

As observed by using ET (Section 3.4), the stair rod immobile dislocations can be easily formed in the $Co_{20}Cr_{40}Ni_{40}$ MEA due to the suppressed cross-slip. The formation of immobile dislocations generally promotes dislocation multiplication as dislocations cut each other, making new dislocation sources [165]. In addition, since cross-slip is suppressed in the $Co_{20}Cr_{40}Ni_{40}$ MEA, dynamic recovery during deformation should be

inhibited. Thus, as confirmed by using in-situ XRD during tensile deformation, dislocation density in the $Co_{20}Cr_{40}Ni_{40}$ MEA became higher than that in the $Co_{60}Ni_{40}$ alloy, resulting in enhanced work-hardenability.

(III) Grain refinement by deformation twins

In FCC metals, shear deformation introduced by DTs is very small compared with other crystal structure materials like HCP metals [176]. Instead, twin boundaries act as obstacles for dislocation motion, similar to the effect of ordinary grain boundaries [66], and better work-hardenability can be obtained. This is the so-called dynamic Hall-Petch effect [136]. As shown in **figure 3.4 and 3.5**, the fraction of DTs in the $Co_{20}Cr_{40}Ni_{40}$ MEA was much higher than that in the $Co_{60}Ni_{40}$ alloy due to the suppressed cross-slip. Therefore, the formation of DTs with high-density also contributed to better work-hardenability in the $Co_{20}Cr_{40}Ni_{40}$ MEA.

3.5. Conclusion

In the present study, the mechanical properties of the $Co_{60}Ni_{40}$ alloy (with low friction stress) and $Co_{20}Cr_{40}Ni_{40}$ MEA (with high friction stress) with the same materials properties such as SFE and elastic constants were compared and deformation microstructure evolution during tensile deformation was investigated by using TEM with multi-dimensions and in-situ XRD. The key results are the following:

(1) Tensile tests were performed at room temperature. The $Co_{20}Cr_{40}Ni_{40}$ MEA was found to show higher yield strength and work-hardening rate than the $Co_{60}Ni_{40}$ alloy resulting in the superior strength-ductility balance.

(2) In the $Co_{60}Ni_{40}$ alloy, most of the grains developed coarse DCs regardless of grain

orientation. A few grains oriented to TA ~// <1 1 1> showed a small fraction of DTs.

(3) In the $Co_{20}Cr_{40}Ni_{40}$ MEA, fine DCs were observed in the grains oriented to TA ~// <1 0 0>, while PDS were observed in others. Many DTs were formed in the grains oriented to TA ~// <1 1 1>.

(4) The three-dimensional structure of the PDS in the $Co_{20}Cr_{40}Ni_{40}$ MEA at the initial stage of deformation was resolved by ET. Many of the dislocations were confined in specific {1 1 1} planes. Dislocations belonging to two different slip systems were found to be intersecting with each other, leaving the stair rod immobile dislocations.

(5) In-situ XRD measurement during tensile deformation revealed a different tendency in the internal stress and texture development in the $Co_{60}Ni_{40}$ alloy and $Co_{20}Cr_{40}Ni_{40}$ MEA, suggesting that heterogeneous deformation microstructure evolution in the $Co_{20}Cr_{40}Ni_{40}$ MEA. The increment of both planar fault probability and dislocation density during deformation was much larger in the $Co_{20}Cr_{40}Ni_{40}$ MEA than the $Co_{60}Ni_{40}$ alloy.

In brief, this study implied that the cross-slip of screw dislocations and dynamic recovery in FCC high-alloy systems (e.g., HEAs, MEAs, and austenitic steels) is inhibited, leading to the characteristic deformation microstructure evolution and enhanced work-hardening. This means that FCC high-alloy systems inherently exhibit superior mechanical properties because of alloying effect (not just simply because SFE decreases). Therefore, the findings of the present study will make it possible to open a path to new fundamental design principles of structural materials for overcoming the dilemma of

strength-ductility trade-off in conventional metallic materials.

Chapter 4: Recrystallization behavior: Approaching the limit

of grain-refinement by recrystallization

4.1. Introduction

Heavily-deformed crystalline materials store high elastic energy due to accumulated non-equilibrium crystal defects introduced by deformation. If they are subsequently annealed at high temperature, restoration of microstructure starts by nucleation and growth of grains with very low defect density, so-called "*recrystallization*". For centuries, recrystallization has been one of the most important and fundamental phenomena in physical metallurgy and geology. Recrystallization also plays an essential role in the industrial processing of metallic materials since their properties can be finely-tuned through controlling microstructure. In the past several decades, the mechanism of recrystallization in pure metals and dilute alloys has been extensively studied [68].

On the other hand, HEAs and MEAs aroused the curiosity of many material scientists owing to their intriguing mechanical properties [6,7]. In the early days, HEAs and MEAs with as-cast and/or as-homogenized states had been mainly studied [8]. Afterward, many people started investigating microstructure evolution during thermo-mechanical processes (involving recrystallization) in HEAs and MEAs [42,138,181–185] because of their potential application in industry as well as fundamental scientific importance. For example, Sun *et al*. [181] reported the fabrication of fully-recrystallized ultrafine-grained (FRex-UFG) microstructure in CoCrFeMnNi HEA with FCC single-phase through simple cold-rolling and recrystallization. In Chapter 2, it was also revealed that FRex-UFG microstructure can be easily achieved in various FCC MEAs through SPD process [186] and recrystallization. Some of these materials were found to exhibit exceptional mechanical properties compared with other conventional metals and alloys having FCC single-phase. In both studies, there seemed to be more room to explore microstructure with finer grain sizes by further optimizing the processing condition. Also, these results

raise one fundamental question: Why is it possible to easily obtain FRex-UFG microstructure in FCC HEAs and MEAs through simple deformation and annealing processes?

In the present study, high-pressure torsion (HPT) [187], one of the SPD process, was applied to CoCrFeMnNi HEA and CoCrNi MEA, and their recrystallization behavior during subsequent annealing at high temperature was investigated. By employing both experiments and atomistic simulations, this study aimed at clarifying the special characteristics of the recrystallization in HEAs and MEAs. Additionally, FRex-UFG microstructure having FCC single-phase with the smallest mean grain size ever reported to date was achieved. It is anticipated that the knowledge presented here will be helpful to construct a universal theory applicable to metals and alloys regardless of the concentration of alloying elements.

4.2. Materials and methods

4.2.1. Materials

Ingots of equiatomic CoCrFeMnNi HEA and CoCrNi MEA having button shapes were produced by vacuum arc-melting of constituent elements with a purity higher than 99.9 wt. % in a water-cooled copper mold under an inert Ar atmosphere. The buttons were flipped and re-melted at least five times to achieve better compositional homogeneity.

The ingots were also subsequently cold-rolled by 90% reduction in thickness and homogenized (fully-recrystallized) at 1200 $^{\circ}$C for 24 h under a vacuum environment ($\sim$ 10^{-4} Pa) using a vacuum tube furnace to remove macro-segregations in the alloys.

Afterward, water-quenching was performed. The resulting grain size in the HEA and MEA were approximately 50 μm.

4.2.2. Deformation and annealing

Disc-shaped specimens with a diameter of 10 mm and a thickness of 0.8 mm for HPT were prepared by cutting the homogenized materials. The HPT process was performed at room temperature under a pressure of 6 GPa at a speed of 0.2 rpm (rotation per minute). The total rotation angle applied was 1800° (five rotations).

After the heavy deformation by HPT, specimens of CoCrFeMnNi HEA and CoCrNi MEA were annealed at 800 °C for 10 s and 700 °C for 30 s, respectively, followed by water-quenching to obtain fully-recrystallized ultrafine-grained microstructure. To investigate the grain growth behavior, the HEA and MEA were also annealed at 800 – 950 °C and 700 – 1100 °C, respectively, for various holding times followed by water-quenching.

4.2.3. Microhardness measurement

Vickers microhardness measurements were conducted on a Vickers microhardness tester (SHIMADZU, HMW-2) at a load of 4.903 N and dwell of 10 seconds. All the measurements were performed at room temperature. The disc specimens of CoCrFeMnNi HEA and CoCrNi MEA were processed by HPT with a different number of rotations under the same condition described in the method section in the manuscript. The microhardness measurements were done on the disc plane of the specimens along the radial direction with an interval of 0.5 mm. The radial position of the measured points was converted to shear strain based on **eq. (2.1)**.

4.2.4. Microstructural observations

Specimens for microstructural observation were cut from the cross-section normal to the radial direction and 3 mm away from the center in the HPT discs.

For SEM observation, the specimens were mechanically polished by using 1000 - 4000 grid sized fine sandpapers and then diamond pastes (1 - 3 μm) to achieve mirror-like surfaces. Afterward, the specimens were electrically polished in a solution of 90 vol. % Ethanol and 10 vol. % Perchloric acid at 30 V for 15 s at room temperature. The microstructure was then characterized by using an SEM (JEOL, JSM-7100 / 7800F) equipped with BSE. Grain sizes of the specimens were determined by the line intercept method on SEM-BSE images. EBSD measurements in CoCrFeMnNi HEA and CoCrNi MEA after primary recrystallization completed were performed by using an SEM (JEOL, JSM-7100 / 7800F) equipped with EBSD detectors. The data collection of EBSD was conducted using TSL-OIM data collection software (TSL solutions, ver. 5.31), and the OIM analysis software (Tex SEM Laboratories, ver. 7.3) was used to analyze the collected data.

For TEM observation, thin slices were cut out, and the slices were furthermore mechanically polished to reduce the thickness to about 50 μm and achieve a mirror-like surface. Then, the specimens were electrically polished in an electrolyte composed of 70 vol.% Methanol, 20 vol.% Glycerin, and 10 vol.% Perchloric acid at 243 K at 15 V by using a twin-jet polishing machine (Tenupol-5, Struers). TEM observations were performed in JEM-2100F (JEOL) at an operation voltage of 200 kV at room temperature.

4.2.5. Synchrotron X-ray diffraction measurement

To investigate the crystal structure of the HEA and MEA after deformation and after primary recrystallization completed, XRD measurements were performed at room temperature ($T = 25$ °C) in a synchrotron radiation facility, beamline No. 46XU in SPring-8 in Hyogo, Japan. The energy of the incident X-ray beam was set to be 30 keV by using an automated double-mirror monochromator, and the spot size of the beam was 0.3 mm (in length) $\times$ 0.5 mm (in width). The specimens for the XRD measurement were mechanically polished by 1000 - 4000 grid sized fine sandpapers and then 1 - 3 μm diamond pastes to achieve mirror-like surfaces. Each specimen was set on a computer-controlled four-axis goniometer so that the position of the specimen was adjusted exactly as same as the designated camera length of the system, and the surface was perfectly parallel to the incident X-ray beam. The transmission-diffracted X-ray beam was detected by a one-dimensional semiconductor detector (MYTHEN, Dectris). The data acquisition time (exposure time) was set to be 60 s to achieve a better signal-noise ratio. The calibration of the system was done using a standard CeO_2 sample. To estimate the dislocation density of the deformed materials, the CMWP method [154] was employed. In the model, XRD profiles are fitted by a theoretical model that takes the effect of dislocation density, crystallite size, elastic anisotropy, and planar faults into account. Since, in high-alloy systems like HEAs and MEAs, chemical heterogeneity can also contribute to the peak broadening (resulting in an overestimation of dislocation density), the profiles of the recrystallized HEA and MEA were used as standards to eliminate the chemical heterogeneity effect from the results, as proposed in the previous study[155].

4.2.6. Tensile tests

Tensile tests were performed on a universal tensile test machine (SHIMADZU, AG-100 kN Xplus) at room temperature at a quasi-static strain rate of 8.3×10^{-4} s^{-1} for characterizing the mechanical properties of the alloys. Small-sized tensile specimens with a gauge length of 2 mm and a gauge cross-section of 1×0.5 mm were cut from the annealed specimens having FCC single-phase so that the center of the gauge part coincided with the position at a radial distance of 3.0 mm from the center of the disc samples. It was confirmed in the previous study that the small-sized specimens could give reliable stress-strain behaviors equivalent to those obtained from standard size specimens of the same materials [42]. Due to the difficulty in attaching the extensometer or strain gauge on the small-sized specimens, the displacement of the gauge section was precisely measured by a CCD video camera extensometer (SVS625MFCP), and the strain was calculated by the use of the DIC technique. Surfaces of all the tensile specimens were painted with white and black inks to produce a random dot pattern (speckle pattern) acting as markers easily tracked during deformation for the DIC analysis. In-situ DIC measurements were achieved from a set of strain snapshots collected automatically by using Vic-2D software [49].

4.2.7. Atomistic simulation of grain boundaries

To investigate the effect of atomic size difference on the GB structure in HEAs, hybrid Monte Carlo/Molecular dynamics (MC/MD) simulations in two-dimensional crystal lattices composed of five elements having variable atomic size differences were performed.

To express the interatomic interactions between the element α and β, the shifted force potentials ($\phi_s^{\alpha\beta}$) was used, in which interatomic interaction energy and its gradient became zero at the cutoff distance of r_c as follows:

$$\phi_s^{\alpha\beta}(r) = \begin{cases} \phi^{\alpha\beta}(r) - \phi^{\alpha\beta}(r_c) - (r - r_c)\frac{d\phi^{\alpha\beta}(r_c)}{dr} & (r \leq r_c) \\ 0 & (r \geq r_c) \end{cases}, \tag{4.1}$$

where r was the interatomic distance between two elements. $\phi^{\alpha\beta}$ was the Morse potential expressed as

$$\phi^{\alpha\beta}(r) = D^{\alpha\beta}\left\{e^{-2a^{\alpha\beta}\left(r-r_0^{\alpha\beta}\right)} - 2e^{-a^{\alpha\beta}\left(r-r_0^{\alpha\beta}\right)}\right\}, \tag{4.2}$$

where $D^{\alpha\beta}$, $a^{\alpha\beta}$, and $r_0^{\alpha\beta}$, were the materials constant related to cohesive energy, elastic constants, and lattice constant, respectively. For simplicity, $D^{\alpha\beta}$ and $a^{\alpha\beta}$ were fixed as 8.16×10^{-20} J and 14.57 nm^{-1}, respectively, in all the elemental combinations. In order to simulate quinary HEAs having various atomic size difference, $r_0^{\alpha\beta}$ was designed as

$$r_0^{\alpha\beta} = r_0^{33} + \frac{1}{2}k\xi(\alpha + \beta - 6) \ (\alpha, \beta = 1, 2, ..., 5) \tag{4.3}$$

where r_0^{33} and ξ were 0.4657 nm and 0.067 nm, respectively. Four types of HEAs having different atomic size differences were simulated by putting $k = 0, 1, 2, 3$. r_c in **eq. (4.1)** was set as 2.2 r_0^{55} in this study.

The atomic size differences in the quinary HEAs were quantified based on the following definition

$$\delta = \sqrt{\sum_{i=1}^{n} c_i \left(1 - \frac{r^{ii}}{\sum_{j=1}^{n} c_j r^{jj}}\right)^2} \times 100 \ (i = 1, 2, ..., 5) \tag{4.4}$$

where n and c_i are the numbers of alloying elements and the concentration of each element in the HEAs. r^{ii} is the radius of element i in a perfect crystal relaxed by the method

described later and closely related $r_0^{ii} = r_0^{33} + k\xi(i-3)$. The δ of the simulated HEAs were 0, 2.06, 4.12, and 6.15.

Bicrystal models, in which one circular-shaped grain was embedded in a matrix, were created to simulate the GB structure in the HEAs with different δ. The embedded grain was rotated by 30 degrees against the matrix. Five elements (approximately 500 atoms for each element) were randomly positioned in a triangular lattice. Periodic boundary condition and constant stress condition was applied in all the structures.

Thermodynamic equilibrium states of atomic configuration at finite temperatures, T, were calculated by the hybrid MC/MD method. In this method, GB structures were relaxed by using MD for 100 ps at $T = 300$ ($\sim 0.1\ T_m$), 1000 ($\sim 0.4\ T_m$), and 2000 ($\sim 0.8\ T_m$) K, first. Here, T_m (~ 2500 K) is the average melting point of all the models with different δ values. It should be noted that the temperature of the systems was controlled by the velocity scaling method. Afterward, the positions of two randomly-chosen atoms were exchanged, and GB structures were relaxed for 10 ps again by using MD. Then, the total potential energy change (ΔE) of the system before and after the exchange was calculated. If $\Delta E \leq 0$, the exchange of atoms was accepted. If $\Delta E > 0$, the exchange was accepted according to the probability of exp($-\Delta E\ /\ k_B T$), where k_B is the Boltzmann constant. In each structure, the exchange of atoms was conducted 7320 times.

In each HEA model, the volume of each atom was determined by the Voronoi division method. The average free volumes at GB with different GB misorientations (0 – 60°) were quantified by the following equation.

$$V_{GB} = \frac{1}{A_{GB}}(V_{Cell} - N_{Cell}\overline{V_{Atom}}), \qquad (4.5)$$

where A_{GB} was the total area of GBs. V_{Cell} and $\overline{V_{Atom}}$ are total volumes of the simulated unit cell including GBs and average atomic volume of a perfect lattice, respectively. N_{Cell} is the total number of atoms in the simulated unit cell including GBs. It should be noted that V_{GB} has a dimension of length. In order to appropriately compare the results obtained under different conditions, the V_{GB} values were firstly normalized by the magnitude of Burgers vector (b) to eliminate the effect of system size (i.e., V_{GB} / b), and then, normalized by the value of pure metal with $\delta = 0$ (i.e., $\frac{V_{GB}/b}{V_{GB}^{\delta=0}/b^{\delta=0}}$).

4.3. Results

4.3.1. Deformation microstructure after high-pressure torsion

The deformation microstructure of CoCrFeMnNi HEA and CoCrNi MEA was investigated, first because it is correlated to recrystallization (as discussed later). Both the materials having FCC single-phase were processed by HPT at room temperature. **Figure**
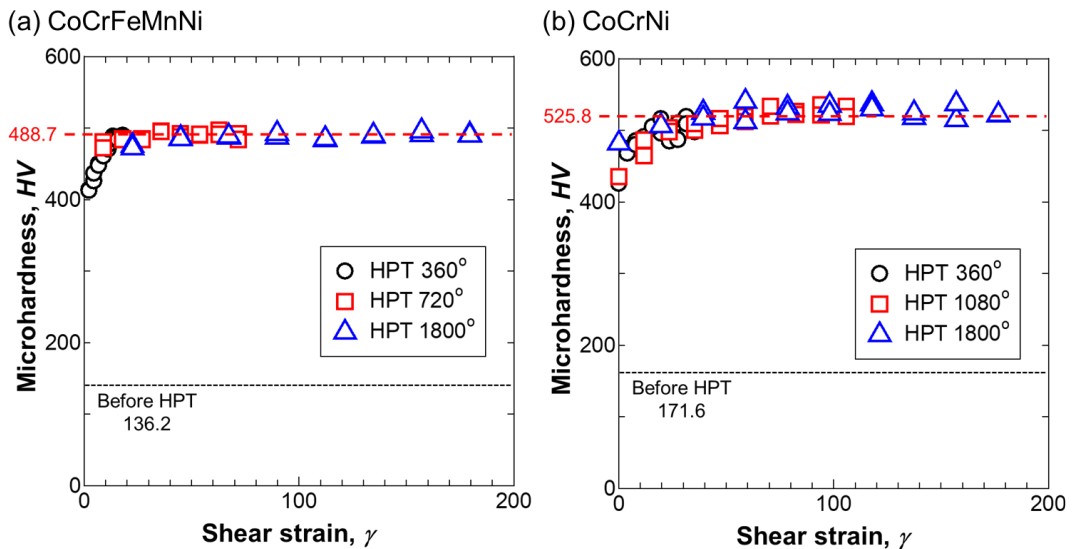

Figure 4.1: Microhardness as a function of applied shear strain during HPT in (a) CoCrFeMnNi HEA and (b) CoCrNi MEA. The microhardness before HPT is indicated by dashed lines. The microhardness after the values saturated is also indicated in the figures.

4.1 (a) and (b) present the microhardness as a function of shear strain in CoCrFeMnNi HEA and CoCrNi MEA, respectively. In CoCrFeMnNi HEA, the microhardness increased from HV 136.2 to HV 488.7 and then saturated after a shear strain of about 15 was applied. On the other hand, in CoCrNi MEA, the microhardness increased from HV 171.6 to HV 525.8 and then saturated after a shear strain of about 20. The saturation of microhardness implied that microstructural change is also saturated due to balancing between the introduction of defects and dynamic recovery during HPT [188].

Figure 4.2 (a) and 4.3 (a) show BF-TEM micrographs of CoCrFeMnNi HEA and CoCrNi MEA, respectively, processed by HPT. DF-TEM images (**Figure 4.2 (c), (d), figure 4.3 (c), and (d)**) were formed by the diffraction spots (P1 and P2) shown in the
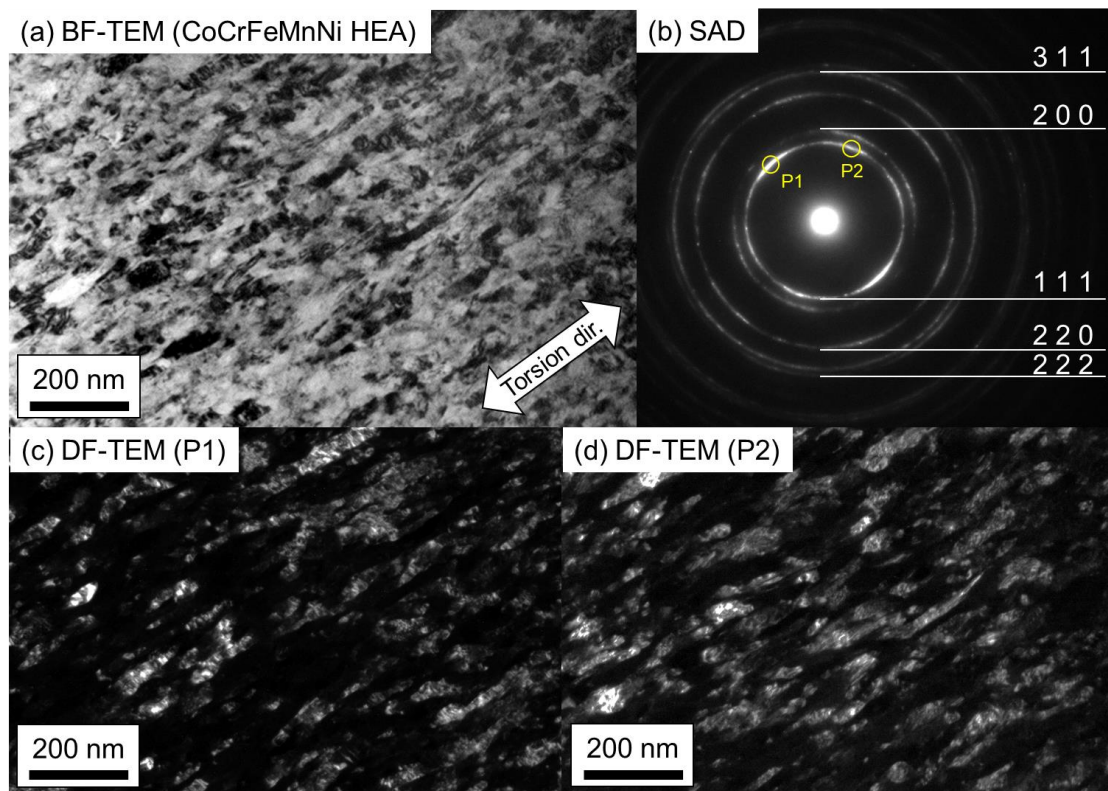

Figure 4.2: (a) BF-TEM micrograph of CoCrFeMnNi HEA processed by HPT. The torsion direction is indicated in the figure. (b) SAD pattern taken from the same area shown in (a). The indexes of each ring corresponding to FCC structure are indicated in the figures. DF-TEM images formed by the diffraction spots of (c) P1 and (d) P2 in (b) taken in the same area as shown in (a).

selective area diffraction (SAD) pattern presented in **figure 4.2 (b) and 4.3 (b)**, respectively. These DF-TEM micrographs were taken in the same area as shown in **figure 4.2 (a) and 4.3 (a)**, respectively. Nanocrystalline microstructures composed of elongated
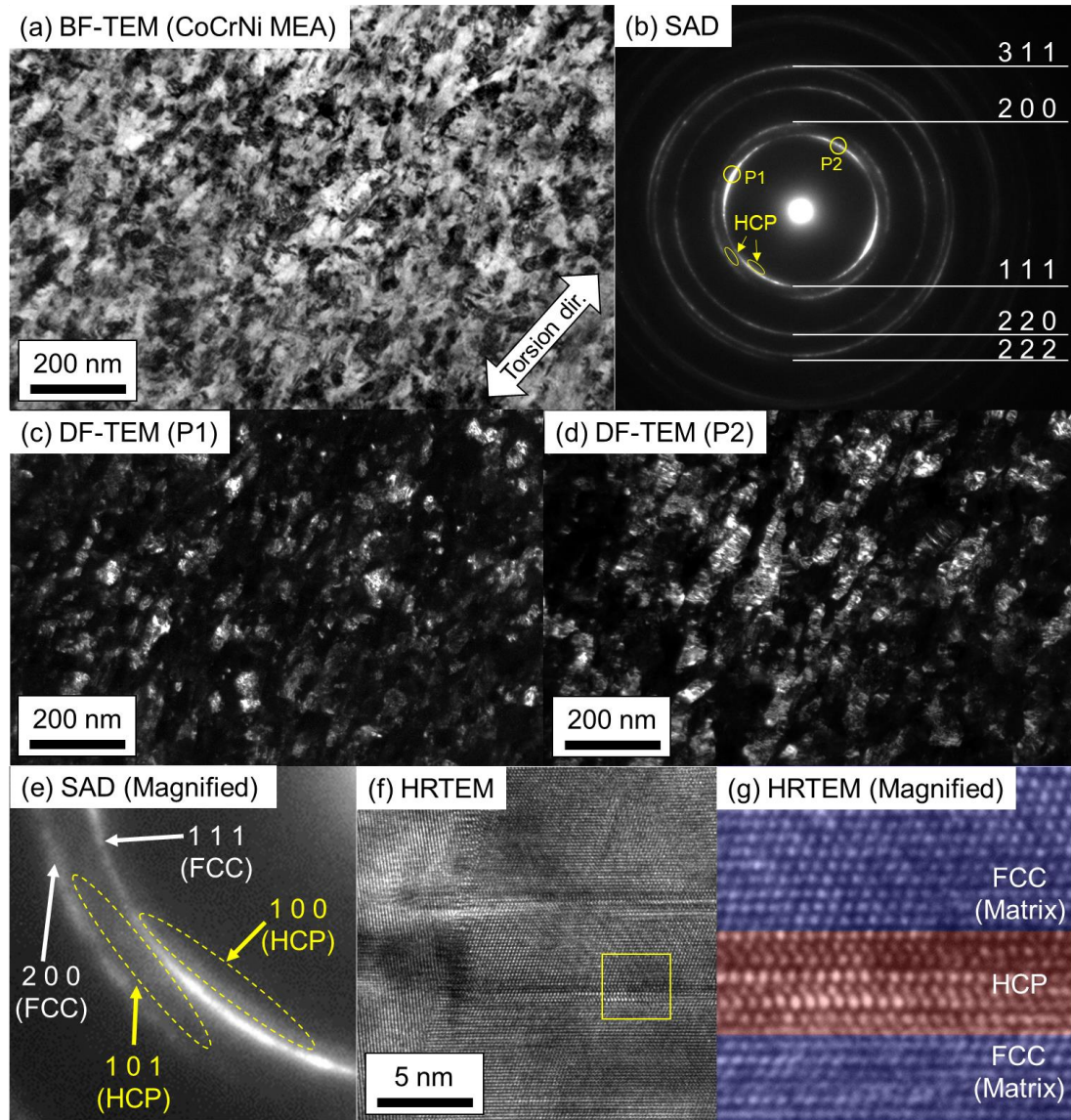

Figure 4.3: (a) BF-TEM micrograph of CoCrNi MEA processed by HPT. The torsion direction is indicated in the figure. (b) SAD pattern taken from the same area shown in (a). The indexes of each ring corresponding to FCC structure are indicated in the figures. DF-TEM images formed by the diffraction spots of (c) P1 and (d) P2 in (b) taken in the same area as shown in (a). (e) Magnified image of (b). The parts indicated by white and yellow allows correspond to the reflection of FCC and HCP structure, respectively. (f) HRTEM micrograph of CoCrNi MEA processed by HPT. (g) Magnified image corresponding to the area indicated by a yellow rectangle in (f). Lattice structures corresponding to FCC and HCP structure are colored by blue and red, respectively.

(along torsion direction) and fragmented grains with a size of 58 nm and 43 nm were observed in the CoCrFeMnNi HEA and CoCrNi MEA, respectively. Interestingly, these grain sizes were much finer than other pure FCC metals and dilute alloys processed under similar conditions [189]. Based on the corresponding SAD patterns (**Figure 4.2 (b) and 4.3 (b)**) showing ring patterns, these grains were expected to be mostly surrounded by high-angle grain boundaries (HAGBs). Fragmented grains elongated along the torsion direction could be seen. The grains contained high-density lattice defects. The SAD pattern of the CoCrFeMnNi HEA (**Figure 4.2 (b)**) consisted of only FCC single-phase. In contrast, the magnified SAD pattern shown in **figure 4.3 (e)** suggested the presence of HCP phase in the CoCrNi MEA. In **figure 4.3 (f)**, a high-resolution (HR) TEM micrograph of the MEA is presented. Planar defects were confirmed in the microstructure. The magnified image of **figure 4.3 (f)** clearly revealed the presence of HCP phase with a thickness of 8 atomic layers (**Figure 4.3 (g)**). Similar structures have been reported in the same MEA tensile-deformed at room temperature and cryogenic temperature[35], and it has been considered as deformation-induced martensite having plate-shape morphology.

The CMWP method [154] was employed to extract the dislocation density of the HPT-processed materials from the one-dimensional synchrotron XRD profiles. **Figure 4.4 (a) and (b)** present XRD profiles of CoCrFeMnNi HEA and CoCrNi MEA, respectively, after HPT. The HEA showed only the peaks corresponding to FCC structure, while, in the MEA, (1 0 0) peak of HCP structure was observed as well as the peaks of FCC structure. These were consistent with the SAD patterns explained above. The
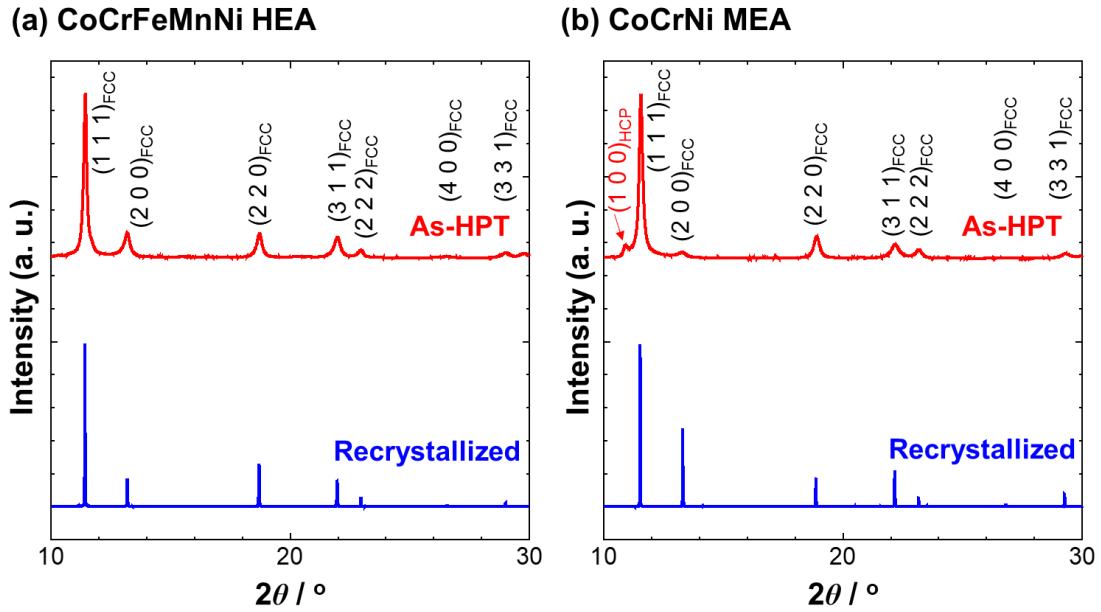
Figure 4.4: XRD profiles of (a) CoCrFeMnNi HEA and (b) CoCrNi MEA after HPT and after recrystallization at 800 °C for 10 s and 700 °C for 30 s, respectively. The peaks are indexed by corresponding lattice planes in FCC structure. The peak indicated by a red arrow corresponds to (1 0 0) plane in HCP structure.

dislocation density of the HPT-processed HEA and MEA were estimated as 3.4×10^{16} and 5.4×10^{16} m^{-2}, respectively, which are consistent with the previous literature [190]. It should be noted that if the dislocation density of metals reaches $10^{17} - 10^{18}$ m^{-2}, amorphization happens, as reported in the Ni-Ti system [191]. Therefore, the obtained dislocation densities in the HEA and MEA were considered to be close to their upper limit for maintaining the crystalline structure. These results implied that severe grain subdivision happened in the materials since dynamic recovery was inhibited due to the low stacking fault energy (SFE) (CoCrFeMnNi: 30 mJm^{-2} [192], CoCrNi MEA: 20 mJm^{-2} [34]). In addition, some of the recent studies showed that the width of stacking faults in FCC HEAs and MEAs varied significantly due to the chemical heterogeneity on an atomic-scale [61,173], and the parts having the widest stacking fault width can control the process of dynamic recovery. Therefore, inhibited dynamic recovery is characterized as one of the special characteristics of FCC HEAs and MEAs.

4.3.2. Microstructure after primary recrystallization completed

The HEA and MEA were subsequently annealed at 800 ℃ for 10 s and 700 ℃ for 30 s, respectively, to obtain FRex-UFG microstructure. **Figure 4.5** presents an SEM-BSE micrograph of CoCrNi MEA processed by HPT and subsequently annealed at 700 ℃ for 10 s. It was partially recrystallized, and there were nucleated recrystallized grains having annealing twins distributed. The size of the recrystallized grains was about 100-200 nm (without annealing twins) in diameter. Partially-recrystallized microstructure could not be observed in CoCrFeMnNi HEA because it was necessary to anneal the specimens at above 800 ℃, where recrystallization kinetics is very fast, to avoid sigma phase precipitation [193].

In **figure 4.4 (a) and (b)**, the XRD profiles of CoCrFeMnNi HEA and CoCrNi MEA, respectively, after primary recrystallization completed after annealing at 800 ℃ for 10 s and 700 ℃ for 30 s, respectively, were presented. Compared with the profiles of the as-
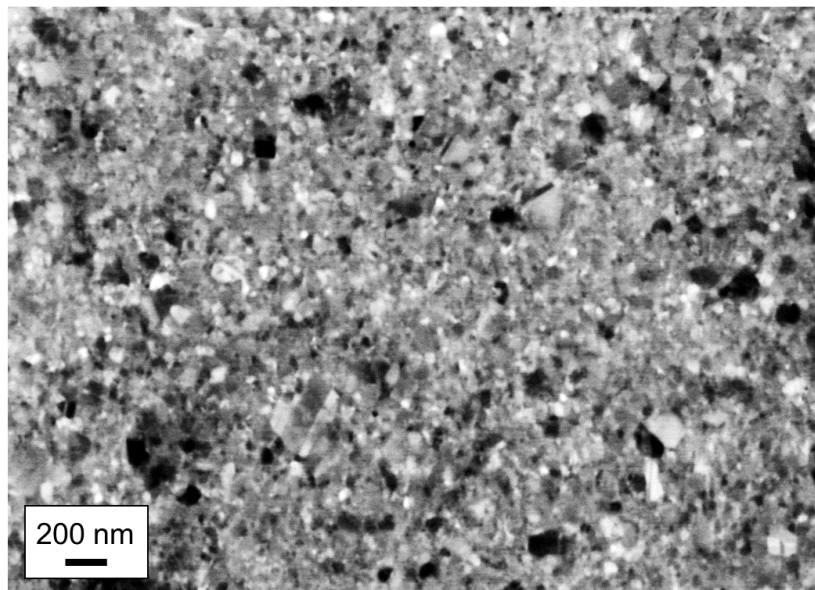

Figure 4.5: SEM-BSE micrograph of CoCrNi MEA processed by HPT and subsequently annealed at 700 ℃ for 10 s.
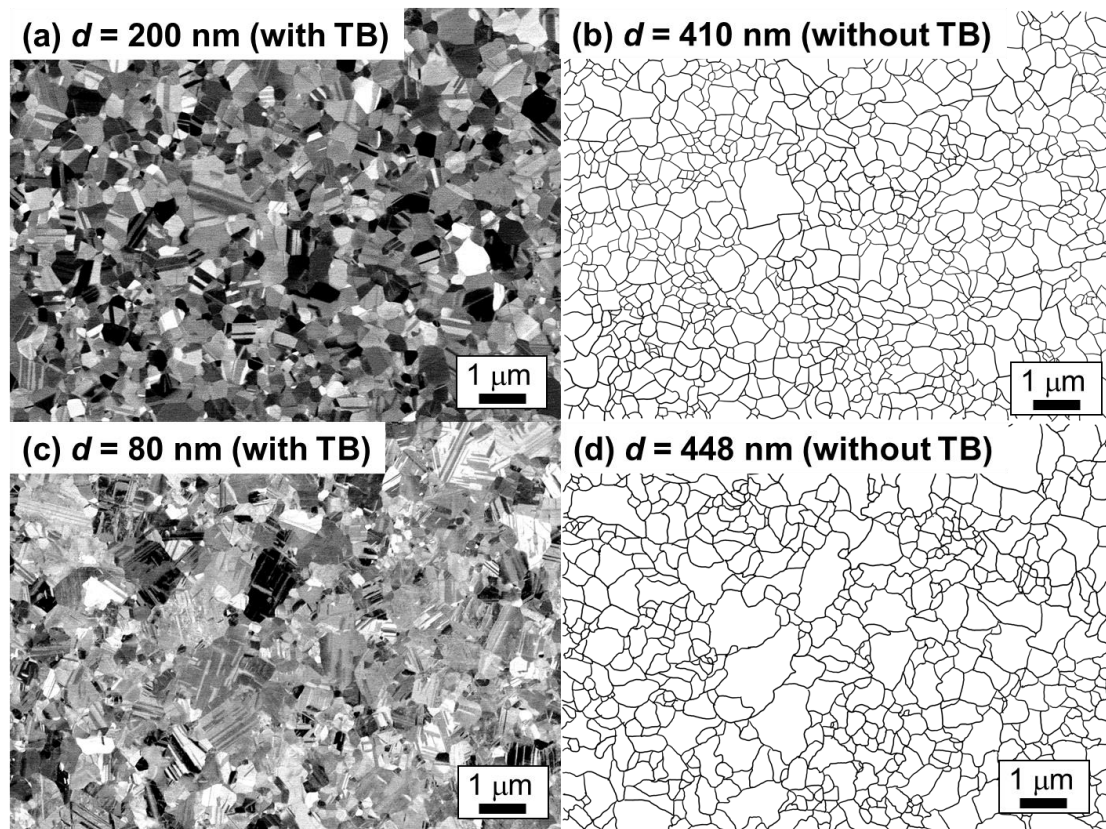
Figure 4.6: SEM-BSE micrographs of (a) CoCrFeMnNi HEA and (c) CoCrNi MEA. Mean grain sizes with annealing TBs are indicated in the upper left. Grain boundary maps of (b) CoCrFeMnNi HEA and (d) CoCrNi MEA without TBs, corresponding to the identical area as shown in (a) and (c), respectively. Mean grain sizes without TBs are indicated in the upper left.

HPT materials, a drastic decrease in peak width was confirmed in both materials, indicating the density of defects significantly decreased after recrystallization. The all the observed peaks were corresponding to FCC structure in both materials.

Figure 4.6 (a) and (c) show SEM-BSE micrographs of microstructure in the HEA and MEA, respectively, after primary recrystallization completed. Profuse annealing twins were observed in all the grains. This seemed to be related to the low SFE owing to the higher concentration of alloying elements. **Figure 4.7 (a) and (d)** show inverse pole
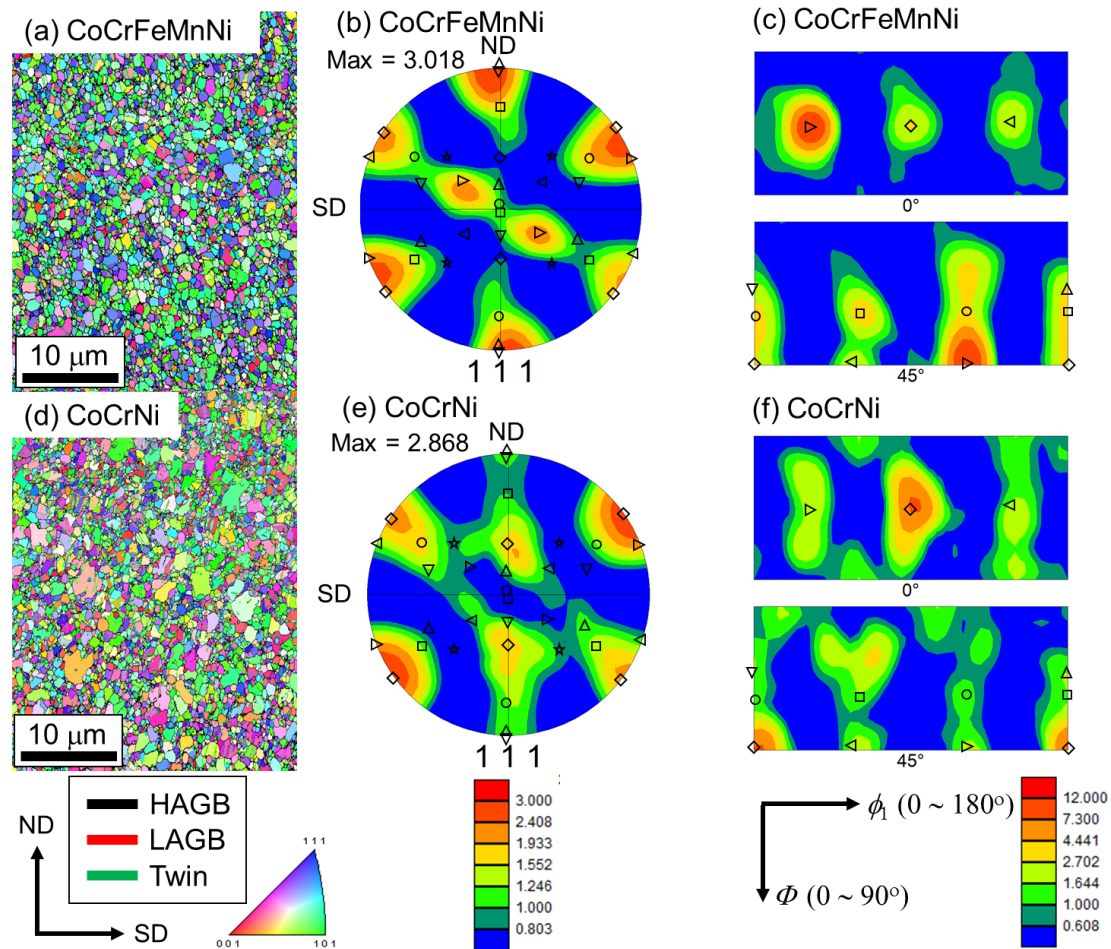
Figure 4.7: EBSD IPF maps and GB maps of (a) CoCrFeMnNi HEA and (d) CoCrNi MEA processed by HPT and subsequently annealed at 800 °C for 10 s and 700 °C for 30 s, respectively. SD and ND are indicated. The black, red, and green lines correspond to HAGB, LAGB, and Twin boundaries, respectively. The colors in the IPF map indicate the orientation of grains along radial direction, and color legend is also indicated. 1 1 1 Pole figures of (b) CoCrFeMnNi HEA and (e) CoCrNi MEA plotted based on (a) and (d), respectively. The points plotted together are typical texture components shown in **table 4.1**. ODF maps of (c) CoCrFeMnNi HEA and (f) CoCrNi MEA plotted based on (a) and (d), respectively. The maps were sectioned at $\phi_2 = 0$ and 45°. Bunge's definition of Euler angle was used. The definition of the symbols plotted together is the same as (b) and (e).

figure (IPF) maps overlapped with their GB maps of CoCrFeMnNi HEA and CoCrNi

MEA, respectively, after primary recrystallization completed. The grains were found to

be surrounded by high-angle grain boundaries (HAGBs) and contained profuse annealing

twin boundaries. The fractions of twin boundaries were estimated as 28 % and 35 % in

the HEA and MEA, respectively. **Figure 4.7 (b) and (c)** are 1 1 1 pole figure and

orientation distribution function (ODF) map, respectively, of CoCrFeMnNi HEA. The symbols plotted together are typical texture components observed in shear-deformed FCC metals [194], as described in **table 4.1**. A^* texture, which is frequently observed in low stacking fault energy materials, was found to be a major component among them. This texture is very similar to the same HEA processed by HPT at room temperature [190]. **Figure 4.7 (e) and (f)** are 1 1 1 pole figure and ODF map, respectively, of CoCrNi MEA. C texture was found to be a major component in the MEA. Further study is necessary to clarify the texture difference between the HEA and MEA.

Table 4.1: Typical texture components in shear-deformed FCC metals [194]. SD and ND are shear direction and shear plane normal direction, respectively.

Notation	Symbol	{u v w} $\perp$ ND	<h k l> // SD
A_1	▲	(1 1 -1)	[1 -1 0]
A_2	▼	(-1 -1 1)	[-1 1 0]
A^*_1	◁	(1 1 -1)	[2 -1 1]
A^*_2	▷	(1 -1 1)	[-2 -1 1]
B_1	○	(1 1 -2)	[1 -1 0]
B_2	□	(-1 -1 2)	[-1 1 0]
C	◊	(1 0 0)	[0 -1 1]
	☆	(1 0 0)	[0 0 1]

Figure 4.8 (a) shows the BF-TEM micrograph of CoCrFeMnNi HEA after primary recrystallization completed. Equiaxed grains having profuse annealing twins could be seen. **Figure 4.8 (b)** is a SAD pattern taken in the same area as **figure 4.8 (a)**. It showed many spots, suggesting that the material was fully-recrystallized. **Figure 4.8 (c) and (d)** are examples of DF-TEM micrographs of recrystallized grains. It was found that many of the grains contained a small number of dislocations. **Figure 4.9 (a)** shows the BF-TEM

micrograph of CoCrFeMnNi HEA after primary recrystallization completed. Similar to
the HEA, equiaxed grains having profuse annealing twins could be seen. **Figure 4.9 (b)**
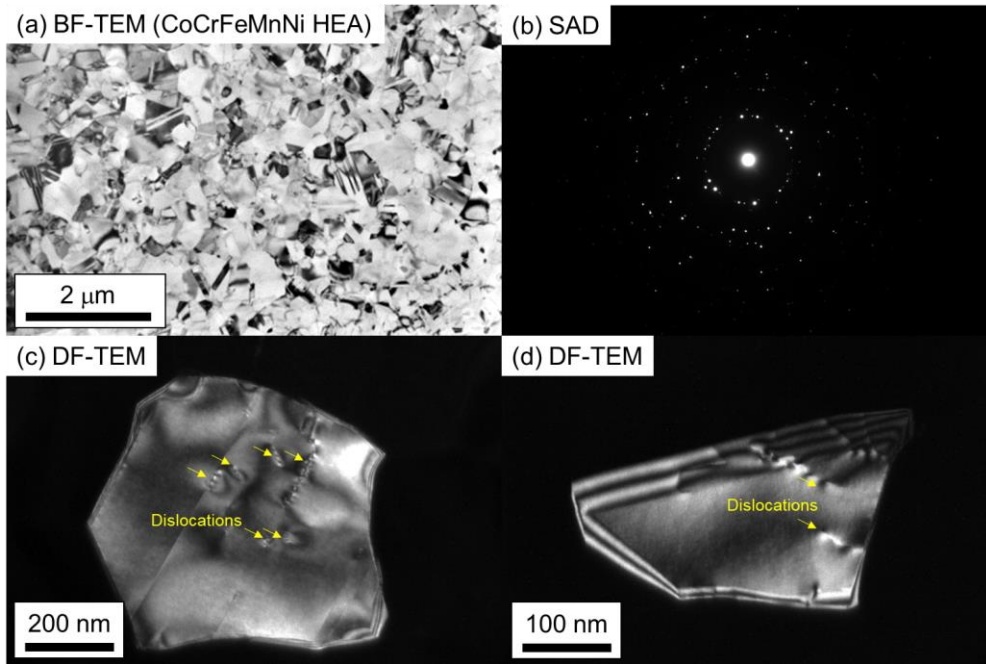is a SAD pattern taken in the same area as **figure 4.9 (a)**. **Figure 4.9 (c) and (d)** are

Figure 4.8: (a) BF-TEM micrograph of CoCrFeMnNi HEA processed by HPT and
subsequently annealed at 800 ℃ for 10 s. (b) SAD pattern taken at the same area as
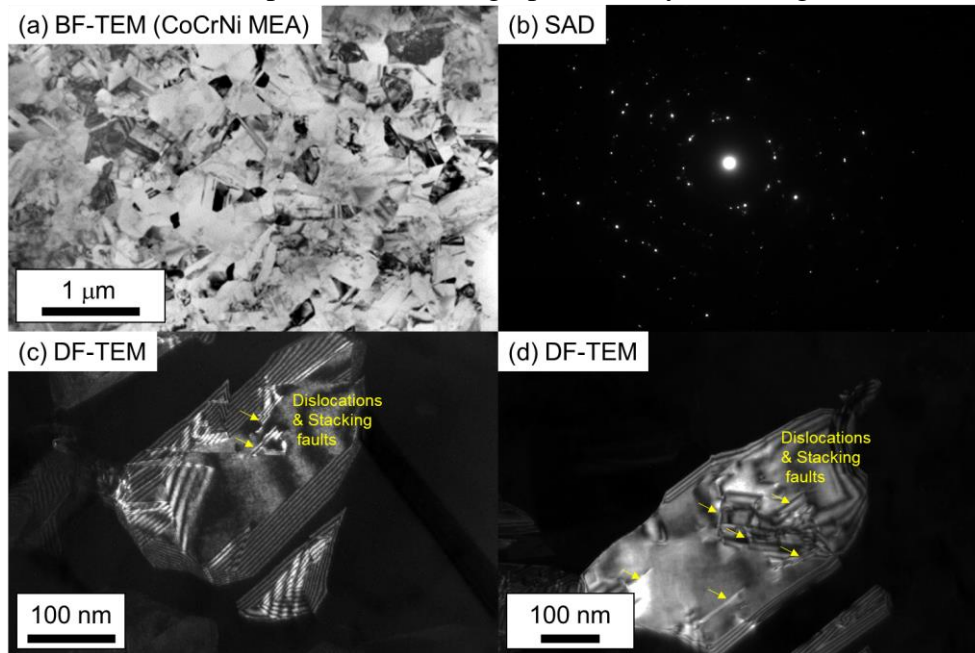shown in (a). (c, d) Examples of DF-micrographs of recrystallized grains.

Figure 4.9: (a) BF-TEM micrograph of CoCrNi MEA processed by HPT and
subsequently annealed at 700 ℃ for 30 s. (b) SAD pattern taken at the same area as
shown in (a). (c, d) Examples of DF-micrographs of recrystallized grains.

examples of DF-TEM micrographs of recrystallized grains. It was found that many of the grains contained a small number of dislocations and stacking faults, similar to the HEA. The implication of these facts will be discussed later.

In **figure 4.6 (b) and (d)**, GB maps without twins were also shown. It was found that the mean grain size (without/with twin boundaries (TBs)) of the HEA and MEA were 410/200 and 448/80 nm, respectively. **Figure 4.10 (a) and (b)** show grain size (with TBs) distribution in CoCrFeMnNi HEA and CoCrNi MEA, respectively, after primary recrystallization completed. It was noteworthy that the grain size distribution was much narrower than the reported cases of conventional materials processed under conventional methods [195]. Besides, it is also worth noting that such surprisingly ultrafine single-phase microstructure after recrystallization has been rarely reported. Particularly, the mean grain size (with twins) of 80 nm in the MEA was the finest among the materials having FRex-UFG microstructure with single-phase reported to date.
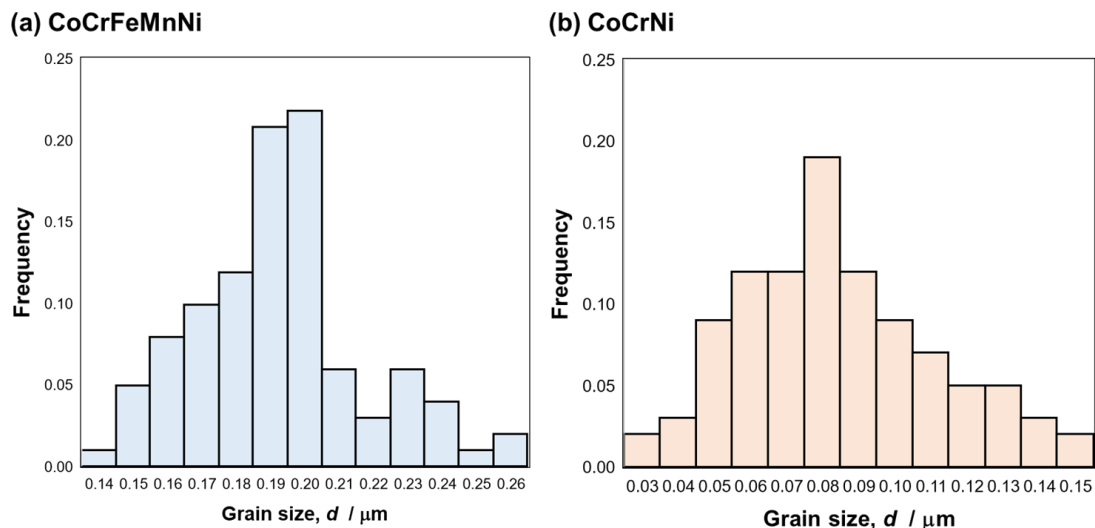

Figure 4.10: Grain size distribution in (a) CoCrFeMnNi HEA and (b) CoCrNi MEA processed by HPT and subsequently annealed at 800 ºC for 10 s and 700 ºC for 30 s, respectively.

4.3.3. Mechanical properties of recrystallized materials

Figure 4.11 (a) shows nominal stress-nominal strain curves of CoCrFeMnNi HEA and CoCrNi MEA having coarse-grained (extracted from literature [42,181]), fully-recrystallized ultrafine-grained (FRex-UFG), and deformed microstructure. In the case of the coarse-grained materials, the yield strength (0.2 % proof stress) of the HEA and MEA were 234 MPa and 295 MPa, respectively. The coarse-grained materials exhibited high work-hardening, leading to ultimate tensile strength (*UTS*) and elongation to fracture (e_f) of 667 MPa and 75.4 % in CoCrFeMnNi HEA and 731 MPa and 67.9 % in CoCrNi MEA. In the as-HPT state, the HEA and MEA exhibited yield strength of 1540 MPa and 2117 MPa, respectively, without elongation. This was due to plastic instability [163], expressed as

$$d\sigma/d\varepsilon \leq \sigma, \qquad (4.6)$$

where σ is true stress and ε is a true strain. When **eq. (4.6)** is satisfied, necking occurs followed by fracture. The equation implies that high work-hardenability is necessary to
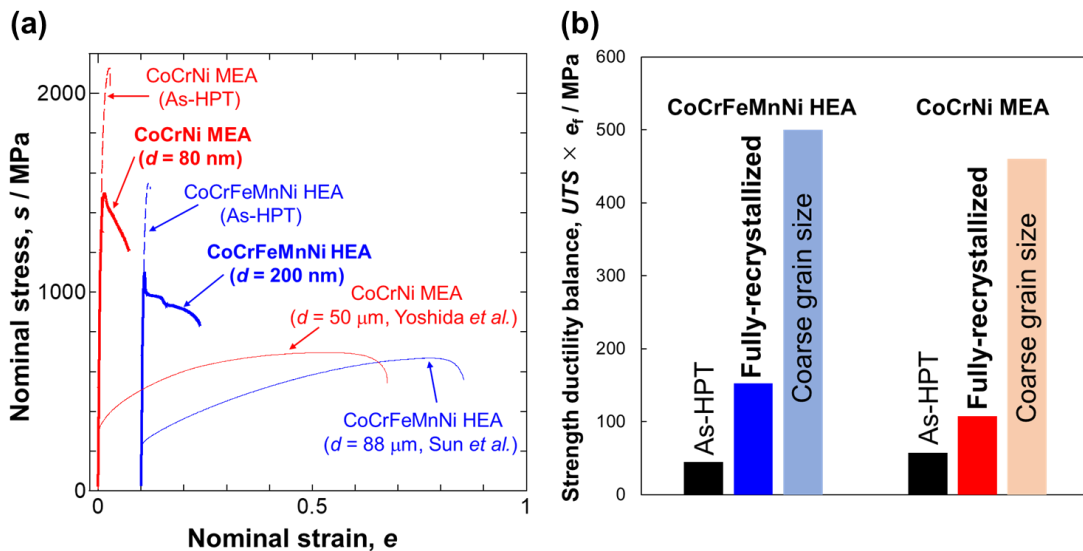

Figure 4.11: (a) Nominal stress-nominal strain curves of CoCrFeMnNi HEA and CoCrNi MEA having deformed, FRex-UFG, and coarse-grained microstructure. (b) Comparison of strength-ductility balance parameter in CoCrFeMnNi HEA and CoCrNi MEA having deformed, FRex-UFG, and coarse-grained microstructure.

postpone necking and achieve large ductility in high strength materials. In as-HPT materials, since work-hardenability was very low owing to high dislocation density, their elongation was limited. In the case of materials having FRex-UFG microstructure, the yield strength of CoCrFeMnNi HEA and CoCrNi MEA were 1099 MPa and 1490 MPa, respectively. *UTS* and e_f were 1082 MPa and 13.7 % in CoCrFeMnNi HEA and 1495 MPa and 7.2 % in CoCrNi MEA. The yield strength of the materials was more than four times higher than those of the coarse-grained materials. The difference in yield strength (σ_Y) can be explained by Hall-Petch effect [51,52], expressed as

$$\sigma_Y = \sigma_0 + kd^{-\frac{1}{2}} \tag{4.7}$$

where σ_0 is lattice friction stress (fundamental resistance to dislocation motion in a crystal lattice), *k* is a constant so-called Hall-Petch slope, and *d* is the mean grain size of the materials. Owing to the small grain size achieved in the FRex-UFG HEA and MEA, very high yield strength can be expected. In addition, the extra-hardening effect, which is commonly observed in various FRex-UFG materials [42,53,57,58,138,196] due to the lack of dislocation sources [196,197], also contributed to the increase in the yield strength. Although necking occurred in the FRex-UFG HEA and MEA just after yielding, the post-uniform elongation was much larger than that of as-HPT materials. This appeared to be due to lower dislocation density in the FRex-UFG microstructure compared with the as-HPT materials, leading to better deformability of necked parts.

In **figure 4.11 (b)**, the strength-ductility balance of the materials was evaluated as shown in **figure 4.11 (a)** based on an artificial parameter *UTS* $\times$ e_f. It was found that the strength-ductility parameters of FRex-UFG materials were several times higher than those of As-HPT materials. The reason for the difference seemed that the deformability

118

of the FRex-UFG materials was better than that of as-HPT materials since fully-recrystallized microstructures could accommodate more lattice defects than deformed microstructures. On the other hand, the strength-ductility parameters of the FRex-UFG materials were smaller than the coarse-grained materials. This was because the plastic instability condition was satisfied at the early stage of deformation in the FRex-UFG materials. Sun *et al*. [181] reported that the strength-ductility balance of CoCrFeMnNi HEA with a mean grain size of about 500 – 600 nm (with twins) was better than that of other grain size materials. Saha *et al*. [55] also reported in high-manganese steel that the strength-ductility balance of the materials with FRex-UFG microstructure with a mean grain size of 400 nm (with twins) was better than other coarse-grained materials. Therefore, by optimizing grain size, materials with excellent strength-ductility balance are expected to be fabricated.

4.3.4. Grain growth kinetics after primary recrystallization completed

After primary recrystallization completed, the HPT-processed materials were subsequently annealed at various temperatures for various holding times to characterize the grain growth behavior of the materials because GB migration kinetics may have a large impact on the formation of FRex-UFG microstructure like **figure 4.6**. The grain growth kinetics of CoCrFeMnNi HEA and CoCrNi MEA was analyzed by the following model [68].

$$d^n - d_0^n = k_0 t\, exp\left(-\frac{Q}{RT}\right) \tag{4.8}$$

where d is grain size after growth, d_0 is grain size after primary recrystallization completed, n is grain growth exponent, k_0 is a constant value, t is annealing time, Q is the

activation energy of grain growth, R is the gas constant, and T is annealing temperature. It should be noted that d and d_0 should be grain size without twins since the mobility of twin boundaries is generally significantly lower than HAGBs [68]. The grain sizes of the HEA and MEA obtained at different temperatures and times are displayed in **figure 4.12 (a) and (b)**, respectively. The data were fitted by **eq. (4.8)** to obtain the activation energy of grain growth, Q, and growth exponent, n. As presented in **table 4.2**, the n values of the HEA and MEA were found to be within the range of $2 < n < 3$; This implied that both the materials maintained FCC single-phase during the annealing at the temperature range. The activation energies of grain growth in the HEA (304 kJmol^{-1}) and MEA (308 kJmol^{-1}) were found to be about three times higher than that of pure Ni (102 kJmol^{-1}) extracted from literature [198], suggesting low GB mobility (sluggish GB migration). Sluggish GB migration has been also reported in other FCC HEAs and MEAs [199,200].
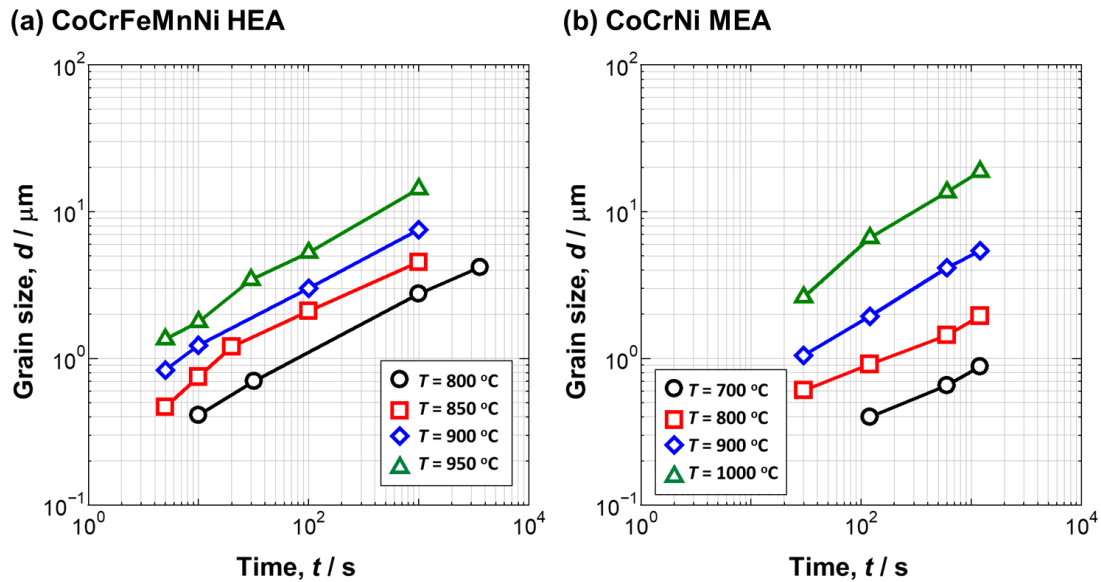

Figure 4.12: Grain size of (a) CoCrFeMnNi HEA and (b) CoCrNi MEA after primary recrystallization completed and grew at different temperatures, plotted as a function of holding time.

Table 4.2: Activation energy of grain growth (Q) and growth exponent (n) in pure Ni [198], CoCrNi MEA, and CoCrFeMnNi HEA calculated by the model (**Eq. (4.8)**).

Materials	Activation energy, Q / kJmol^{-1}	Growth exponent, n
Pure Ni[198]	102	2.0
CoCrNi MEA	308	2.1
CoCrFeMnNi HEA	304	2.3

One possible reason is the so-called solute drag effect [68]. In the process of GB migration, the jump of atoms across GBs happens, and if solute atoms at GB have low potential energy (i.e., attractive interaction with neighboring atoms), GB migration is inhibited. In conventional dilute alloys, the solute drag effect is evident in low-angle (LA) GBs with low velocity [68], but, in high-alloy systems, this effect can be significant even in HAGBs with large velocity due to the variety and high concentration of alloying elements.

To understand the experimental results further, atomistic hybrid MD/MC calculations were performed for simulating grain boundary structures in two-dimensional lattices of artificial HEAs in which the atomic size difference of constituent elements (δ defined by **eq. (4.4)**) (i.e., lattice distortion) and temperature were variables. GB free volumes (V_{GB} defined by **eq. (4.5)**), which is closely-correlated with GB mobility [68], were calculated and normalized by the magnitude of Burgers vector (b) as a function of atomic size difference as shown in **figure 4.13 (a)**. It was found that, with increasing atomic size differences, V_{GB} decreased. This was because atoms having various sizes could geometrically cancel V_{GB}. Since severe lattice distortion is one of the special characteristics of HEAs and MEAs [42,138], V_{GB} of the HEA and MEA can be small. In addition, with decreasing temperature, segregation of specific elements with a few atomic layers happened (as shown in **figure 4.13 (b)** as an example), and V_{GB} decreased. The reduction of V_{GB} by segregation appeared to be because specific elements having large or

small atomic sizes could easily cancel V_{GB} geometrically, contributing to the reduction of the total free energy of the system. In order to have elemental segregation at GBs during recrystallization, the velocity of GB migration and diffusion of alloying elements have to be comparable. According to the data shown in **figure 4.12**, the velocity of GB migration is estimated as about $\sim 10^1$ nm s^{-1} at the beginning of recrystallization and slows down later. On the other hand, according to the reported data of diffusion coefficient [18,21], the velocity of lattice diffusion is estimated as 10^{-1} nm s^{-1}. Therefore, the velocity of lattice
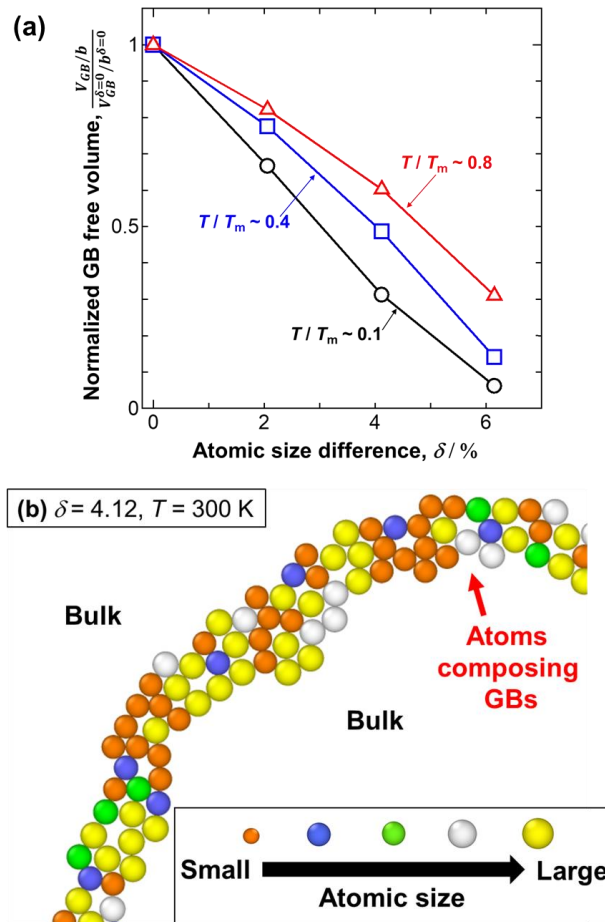

Figure 4.13: (a) Normalized GB free volume in artificial HEAs as a function of the atomic size difference of the constituent elements at $T / T_m \sim 0.1$ (Black circle), 0.4 (Blue square), and 0.8 (red triangles), calculated by hybrid MC/MD simulations. The V_{GB} values were firstly normalized by the magnitude of Burgers vector to eliminated the effect of system size, and then, normalized by the value of pure metal with $\delta = 0$. (b) An example of GB structure in an artificial HEA having $\delta = 4.12$ at 300 K, calculated by the MD simulation. The atoms having five different atomic sizes are composing GBs.

diffusion is about 10^2 times slower than that of GB migration, and it is difficult to have elemental segregation at GBs during recrystallization through lattice diffusion. However, there are other diffusion pathways such as GB diffusion and pipe diffusion along dislocations. Typically, the velocity of diffusion through GB and pipe diffusion is about 10^1 - 10^2 times faster than lattice diffusion [68,201]. Thus, GB segregation of specific elements during recrystallization can occur through the diffusion along GBs and dislocations. It should be noted that experimental observation of such small segregation is extremely challenging unless the concentration reaches certain levels, but GB segregation of some specific elements (such as Co, Ni) has been reported in the HEA [202] and MEA [203] at intermediate temperature. Therefore, the sluggish GB migration could be characterized as an essential nature of HEAs and MEAs and attributed to the massive solute drag effect, severe lattice distortion effect, and elemental segregation at GBs.

4.4. Discussion: Recrystallization mechanisms and microstructure evolution

Finally, the reasons why it was possible to achieve significantly fine FRex-UFG microstructure in the HEA and MEA after HPT and annealing are discussed. Generally, the potential nuclei of recrystallization are believed to exist in the deformed matrix [68] because the formation of nuclei by the thermal fluctuation of atoms is energetically impossible (as discussed later). Such nuclei should be the domains surrounded by HAGBs with high mobility and having lower dislocation density compared with the surrounding matrix, formed under the process of grain subdivision during deformation and recovery

during subsequent annealing [204,205]. If there is a difference in dislocation density (i.e., stored elastic energy) between inside and outside of the nuclei, the migration of GBs happens toward higher dislocation density sides, which is called strain-induced boundary migration [68].

Based on the above picture, critical nuclei size (d^*) over which nuclei could grow stably was calculated. Here, it is considered that there is a nucleus for recrystallization, defined as a domain having low defects density (ρ') and surrounded by HAGBs, in a deformed matrix having high defects density (ρ), as illustrated in **figure 4.14**. For simplicity, the shape of the nucleus is a sphere with a radius of r, and the HAGBs have constant GB energy of γ_{GB}. The nucleus could be formed in the process of grain subdivision during deformation and recovery during subsequent annealing [204,205]. Now, it is considered that the nucleus grows and the radius becomes ($r + \mathrm{d}r$) from r. The thermodynamical driving force for the coarsening is mainly the difference in the elastic energy stored by lattice defects between the inside (E') and outside (E) of the nucleus, so-
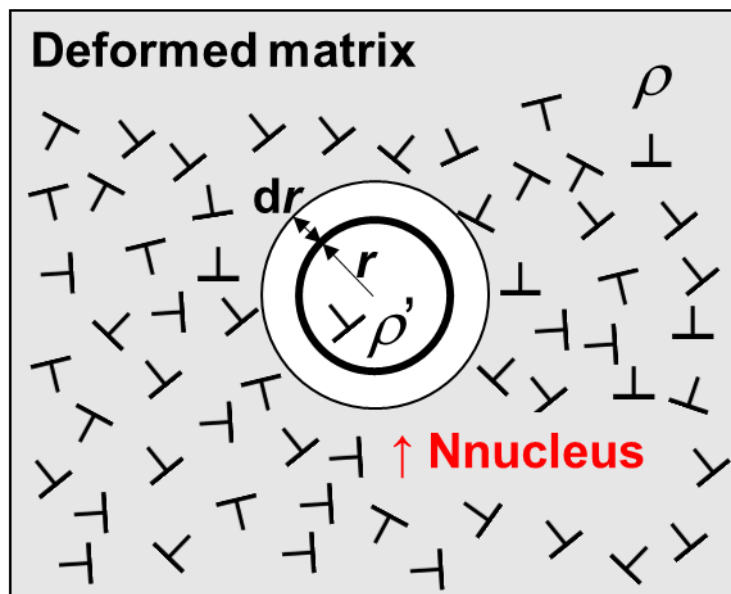

Figure 4.14: Schematic illustration on a nucleus potentially existing in a deformed matrix.

called strain-induced boundary migration (SIBM) [68]. In such a case, the molar free energy change of the system can be expressed as

$$dG(r) = \left(-\frac{4}{3}\pi(r+dr)^3 E + 4\pi(r+dr)^2 \gamma_{\text{GB}}\right) - \left(-\frac{4}{3}\pi r^3 E' + 4\pi r^2 \gamma_{\text{GB}}\right). \quad (4.9)$$

The first and second terms in the brackets in **eq. (4.9)** are the contribution of the bulk free energy and surface energy of GBs, respectively. Neglecting the higher-order terms, **eq. (4.9)** yields

$$\frac{dG(r)}{dr} dr = (-4\pi r^2 \Delta E + 8\pi r \gamma_{\text{GB}})dr, \quad (4.10)$$

where $\Delta E = E - E'$. When dG takes local maximum $\left(\frac{dG(r^*)}{dr} = 0\right)$, the critical nuclei size $(d^* = 2r^*)$ over which the nucleus can grow stably is expressed as

$$d^* = \frac{4\gamma_{\text{GB}}}{\Delta E}. \quad (4.11)$$

Assuming that the lattice defects storing elastic energy are mainly dislocations, ΔE can be expressed as

$$\Delta E = \alpha\mu b^2(\rho - \rho'), \quad (4.12)$$

where α is a constant related to line tension of dislocations, μ is shear modulus, b is the magnitude of burgers vectors. If $\rho \gg \rho'$ is assumed, **eq. (4.11)** can be

$$d^* = \frac{4\gamma_{\text{GB}}}{\alpha\mu b^2 \rho}. \quad (4.13)$$

In FCC HEAs and MEAs, α is reported as 0.06125 [63]. μ of CoCrFeMnNi HEA and CoCrNi MEA are reported as 80 GPa [206] and 91 GPa [207], respectively. b of the HEA and MEA were determined as 0.2545 nm and 0.2520 nm, respectively, by using synchrotron XRD measurement. It should be noted that the nuclei larger than d^* grow, but those smaller than d^* do not shrink like the cases of the nuclei for phase transformation because the shrinking of nuclei requires the production of lattice defects in the matrix,

125

which has never been observed. Instead, nuclei smaller than d^* are eaten by other growing nuclei to reduce the total free energy of the system. By looking at **eq. (4.13)**, it is possible to understand that dislocation density (which is considered to be proportional to the fraction of HAGBs) is a major parameter for controlling the recrystallization behavior of materials. Therefore, potential nuclei can exist in regions with large misorientation, such as shear bands, deformation bands, near original GBs.

This idea was first proposed by Cahn [204], and its supporting experimental evidence has been reported. For example, Yu *et al.* [205] investigated recovery and recrystallization in heavily deformed pure aluminum by particularly focusing on GB triple-junctions (with Y-shape) of elongated grains in a deformed matrix. They revealed that the triple-junctions migrated during the early stage of annealing accompanying the annihilation of dislocations, and equiaxed grains having low dislocation density formed. Subsequently, coarsening of some of the equiaxed grains (i.e., recrystallization) was confirmed. The idea is also supported by the fact that the texture of the HEA and MEA were very similar to deformation texture and that the grains after primary recrystallization completed contained a small number of defects, which were possibly introduced before nucleation (during deformation).

If $\gamma_{GB} = 1.0 \ \mathrm{Jm^{-2}}$ (typical value for transition metals) is assumed, the critical size of nuclei in CoCrFeMnNi HEA is calculated as 370 nm. This is much larger than the typical critical nuclei size for phase transformation (~ several nm). The formation of such large nuclei by the thermal fluctuation of atoms is energetically very difficult. Thus, it is reasonable to consider that there are potential nuclei in a deformed matrix.
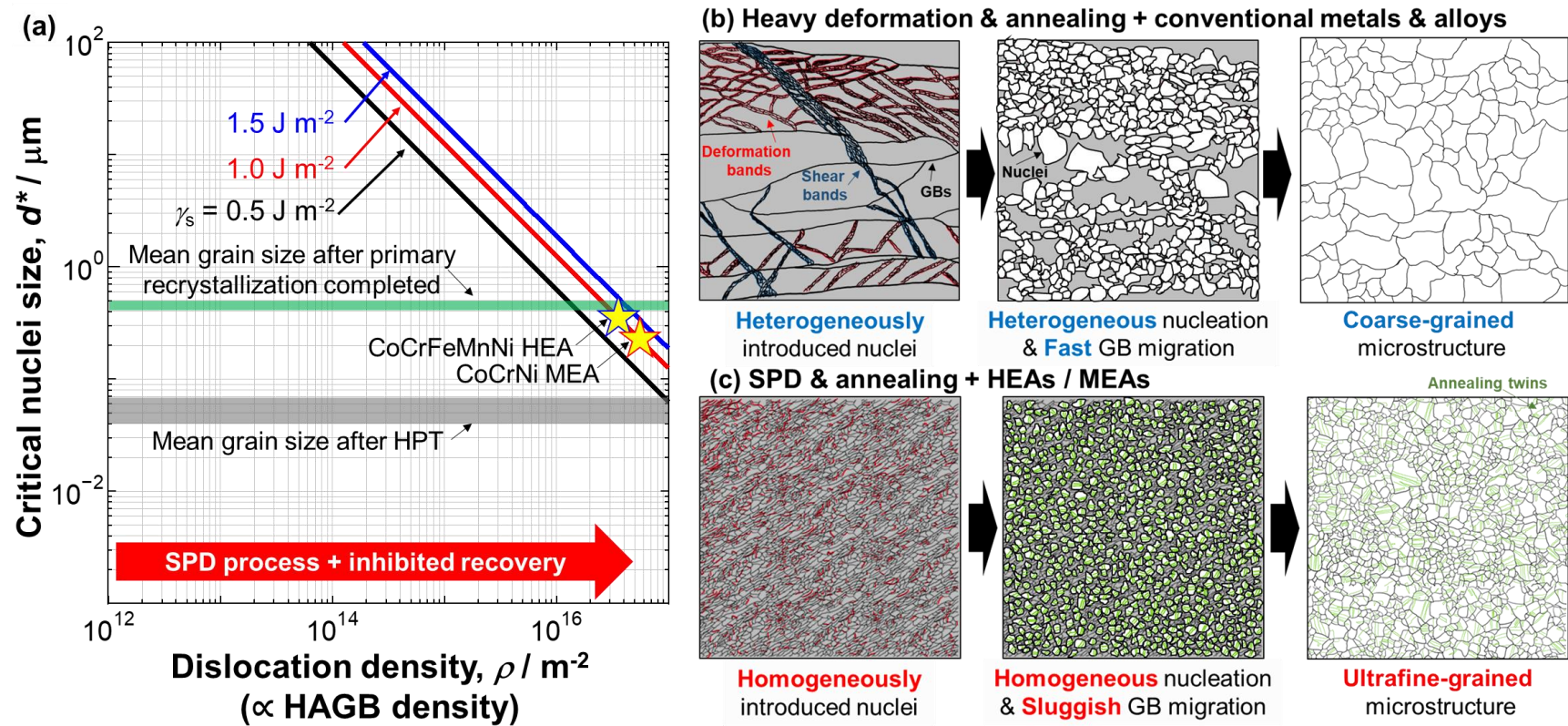
Figure 4.15: (a) Critical nuclei size as a function of dislocation density (ρ) with possible value ranges of grain boundary surface energy (γ_s) in transition metals and HEAs[208]. The critical nuclei size (calculated by **eq. (4.13)**) in CoCrFeMnNi HEA and CoCrNi MEA are plotted together. The mean grain sizes of the HEA and MEA after HPT and after primary recrystallization completed are also indicated. Schematic illustration of microstructure evolution during annealing in the cases of (b) conventional heavy deformation processes applied to conventional metals and alloys and (c) severe plastic deformation process applied to HEAs and MEAs. The black and red lines are HAGBs and LAGB, respectively. The green lines are TBs. The gray and white areas are deformed and recrystallized parts, respectively.

In **figure 4.15 (a)**, critical nuclei sizes of the HEA and MEA were plotted as a function of dislocation density (ρ) with possible GB surface energy value range in transition metals and HEAs [208]. It is clearly seen that, with increasing dislocation density (i.e., increasing the fraction of HAGB) by deformation, smaller critical nuclei size (i.e., higher nuclei density ($\rho_{Nuc} \propto 1 / d^*$)) is achieved. The calculated value ranges of the critical nuclei sizes of the materials are displayed in the figure. The values were similar to the size of the nucleated grains shown in **figure 4.5**. The mean grain sizes of the materials after HPT and after primary recrystallization completed were also indicated. One can find that the grain sizes after HPT were smaller than the critical nuclei size. This implied that nuclei were formed through recovery (triple-junction migration accompanying with the annihilation of dislocations) at the beginning of the annealing process. The grain sizes of the recrystallized materials were larger than the critical size of nuclei, but these have a similar order of magnitude, suggesting slight growth of nuclei happened until they collided with each other.

Now, it is considered that conventional heavy deformation processes (such as cold-rolling, for instance) are applied to conventional dilute alloys or pure metals (**Figure 4.15 (b)**). In such processes, deformation is microscopically very heterogeneous, and the domains with large misorientation (where many potential nuclei exist) are mainly introduced at near original GB, deformation bands, shear bands. The density of the potential nuclei in the deformed matrix is limited owing to dynamic recovery during deformation. So that, nucleation happens heterogeneously and sparsely. The growth of the nuclei is fast until they collide with each other and slows down afterward. It should be noted that the incubation time required for nucleation (i.e., time to form nuclei through recovery [205]) is different in each nucleus. Thus, because of the high GB mobility, the

size difference between grains nucleated earlier and later is large, leading to a coarse and heterogeneous microstructure. Generally, the minimum mean grain size obtained by the above processes has been limited to several μm.

On the other hand, in the present study, HPT was applied to the HEA and MEA (**Figure 4.15 (c)**). Compared with the above processes, there are several advantages for achieving finer microstructure as follows: (1) In SPD processes like HPT, the domains having large misorientation are introduced to entire parts of the materials due to large applied strain. (2) In addition, dynamic recovery during deformation is inhibited owing to the low SFE and the interaction between dislocations and the chemical heterogeneity on an atomic-scale. Therefore, severe grain subdivision happens and, the density of potential nuclei is expected to be much higher than in the above case. (3) Moreover, as suggested by **figure 4.15 (a)**, the growth of nuclei was suppressed owing to sluggish GB migration in the HEA and MEA. Therefore, the size difference among grains nucleated earlier and later is small. So that, FRex-UFG microstructure with homogeneous grain size distribution is obtained. (4) Furthermore, because of the low SFE of the materials, annealing twins are introduced with high density, resulting in significantly fine FRex-UFG microstructure.

4.5. Conclusion

In brief, the special characteristics of FCC HEAs and MEAs such as inhibited dynamic recovery and sluggish GB migration, which are closely correlated with the chemical heterogeneity on an atomic-scale, have a great impact on their recrystallization behavior. The unique recrystallization behavior of HEAs and MEAs allows approaching the limit of grain-refinement by recrystallization.

Chapter 5: Concluding remarks and future outlooks

5.1. Essential nature of high/medium entropy alloys

In this dissertation, the essential nature of HEAs and MEAs was clarified. The special characteristics of HEAs compared with conventional dilute alloys can be explained based on the idea of the heterogeneity of chemistry on an atomic-scale. As schematically illustrated in **figure 5.1**, the atomic sites in the crystal lattice of HEAs and MEAs are occupied by different constituent elements, and the lattice is distorted due to the difference in the atomic sizes as explained in Chapter 2. Thus, high-alloy systems are considered to be very heterogeneous on atomic-scale. This is very different from the structure of conventional dilute systems where most of the atomic sites are occupied by solvent elements (i.e., Homogeneous on atomic-scale). The interaction between the
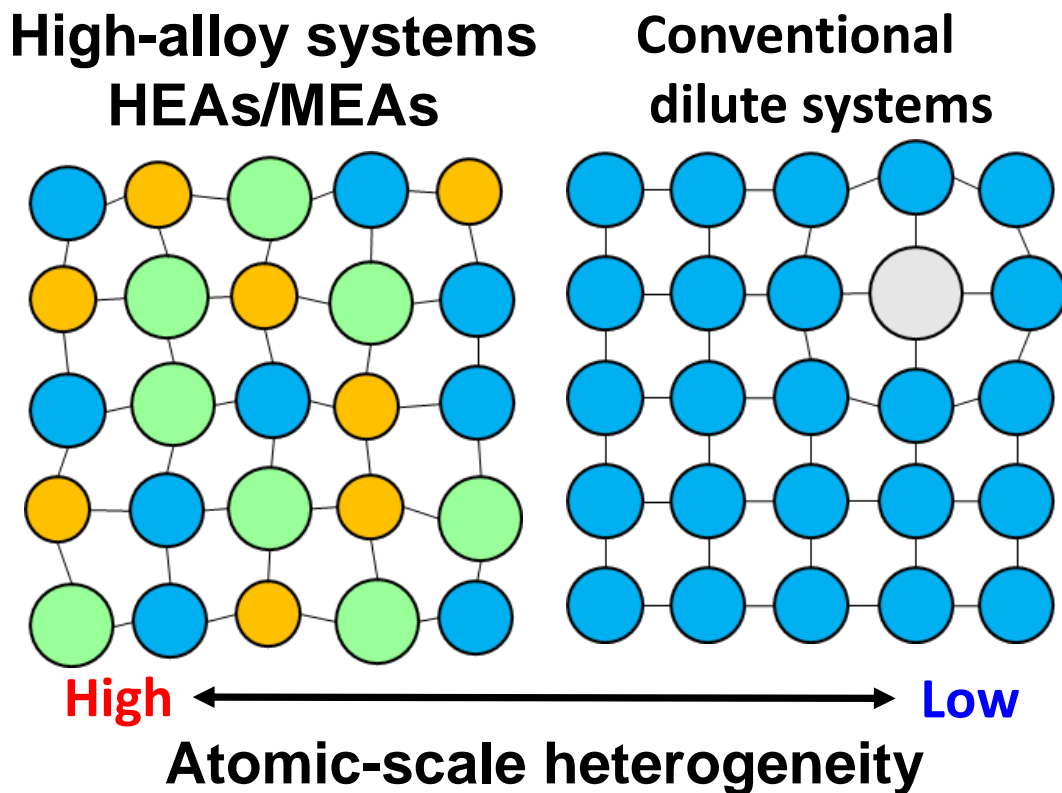
Figure 5.1: Schematic illustration crystal lattices comparing the atomic-scale heterogeneity of conventional dilute systems and high-alloy systems including HEAs and MEAs.

atomic-scale heterogeneity and lattice defects such as dislocations, planar faults, and GBs were found to play a significant role in the macroscopic deformation behavior and microstructure evolution in high-alloy systems. The key results in the present dissertation are summarized as follows.

In Chapter 1, some of the important previous studies including the concept of four core effects were briefly reviewed, and the key issue, main focus, and structure of the dissertation were explained.

In Chapter 2, the effect of elemental combinations on the friction stress (fundamental resistance to dislocation motion in a crystal lattice) and Hall-Petch relationship of various HEAs and MEAs (e.g., CoCrFeNi, and CoCrNi) with FCC structure was investigated. The specimens with fully-recrystallized microstructures of FCC single-phase with various mean grain sizes down to the sub-micrometer scale were obtained by HPT and subsequent annealing. Tensile tests were performed at room temperature to obtain precise Hall-Petch relationships and friction stresses of the materials. Experimental values of the friction stresses were found to fit with the mean-field Labusch model and Leyson-Varvenne model very well. This indicated that the interaction between the elastic field of dislocations and misfit volumes of alloying elements (i.e., Severe lattice distortion) was the dominant factor determining the strength of HEAs and MEAs with FCC single-phase. In addition to that, finally, a new strengthening mechanism by element-element interaction was proposed as an additional mechanism to enhance the strength in FCC HEAs and MEAs.

In Chapter 3, characteristics of the deformation microstructure evolution and macroscopic deformation behavior in FCC high-alloy systems, such as HEAs/MEAs,

austenitic steels were clarified. The deformation behavior of the $Co_{60}Ni_{40}$ alloy and $Co_{20}Cr_{40}Ni_{40}$ MEA having low and high friction stress, respectively, but having the same materials properties such as SFE, elastic constants, and lattice constant was compared. Tensile yield strength and work-hardenability of the $Co_{20}Cr_{40}Ni_{40}$ MEA were much higher than those in the $Co_{60}Ni_{40}$ alloy. Coarse DCs developed in the $Co_{60}Ni_{40}$ alloy, and a small fraction of DTs was observed if the TA was close to <1 1 1>. In contrast, in the $Co_{20}Cr_{40}Ni_{40}$ MEA, fine DCs developed in grains with TA~//<1 0 0>, while PDS were formed in other grains. DTs with high-density were seen in grains with TA~//<1 1 1>. Three-dimensional electron tomography revealed that the PDS developed by confining dislocations in specific {1 1 1} plane, and Lomer-Cottrell immobile dislocations were formed at the intersection of two different slip systems. In-situ X-ray diffraction during tensile deformation clarified different internal stress and texture development in these alloys. Planar fault probability and dislocation density in the $Co_{20}Cr_{40}Ni_{40}$ MEA were found to be higher than those in the $Co_{60}Ni_{40}$ alloy. The results suggested that the cross-slip of dislocations in FCC high-alloy systems is inhibited owing to (1) chemical heterogeneity-induced stacking fault width variation, (2) applied stress (friction stress)-induced stacking fault width variation, and (3) the element-element interaction. In addition, the MTN model could explain the orientation dependence of deformation twining and the reason for the difference in DTs fraction in the two alloys. All these lead to the conclusion that FCC high-alloy systems inherently develop characteristic deformation microstructures owing to the atomic-scale heterogeneity, and they are advantageous for obtaining superior mechanical properties.

In Chapter 4, the special characteristics of recrystallization in FCC HEAs and MEAs were investigated. The materials were processed by HPT and subsequent annealing at

133

high temperature. As-deformed materials exhibited nanocrystalline microstructure with high dislocation density composed of elongated and fragmented grains with a size of several tens nm. After annealing, FRex-UFG microstructure with FCC single-phase and high-density annealing twins was obtained. Surprisingly, mean grain sizes (without/with twin boundaries) of the HEA and MEA were 410/200 and 448/80 nm, respectively, which were the smallest among the fully-recrystallized single-phase materials ever reported. The activation energy of grain growth in the materials were three times higher than that of pure Ni. The atomistic simulations revealed that GB mobility of the HEA and MEA could be low due to (1) massive solute drag effect at GBs and geometrical cancellation of GB free volumes by (2) lattice distortion and (3) GB segregation. It was concluded that significantly fine recrystallization microstructure could be inherently attained owing to (1) the high lattice defect density and (2) low GB mobility in the severe plastically-deformed HEA and MEA.

All the results described above were closely correlated with the interaction between lattice defects and the atomic-scale heterogeneity in HEAs and MEAs. In brief, the interaction between dislocations (and stacking faults at the core) and the atomic-scale heterogeneity contribute to the increase in yield strength (Chapter 2) and work-hardenability (Chapter 3), and it leads to superior mechanical properties of FCC HEAs and MEAs compared with conventional metals and alloys. The interaction between GBs and the atomic-scale heterogeneity leads to a decrease in GB mobility, and this contributed to the significant grain refinement after SPD and annealing processes in FCC HEAs and MEAs (Chapter 4). Thus, the atomic-scale heterogeneity can be a useful concept to universally understand the essential nature of HEAs and MEAs as well as the nature of conventional metals and alloys.

5.2. Future outlook

The concept of the atomic-scale heterogeneity should also apply to the dynamics of other lattice defects.

(1) 0-dimensional defects: vacancies, interstitials

As described in Chapter 1, the average formation energy and migration energy of vacancies in HEAs and MEAs may not be different from conventional metals and alloys. However, the variation of vacancy migration energy due to the atomic-scale heterogeneity can cause trapping of vacancies resulting in sluggish diffusion kinetics in HEAs and MEAs.

Another interesting problem is the effect of interstitials on the properties of HEAs and MEAs. Similar to the substitutional elements in solid solution alloys, interstitials should interact with defects like dislocations leading to strengthening. For instance, Moravcik *et al.* [209] reported that the friction stress of CoCrNi MEA increased by 38 MPa by adding 0.47 at. % Nitrogen. Stepanov *et al.* [210,211] also confirmed the increase in the friction stress of CoCrFeMnNi HEA by adding Carbon. Systematic investigations are highly demanded to unveil the effect of interstitials on the mechanical properties of HEAs and MEAs.

(2) 1-dimensional defects: dislocations in various crystal structures

Labusch's theory-based models used in Chapter 2 can apply to the edge dislocations in HEAs and MEAs with HCP and BCC structures. The Leyson-Varvenne model was previously employed to analyze the behavior of basal dislocations in Mg alloys [212,213].

However, due to the difficulty in the fabrication of HEAs and MEAs with HCP structure [214,215], their deformation behavior has been rarely reported. Bu *et al*. [216] observed $<c + a>$ dislocations in an HCP HEA and they argued that the easiness of the activation of $<c + a>$ slip systems could be explained by the c/a ratio as employed for the analysis of conventional HCP metals and alloys. More experimental evidence must be accumulated to understand the slip behavior of dislocations in HCP HEAs and MEAs.

A recent study done by Maresca *et al*. [86] showed that the Leyson-Varvenne model could explain the strength of BCC HEAs at high temperatures as well as room temperature. Also, they constructed a theoretical model that applied to the screw dislocations in BCC HEAs as well as dilute alloys [87]. In BCC high-alloy systems, screw dislocations can form kinks on different {1 1 0} planes depending on the local chemical environment, and such a complex core structure requires high stress to move (i.e., strengthening). The theories need to be validated by careful experiments in the future. This complex character of screw dislocations may also contribute to the deformation microstructure evolution.

Furthermore, the idea of high-entropy materials can apply to other complex crystal structures such as intermetallics and ceramics [217]. Very few experimental data on the dislocation dynamics in such very complex crystals have been reported to date.

Additionally, the effect of SRO on the mechanical properties of HEAs and MEAs is a controversial issue. As demonstrated in Chapter 2, there is no significant contribution of SRO on the friction stress of HEAs and MEAs annealed at high temperature and followed by fast-quenching. However, how SRO contributes to the work-hardening behavior of metals is not clear. Gerold and Karnthaler [137] argued that the reason for the formation of planar dislocation microstructure in FCC alloys was attributed to the

destruction of SRO by dislocation slip that caused the decrease in CRSS of the following dislocations on the same {1 1 1} planes. This effect is the so-called glide plane softening. Since the planar slip of dislocations can increase the internal stress, the work-hardening rate can be enhanced compared with the materials without SRO. However, as demonstrated in Chapter 3, the formation of PDS is highly orientation dependent. Therefore, it is necessary to systematically investigate the deformation microstructure evolution in materials with SRO depending on the grain orientation against the deformation axis to reveal the true contribution of SRO on the mechanical properties.

(3) Multi-dimensional defects: Martensitic transformation

In some HEAs and MEAs, martensitic phase transformation induced by quenching and deformation has been reported in the past several years. Generally, martensite provides additional phase interfaces acting as obstacles for dislocation motion. In addition, due to the difference in deformability (i.e., availability of slip systems) between matrix and martensite, internal stress can increase owing to the elastic interaction between them. These lead to enhanced work-hardenability. The nucleation and growth of martensite can be affected by the atomic-scale heterogeneity, but, due to the lack of investigation, the details are still unclear.

(4) Multi-dimensional defects: Cracks

Zhang *et al*. [218] showed that the origin of the excellent toughness of CoCrFeMnNi HEA could the nucleation of DTs at the tip of cracks. As demonstrated in Chapter 3, such nucleation of DTs can be also related to the atomic-scale heterogeneity although the

nucleation mechanism may be different in cracking. Further study is necessary to understand the cracking and fracture behavior of HEAs and MEAs.

All these interactions between various types of lattice defects and the atomic-scale heterogeneity should lead to characteristic deformation microstructure development and deformation behavior like the example shown in Chapter 3. In addition, such deformation microstructures also affect the microstructure evolution during thermo-mechanical processing. Further investigation in the future must be able to give valuable hints to clarify the details of the interaction processes and their impact on the macroscopic properties of materials.

Above all, revealing the essential nature of HEAs and MEAs allows to drastically deepen the general understanding of metallurgy. As a result, it becomes possible to design new alloys having ultimate properties by engineering their atomic-scale heterogeneity in near the future.

Appendix A : Equivalence between the mean-field Labusch model and Leyson-Varvenne model

Here, the equivalence between the mean-field Labusch model and the Leyson-Varvenne model is discussed. Assuming that $b = a/\sqrt{2}$ and $\nu = 0.33$ (typical values in FCC metals), **eq. (2.25)** is rewritten as

$$\frac{\tau(0\text{K})}{G} = 0.0810\alpha^{-\frac{1}{3}}f_1(w_c)\left[\sum_n c_n\left(\frac{\Delta\overline{V}_n}{V_{\text{alloy}}}\right)^2\right]^{\frac{2}{3}} \tag{A1}$$

If $\Delta\overline{V}_n/V_{\text{alloy}}$ is small enough, $\Delta\overline{V}_n/V_{\text{alloy}} \sim 3\,(\text{d}a\,/\,\text{d}c_n)\,/\,a$, and **eq. (A1)** is approximated as

$$\frac{\tau(0\text{K})}{G} \sim 0.3503\alpha^{-\frac{1}{3}}f_1(w_c) \times \left[\sum_n c_n\left(\frac{1}{a}\frac{da}{dc_n}\right)^2\right]^{\frac{2}{3}} \tag{A2}$$

This results in

$$\frac{\tau(0\text{K})}{G} \sim 0.3503\alpha^{-\frac{1}{3}}f_1(w_c) \times \varepsilon_{\text{ave}}^{\frac{4}{3}} \tag{A3}$$

as approximated as

$$\sum_n c_n\left(\frac{1}{a}\frac{da}{dc_n}\right)^2 \sim \varepsilon_{\text{ave}}^2 \tag{A4}$$

Eq. (A3) is identical to **eq. (2.5)**. If $\alpha = 0.06125$, and $f_1(w_c) = 0.35$ (as same as Section 4.2.3), the value of the slope in **eq. (A3)** $(= 0.3503\alpha^{-\frac{1}{3}}f_1(w_c))$ is calculated as 0.311, which agrees very well with the slope shown in **figure 2.10** $(= 0.329)$. Thus, the mean-field Labusch model and Leyson-Varvenne model can be regarded as equivalent.

In addition, by looking at the slope $(0.3503\alpha^{-\frac{1}{3}}f_1(w_c))$, it can be understood that the reason for the difference in slopes depending on the alloy systems presented in **figure**

2.10 (b) is mainly due to the difference in (1) dislocation line tension (α) and (2) dislocation core structure (i.e., SFE) ($f_1(w_c)$).

Appendix B: Additivity of potential energy variation

Regarding the additivity of potential energy variation, ΔE, in **figure 2.12**, there is a mathematical background. Now, it is considered that three independent statistical populations A, B, C, and taking real numbers (a, b, c) from the populations: $a \in A, b \in B, c \in C$. Here it is assumed that the real numbers a, b, and c follow the normal distribution with the average of zero, which corresponds to the atomistic variations of potential energies in HEAs shown in **figure 2.12**. In this case, the standard deviation of each statistical population is $\sqrt{\langle a^2 \rangle}, \sqrt{\langle b^2 \rangle}, \sqrt{\langle c^2 \rangle}$ for A, B, C, respectively. Now, there is a set of the summation of the three statistical populations, $A \oplus B \oplus C$. Based on the theory of statistics, the addition theorem of the normal distributions can be applied, and $A \oplus B \oplus C$ also follows standard deviation with the average of zero, so that the standard deviation of the set of three populations $A \oplus B \oplus C$ is $\sqrt{\langle a^2 \rangle + \langle b^2 \rangle + \langle c^2 \rangle}$. In this study, it was assumed that the values of ΔE_{PM}, ΔE_{LD}, ΔE_{AR} follow the independent normal distributions with standard deviations of $\sqrt{\langle (\Delta E_{PM})^2 \rangle}, \sqrt{\langle (\Delta E_{LD})^2 \rangle}, \sqrt{\langle (\Delta E_{ee})^2 \rangle}$, respectively. Then the zero-point of potential energy is set so that average values of ΔE_{PM}, ΔE_{LD}, ΔE_{AR} become zero. Accordingly, applying the addition theorem of the normal distributions described above, the additivity of ΔE is obtained as $\left(\sqrt{\langle (\Delta E_{PM})^2 \rangle + \langle (\Delta E_{LD})^2 \rangle + \langle (\Delta E_{ee})^2 \rangle} \right)$, as shown in **figure 2.12**.

Bibliography

[1]   J.-W. Yeh, S.-K. Chen, S.-J. Lin, J.-Y. Gan, T.-S. Chin, T.-T. Shun, C.-H. Tsau, S.-Y. Chang, Nanostructured high-entropy alloys with multiple principal elements: novel alloy design concepts and outcomes, Adv. Eng. Mater. 6 (2004) 299–303. https://doi.org/10.1002/adem.200300567.

[2]   B. Cantor, I.T.H. Chang, P. Knight, A.J.B. Vincent, Microstructural development in equiatomic multicomponent alloys, Mater. Sci. Eng. A. 375–377 (2004) 213–218. https://doi.org/10.1016/j.msea.2003.10.257.

[3]   M.-H. Tsai, J.-W. Yeh, High-Entropy Alloys: A Critical Review, Mater. Res. Lett. 2 (2014) 107–123. https://doi.org/10.1080/21663831.2014.912690.

[4]   Y. Zhang, T.T. Zuo, Z. Tang, M.C. Gao, K.A. Dahmen, P.K. Liaw, Z.P. Lu, Microstructures and properties of high-entropy alloys, Prog. Mater. Sci. 61 (2014) 1–93. https://doi.org/10.1016/j.pmatsci.2013.10.001.

[5]   D.B. Miracle, O.N. Senkov, A critical review of high entropy alloys and related concepts, Acta Mater. 122 (2017) 448–511. https://doi.org/10.1016/j.actamat.2016.08.081.

[6]   E.P. George, D. Raabe, R.O. Ritchie, High-entropy alloys, Nat. Rev. Mater. 4 (2019) 515–534. https://doi.org/10.1038/s41578-019-0121-4.

[7]   E.P. George, W.A. Curtin, C.C. Tasan, High entropy alloys: A focused review of mechanical properties and deformation mechanisms, Acta Mater. 188 (2019) 435–474. https://doi.org/10.1016/j.actamat.2019.12.015.

[8]   B. Cantor, Multicomponent high-entropy Cantor alloys, Prog. Mater. Sci. (2020) 100754. https://doi.org/10.1016/j.pmatsci.2020.100754.

[9]   J. Yeh, M.C. Gao, P.K. Liaw, Y. Zhang, High-Entropy Alloys, Springer, 2016.

[10]   B.S. Murty, S. Ranganathan, J.W. Yeh, P.P. Bhattacharjee, High-Entropy Alloys, 2nd Editio, Elsevier, 2019. https://doi.org/10.1016/C2017-0-03317-7.

[11]   F. Otto, A. Dlouh, C. Somsen, H. Bei, G. Eggeler, E.P. George, The influences of temperature and microstructure on the tensile properties of a CoCrFeMnNi high-entropy alloy, Acta Mater. 61 (2013) 5743–5755. https://doi.org/10.1016/j.actamat.2013.06.018.

[12]   B. Gludovatz, A. Hohenwarter, D. Catoor, E.H. Chang, E.P. George, R.O. Ritchie,

A fracture-resistant high-entropy alloy for cryogenic applications, Science (80-.). 345 (2014) 1153–1158. https://doi.org/10.1126/science.1254581.

[13] C. Hsu, J. Yeh, S. Chen, T. Shun, Wear resistance and high-temperature compression strength of Fcc CuCoNiCrAl0.5Fe alloy with boron addition, Metall. Mater. Trans. A. 35 (2004) 1465–1469. https://doi.org/10.1007/s11661-004-0254-x.

[14] C. Zhang, F. Zhang, H. Diao, M.C. Gao, Z. Tang, J.D. Poplawsky, P.K. Liaw, Understanding phase stability of Al-Co-Cr-Fe-Ni high entropy alloys, Mater. Des. 109 (2016) 425–433. https://doi.org/10.1016/j.matdes.2016.07.073.

[15] S. Haas, M. Mosbacher, O. Senkov, M. Feuerbacher, J. Freudenberger, S. Gezgin, R. Völkl, U. Glatzel, Entropy Determination of Single-Phase High Entropy Alloys with Different Crystal Structures over a Wide Temperature Range, Entropy. 20 (2018) 654. https://doi.org/10.3390/e20090654.

[16] O.N. Senkov, J.D. Miller, D.B. Miracle, C. Woodward, Accelerated exploration of multi-principal element alloys for structural applications, Calphad Comput. Coupling Phase Diagrams Thermochem. 50 (2015) 32–48. https://doi.org/10.1016/j.calphad.2015.04.009.

[17] T. Abe, Thermal Vacancies in High-Entropy Alloys, Mater. Trans. 61 (2020) 610–615. https://doi.org/10.2320/matertrans.MT-MK2019008.

[18] K.Y. Tsai, M.H. Tsai, J.W. Yeh, Sluggish diffusion in Co-Cr-Fe-Mn-Ni high-entropy alloys, Acta Mater. 61 (2013) 4887–4897. https://doi.org/10.1016/j.actamat.2013.04.058.

[19] J. Dąbrowa, W. Kucza, G. Cieślak, T. Kulik, M. Danielewski, J.-W. Yeh, Interdiffusion in the FCC-structured Al-Co-Cr-Fe-Ni high entropy alloys: Experimental studies and numerical simulations, J. Alloys Compd. 674 (2016) 455–462. https://doi.org/10.1016/j.jallcom.2016.03.046.

[20] K. Sugita, N. Matsuoka, M. Mizuno, H. Araki, Vacancy formation enthalpy in CoCrFeMnNi high-entropy alloy, Scr. Mater. 176 (2020) 32–35. https://doi.org/10.1016/j.scriptamat.2019.09.033.

[21] K. Jin, C. Zhang, F. Zhang, H. Bei, Influence of compositional complexity on interdiffusion in Ni-containing concentrated solid-solution alloys, Mater. Res. Lett. 6 (2018) 293–299. https://doi.org/10.1080/21663831.2018.1446466.

[22] M. Mizuno, K. Sugita, H. Araki, Defect energetics for diffusion in CrMnFeCoNi high-entropy alloy from first-principles calculations, Comput. Mater. Sci. 170 (2019) 109163. https://doi.org/10.1016/j.commatsci.2019.109163.

[23] H. Oh, D. Ma, G. Leyson, B. Grabowski, E. Park, F. Körmann, D. Raabe, Lattice Distortions in the FeCoNiCrMn High Entropy Alloy Studied by Theory and Experiment, Entropy. 18 (2016) 321. https://doi.org/10.3390/e18090321.

[24] H.S. Oh, S.J. Kim, K. Odbadrakh, W.H. Ryu, K.N. Yoon, S. Mu, F. Körmann, Y. Ikeda, C.C. Tasan, D. Raabe, T. Egami, E.S. Park, Engineering atomic-level complexity in high-entropy and complex concentrated alloys, Nat. Commun. 10 (2019) 2090. https://doi.org/10.1038/s41467-019-10012-7.

[25] W. Sun, X. Huang, A.A. Luo, Phase formations in low density high entropy alloys, Calphad Comput. Coupling Phase Diagrams Thermochem. 56 (2017) 19–28. https://doi.org/10.1016/j.calphad.2016.11.002.

[26] I.S. Wani, T. Bhattacharjee, S. Sheikh, I.T. Clark, M.H. Park, T. Okawa, S. Guo, P.P. Bhattacharjee, N. Tsuji, Cold-rolling and recrystallization textures of a nano-lamellar AlCoCrFeNi2.1 eutectic high entropy alloy, Intermetallics. 84 (2017) 42–51. https://doi.org/10.1016/j.intermet.2016.12.018.

[27] Q. Tang, Y. Huang, H. Cheng, X. Liao, T.G. Langdon, P. Dai, The effect of grain size on the annealing-induced phase transformation in an Al0·3CoCrFeNi high entropy alloy, Mater. Des. 105 (2016) 381–385. https://doi.org/10.1016/j.matdes.2016.05.079.

[28] Z. Li, K.G. Pradeep, Y. Deng, D. Raabe, C.C. Tasan, Metastable high-entropy dual-phase alloys overcome the strength–ductility trade-off, Nature. 534 (2016) 227–230. https://doi.org/10.1038/nature17981.

[29] Z. Li, C.C. Tasan, K.G. Pradeep, D. Raabe, A TRIP-assisted dual-phase high-entropy alloy: Grain size and phase fraction effects on deformation behavior, Acta Mater. 131 (2017) 323–335. https://doi.org/10.1016/j.actamat.2017.03.069.

[30] Z. Li, F. Körmann, B. Grabowski, J. Neugebauer, D. Raabe, Ab initio assisted design of quinary dual-phase high-entropy alloys with transformation-induced plasticity, Acta Mater. 136 (2017) 262–270. https://doi.org/10.1016/j.actamat.2017.07.023.

[31] Z. Li, C.C. Tasan, H. Springer, B. Gault, D. Raabe, Interstitial atoms enable joint

twinning and transformation induced plasticity in strong and ductile high-entropy alloys, Sci. Rep. 7 (2017) 1–7. https://doi.org/10.1038/srep40704.

[32] Z. Wu, H. Bei, F. Otto, G.M.M. Pharr, E.P.P. George, Recovery, recrystallization, grain growth and phase stability of a family of FCC-structured multi-component equiatomic solid solution alloys, Intermetallics. 46 (2014) 131–140. https://doi.org/10.1016/j.intermet.2013.10.024.

[33] B. Gludovatz, A. Hohenwarter, K.V.S. Thurston, H. Bei, Z. Wu, E.P. George, R.O. Ritchie, Exceptional damage-tolerance of a medium-entropy alloy CrCoNi at cryogenic temperatures, Nat. Commun. 7 (2016) 10602. https://doi.org/10.1038/ncomms10602.

[34] G. Laplanche, A. Kostka, C. Reinhart, J. Hunfeld, G. Eggeler, E.P. George, Reasons for the superior mechanical properties of medium-entropy CrCoNi compared to high-entropy CrMnFeCoNi, Acta Mater. 128 (2017) 292–303. https://doi.org/10.1016/j.actamat.2017.02.036.

[35] J. Miao, C.E. Slone, T.M. Smith, C. Niu, H. Bei, M. Ghazisaeidi, G.M. Pharr, M.J. Mills, The evolution of the deformation substructure in a Ni-Co-Cr equiatomic solid solution alloy, Acta Mater. 132 (2017) 35–48. https://doi.org/10.1016/j.actamat.2017.04.033.

[36] F.G. Coury, K.D. Clarke, C.S. Kiminami, M.J. Kaufman, A.J. Clarke, High Throughput Discovery and Design of Strong Multicomponent Metallic Solid Solutions, Sci. Rep. 8 (2018) 1–10. https://doi.org/10.1038/s41598-018-26830-6.

[37] F.G. Coury, P. Wilson, K.D. Clarke, M.J. Kaufman, A.J. Clarke, High-throughput solid solution strengthening characterization in high entropy alloys, Acta Mater. 167 (2019) 1–11. https://doi.org/10.1016/j.actamat.2019.01.029.

[38] S. Yoshida, T. Ikeuchi, Y. Bai, N. Tsuji, Effect of cobalt-content on mechanical properties of non-equiatomic CoCrNi medium entropy alloys, Mater. Trans. 61 (2020) 587–595. https://doi.org/10.2320/matertrans.MT-MK2019004.

[39] Y.Y. Zhao, T.G. Nieh, Correlation between lattice distortion and friction stress in Ni-based equiatomic alloys, Intermetallics. 86 (2017) 45–50. https://doi.org/10.1016/j.intermet.2017.03.011.

[40] H. Chen, A. Kauffmann, S. Laube, I.C. Choi, R. Schwaiger, Y. Huang, K. Lichtenberg, F. Müller, B. Gorr, H.J. Christ, M. Heilmaier, Contribution of Lattice

Distortion to Solid Solution Strengthening in a Series of Refractory High Entropy Alloys, Metall. Mater. Trans. A Phys. Metall. Mater. Sci. (2017) 1–10. https://doi.org/10.1007/s11661-017-4386-1.

[41]   N.L. Okamoto, K. Yuge, K. Tanaka, H. Inui, E.P. George, Atomic displacement in the CrMnFeCoNi high-entropy alloy – A scaling factor to predict solid solution strengthening, AIP Adv. 6 (2016) 125008. https://doi.org/10.1063/1.4971371.

[42]   S. Yoshida, T. Bhattacharjee, Y. Bai, N. Tsuji, Friction stress and Hall-Petch relationship in CoCrNi equi-atomic medium entropy alloy processed by severe plastic deformation and subsequent annealing, Scr. Mater. 134 (2017) 33–36. https://doi.org/10.1016/j.scriptamat.2017.02.042.

[43]   R.. Fleischer, Substitutional solution hardening, Acta Metall. 11 (1963) 203–209. https://doi.org/10.1016/0001-6160(63)90213-X.

[44]   R.L. Fleischer, Solution hardening by tetragonal distortions: Application to irradiation hardening in F.C.C. crystals, Acta Metall. 10 (1962) 835–842. https://doi.org/10.1016/0001-6160(62)90098-6.

[45]   Labusch. R, A statistical theory of solid solution hardening, Phys. Status Solidi. 41 (1970) 659–669.

[46]   A.S. Argon, Strengthening mechanisms in crystal plasticity, Oxford University Press, Oxford, UK, 2008.

[47]   L.A. Gypen, A. Deruyttere, Multi-component solid solution hardening - Part 1 Proposed model, J. Mater. Sci. 12 (1977) 1028–1033. https://doi.org/10.1007/BF00540987.

[48]   Z. Wu, Y. Gao, H. Bei, Thermal activation mechanisms and Labusch-type strengthening analysis for a family of high-entropy and equiatomic solid-solution alloys, Acta Mater. 120 (2016) 108–119. https://doi.org/10.1016/j.actamat.2016.08.047.

[49]   H. Schreier, J.-J. Orteu, M.A. Sutton, Image Correlation for Shape, Motion and Deformation Measurements, Springer US, Boston, MA, 2009. https://doi.org/10.1007/978-0-387-78747-3.

[50]   T. Omori, J. Sato, K. Shinagawa, I. Ohnuma, K. Oikawa, R. Kainuma, K. Ishida, Experimental determination of phase equilibria in the Co-Cr-Ni system, J. Phase Equilibria Diffus. 35 (2014) 178–185. https://doi.org/10.1007/s11669-014-0292-z.

[51] E.O. Hall, The deformation and ageing of mild steel III Discussion of results, Proc. Phys. Soc. Sect. B. 64 (1951) 747. https://doi.org/10.1088/0370-1301/64/9/303.

[52] N.J. Petch, The Cleavage Strength of Polycrystals, J. Iron Steel Inst. 174 (1953) 25–28.

[53] N. Tsuji, Y. Ito, Y. Saito, Y. Minamino, Strength and ductility of ultrafine grained aluminum and iron produced by ARB and annealing, Scr. Mater. 47 (2002) 893–899. https://doi.org/10.1016/S1359-6462(02)00282-8.

[54] N. Tsuji, Unique Mechanical Properties of Nanostructured Metals, J.Nanosci.Nanotechnol. 7 (2007) 3765–3770. https://doi.org/10.1166/jnn.2007.025.

[55] R. Saha, R. Ueji, N. Tsuji, Fully recrystallized nanostructure fabricated without severe plastic deformation in high-Mn austenitic steel, Scr. Mater. 68 (2013) 813–816. https://doi.org/10.1016/j.scriptamat.2013.01.038.

[56] Y.Z. Tian, S. Gao, L.J. Zhao, S. Lu, R. Pippan, Z.F. Zhang, N. Tsuji, Remarkable transitions of yield behavior and Lüders deformation in pure Cu by changing grain sizes, Scr. Mater. 142 (2018) 88–91. https://doi.org/10.1016/j.scriptamat.2017.08.034.

[57] S. Gao, M. Chen, S. Chen, N. Kamikawa, A. Shibata, N. Tsuji, Yielding Behavior and Its Effect on Uniform Elongation of Fine Grained IF Steel, Mater. Trans. 55 (2014) 73–77. https://doi.org/10.2320/matertrans.MA201317.

[58] S. Khamsuk, N. Park, S. Gao, D. Terada, H. Adachi, N. Tsuji, Mechanical Properties of Bulk Ultrafine Grained Aluminum Fabricated by Torsion Deformation at Various Temperatures and Strain Rates, Mater. Trans. 55 (2014) 106–113. https://doi.org/DOI 10.2320/matertrans.MA201321.

[59] C. Keller, E. Hug, Hall–Petch behaviour of Ni polycrystals with a few grains per thickness, Mater. Lett. 62 (2008) 1718–1720. https://doi.org/10.1016/j.matlet.2007.09.069.

[60] Z. Wu, H. Bei, G.M. Pharr, E.P. George, Temperature dependence of the mechanical properties of equiatomic solid solution alloys with face-centered cubic crystal structures, Acta Mater. 81 (2014) 428–441. https://doi.org/10.1016/j.actamat.2014.08.026.

[61] T.M. Smith, M.S. Hooshmand, B.D. Esser, F. Otto, D.W. McComb, E.P. George,

M. Ghazisaeidi, M.J. Mills, Atomic-Scale Characterization and Modeling of 60° Dislocations in a High Entropy Alloy, Acta Mater. 110 (2016) 352–363. https://doi.org/10.1016/j.actamat.2016.03.045.

[62] Y. Zeng, X. Cai, M. Koslowski, Effects of the stacking fault energy fluctuations on the strengthening of alloys, Acta Mater. 164 (2019) 1–11. https://doi.org/10.1016/j.actamat.2018.09.066.

[63] C. Varvenne, A. Luque, W.A. Curtin, Theory of strengthening in fcc high entropy alloys, Acta Mater. 118 (2016) 164–176. https://doi.org/10.1016/j.actamat.2016.07.040.

[64] R. Labusch, Statistische theorien der mischkristallhärtung, Acta Metall. 20 (1972) 917–927. https://doi.org/10.1016/0001-6160(72)90085-5.

[65] R. Labusch, Cooperative effects in alloy hardening, Czech. J. Phys. B. 38 (1988) 474–481.

[66] M. Schneider, E.P. George, T.J. Manescau, T. Záležák, J. Hunfeld, A. Dlouhý, G. Eggeler, G. Laplanche, Analysis of strengthening due to grain boundaries and annealing twin boundaries in the CrCoNi medium-entropy alloy, Int. J. Plast. 124 (2020) 155–169. https://doi.org/10.1016/j.ijplas.2019.08.009.

[67] A. Haglund, M. Koehler, D. Catoor, E.P. George, V. Keppens, Polycrystalline elastic moduli of a high-entropy alloy at cryogenic temperatures, Intermetallics. 58 (2015) 62–64. https://doi.org/10.1016/j.intermet.2014.11.005.

[68] A.D. Rollett, G.S. Rohrer, F.J. Humphreys, Recrystallization and related annealing phenomena., 3rd Editio, Elsevier, 2017.

[69] I. Toda-Caraballo, J.S. Wrobel, S.L. Dudarev, D. Nguyen-Manh, P.E.J. Rivera-Diaz-Del-Castillo, Interatomic spacing distribution in multicomponent alloys, Acta Mater. 97 (2015) 156–169. https://doi.org/10.1016/j.actamat.2015.07.010.

[70] I. Toda-Caraballo, A general formulation for solid solution hardening effect in multicomponent alloys, Scr. Mater. 127 (2017) 113–117. https://doi.org/10.1016/j.scriptamat.2016.09.009.

[71] N. Greenwood, N, A. Earnshaw, Chemistry of the Elements, Second Edi, Elsevier, Oxford, UK, 1997.

[72] B. Yin, S. Yoshida, N. Tsuji, W.A. Curtin, Yield strength and misfit volumes of NiCoCr and implications for short-range-order, Nat. Commun. 11 (2020) 2507.

https://doi.org/10.1038/s41467-020-16083-1.

[73] M.Z. Butt, P. Feltham, Solid-solution hardening, J. Mater. Sci. 28 (1993) 2557–2576. https://doi.org/10.1007/BF00356192.

[74] M.Z. Butt, P. Feltham, I.M. Ghauri, On the temperature dependence of the flow stress of metals and solid solutions, J. Mater. Sci. 21 (1986) 2664–2666. https://doi.org/10.1007/BF00551470.

[75] O. Grässel, L. Krüger, G. Frommeyer, L.W. Meyer, High strength Fe-Mn-(Al, Si) TRIP/TWIP steels development - properties - application, Int. J. Plast. 16 (2000) 1391–1409. https://doi.org/10.1016/S0749-6419(00)00015-2.

[76] G.P.M. Leyson, W.A. Curtin, L.G. Hector, C.F. Woodward, Quantitative prediction of solute strengthening in aluminium alloys, Nat. Mater. 9 (2010) 750–755. https://doi.org/10.1038/nmat2813.

[77] G.P.M. Leyson, L.G. Hector, W.A. Curtin, Solute strengthening from first principles and application to aluminum alloys, Acta Mater. 60 (2012) 3873–3884. https://doi.org/10.1016/j.actamat.2012.03.037.

[78] B. Yin, W.A. Curtin, First-principles-based prediction of yield strength in the RhIrPdPtNiCu high-entropy alloy, Npj Comput. Mater. 5 (2019). https://doi.org/10.1038/s41524-019-0151-x.

[79] B. Yin, F. Maresca, W.A. Curtin, Vanadium is an optimal element for strengthening in both fcc and bcc high-entropy alloys, Acta Mater. 188 (2020) 486–491. https://doi.org/10.1016/j.actamat.2020.01.062.

[80] C. Varvenne, G.P.M. Leyson, M. Ghazisaeidi, W.A. Curtin, Solute strengthening in random alloys, Acta Mater. 124 (2017) 660–683. https://doi.org/10.1016/j.actamat.2016.09.046.

[81] C.R. LaRosa, M. Shih, C. Varvenne, M. Ghazisaeidi, Solid solution strengthening theories of high-entropy alloys, Mater. Charact. 151 (2019) 310–317. https://doi.org/10.1016/j.matchar.2019.02.034.

[82] C. Varvenne, W.A. Curtin, Predicting yield strengths of noble metal high entropy alloys, Scr. Mater. 142 (2018) 92–95. https://doi.org/10.1016/j.scriptamat.2017.08.030.

[83] C. Varvenne, W.A. Curtin, Strengthening of high entropy alloys by dilute solute additions: CoCrFeNiAlx and CoCrFeNiMnAlx alloys, Scr. Mater. 138 (2017) 92–

95. https://doi.org/10.1016/j.scriptamat.2017.05.035.

[84]   G. Laplanche, J. Bonneville, C. Varvenne, W.A. Curtin, E.P. George, Thermal activation parameters of plastic flow reveal deformation mechanisms in the CrMnFeCoNi high-entropy alloy, Acta Mater. 143 (2018) 257–264. https://doi.org/10.1016/j.actamat.2017.10.014.

[85]   M.P. Agustianingrum, S. Yoshida, N. Tsuji, N. Park, Effect of aluminum addition on solid solution strengthening in CoCrNi medium-entropy alloy, J. Alloys Compd. 781 (2019) 866–872. https://doi.org/10.1016/j.jallcom.2018.12.065.

[86]   F. Maresca, W.A. Curtin, Mechanistic origin of high strength in refractory BCC high entropy alloys up to 1900K, Acta Mater. 182 (2020) 235–249. https://doi.org/10.1016/j.actamat.2019.10.015.

[87]   F. Maresca, W.A. Curtin, Theory of screw dislocation strengthening in random BCC alloys from dilute to "High-Entropy" alloys, Acta Mater. 182 (2020) 144–162. https://doi.org/10.1016/j.actamat.2019.10.007.

[88]   W. Georg, W.A. Curtin, Correlation of microdistortions with misfit volumes in High Entropy Alloys, Scr. Mater. 168 (2019) 119–123. https://doi.org/10.1016/j.scriptamat.2019.04.012.

[89]   D. Wen, C.-H. Chang, S. Matsunaga, G. Park, L. Ecker, S.K. Gill, M. Topsakal, M.A. Okuniewski, S. Antonov, D.R. Johnson, M.S. Titus, Structure and tensile properties of Mx(MnFeCoNi)100-x solid solution strengthened high entropy alloys, Materialia. 9 (2020) 100539. https://doi.org/10.1016/j.mtla.2019.100539.

[90]   S.S. Sohn, A. Kwiatkowski da Silva, Y. Ikeda, F. Körmann, W. Lu, W.S. Choi, B. Gault, D. Ponge, J. Neugebauer, D. Raabe, Ultrastrong Medium-Entropy Single-Phase Alloys Designed via Severe Lattice Distortion, Adv. Mater. 31 (2019) 1807142. https://doi.org/10.1002/adma.201807142.

[91]   F.X. Zhang, S. Zhao, K. Jin, H. Xue, G. Velisa, H. Bei, R. Huang, J.Y.P. Ko, D.C. Pagan, J.C. Neuefeind, W.J. Weber, Y. Zhang, Local Structure and Short-Range Order in a NiCoCr Solid Solution Alloy, Phys. Rev. Lett. 118 (2017) 1–6. https://doi.org/10.1103/PhysRevLett.118.205501.

[92]   Q.J. Li, H. Sheng, E. Ma, Strengthening in multi-principal element alloys with local-chemical-order roughened dislocation pathways, Nat. Commun. 10 (2019) 1–11. https://doi.org/10.1038/s41467-019-11464-7.

[93] R. Zhang, S. Zhao, J. Ding, Y. Chong, T. Jia, C. Ophus, M. Asta, R.O. Ritchie, A.M. Minor, Short-range order and its impact on the CrCoNi medium-entropy alloy, Nature. 581 (2020) 283–287. https://doi.org/10.1038/s41586-020-2275-z.

[94] E. Antillon, C. Woodward, S.I. Rao, B. Akdim, T.A. Parthasarathy, Chemical short range order strengthening in a model FCC high entropy alloy, Acta Mater. 190 (2020) 29–42. https://doi.org/10.1016/j.actamat.2020.02.041.

[95] E. Ma, Unusual dislocation behavior in high-entropy alloys, Scr. Mater. 181 (2020) 127–133. https://doi.org/10.1016/j.scriptamat.2020.02.021.

[96] I. Basu, J.T.M. De Hosson, Strengthening mechanisms in high entropy alloys: Fundamental issues, Scr. Mater. 187 (2020) 148–156. https://doi.org/10.1016/j.scriptamat.2020.06.019.

[97] F. Thiel, D. Utt, A. Kauffmann, K. Nielsch, K. Albe, M. Heilmaier, J. Freudenberger, Breakdown of Varvenne scaling in (AuNiPdPt) 1 − x Cu x high-entropy alloys, Scr. Mater. 181 (2020) 15–18. https://doi.org/10.1016/j.scriptamat.2020.02.007.

[98] Z. Pei, R. Li, M.C. Gao, G.M. Stocks, Statistics of the NiCoCr medium-entropy alloy: Novel aspects of an old puzzle, Npj Comput. Mater. 6 (2020) 122. https://doi.org/10.1038/s41524-020-00389-1.

[99] Y. Zhang, S. Zhao, W.J. Weber, K. Nordlund, F. Granberg, F. Djurabekova, Atomic-level heterogeneity and defect dynamics in concentrated solid-solution alloys, Curr. Opin. Solid State Mater. Sci. 21 (2017) 221–237. https://doi.org/10.1016/j.cossms.2017.02.002.

[100] J. Ding, Q. Yu, M. Asta, R.O. Ritchie, Tunable stacking fault energies by tailoring local chemical order in CrCoNi medium-entropy alloys, Proc. Natl. Acad. Sci. U. S. A. 115 (2018) 8919–8924. https://doi.org/10.1073/pnas.1808660115.

[101] Y. Wu, F. Zhang, X. Yuan, H. Huang, X. Wen, Y. Wang, M. Zhang, H. Wu, X. Liu, H. Wang, S. Jiang, Z. Lu, Short-range ordering and its effects on mechanical properties of high-entropy alloys, J. Mater. Sci. Technol. 62 (2021) 214–220. https://doi.org/10.1016/j.jmst.2020.06.018.

[102] D. Zhou, Z. Chen, K. Ehara, K. Nitsu, K. Tanaka, H. Inui, Effects of annealing on hardness, yield strength and dislocation structure in single crystals of the equiatomic Cr-Mn-Fe-Co-Ni high entropy alloy, Scr. Mater. 191 (2021) 173–178.

https://doi.org/10.1016/j.scriptamat.2020.09.039.

[103] W.G. Nöhring, W.A. Curtin, Cross-slip of long dislocations in FCC solid solutions, Acta Mater. 158 (2018) 95–117. https://doi.org/10.1016/j.actamat.2018.05.027.

[104] W.G. Nöhring, W.A. Curtin, Dislocation cross-slip in fcc solid solution alloys, Acta Mater. 128 (2017) 135–148. https://doi.org/10.1016/j.actamat.2017.02.027.

[105] C.C. Wang, C.H. Wong, Short-to-medium range order of Al-Mg metallic glasses studied by molecular dynamics simulations, J. Alloys Compd. 509 (2011) 10222–10229. https://doi.org/10.1016/j.jallcom.2011.08.075.

[106] S. Nag, W.A. Curtin, Effect of solute-solute interactions on strengthening of random alloys from dilute to high entropy alloys, Acta Mater. 200 (2020) 659–673. https://doi.org/10.1016/j.actamat.2020.08.011.

[107] X. Huang, N. Hansen, Grain orientation dependence of microstructure in aluminium deformed in tension, Scr. Mater. 37 (1997) 1–7. https://doi.org/10.1016/S1359-6462(97)00072-9.

[108] X. Huang, Grain orientation effect on microstructure in tensile strained copper, Scr. Mater. 38 (1998) 1697–1703. https://doi.org/10.1016/S1359-6462(98)00051-7.

[109] X. Huang, G. Winther, Dislocation structures. Part I. Grain orientation dependence, Philos. Mag. 87 (2007) 5189–5214. https://doi.org/10.1080/14786430701652851.

[110] N. Hansen, R.F. Mehl, New discoveries in deformed metals, Metall. Mater. Trans. A Phys. Metall. Mater. Sci. 32 (2001) 2917–2935. https://doi.org/10.1007/s11661-001-0167-x.

[111] N. Hansen, X. Huang, W. Pantleon, G. Winther, Grain orientation and dislocation patterns, Philos. Mag. 86 (2006) 3981–3994. https://doi.org/10.1080/14786430600654446.

[112] G. Winther, X. Huang, Dislocation structures. Part II. Slip system dependence, Philos. Mag. 87 (2007) 5215–5235. https://doi.org/10.1080/14786430701591505.

[113] G.M. Le, A. Godfrey, N. Hansen, W. Liu, G. Winther, X. Huang, Influence of grain size in the near-micrometre regime on the deformation microstructure in aluminium, Acta Mater. 61 (2013) 7072–7086. https://doi.org/10.1016/j.actamat.2013.07.046.

[114] D.A. Hughes, N. Hansen, The microstructural origin of work hardening stages, Acta Mater. 148 (2018) 374–383. https://doi.org/10.1016/j.actamat.2018.02.002.

[115] I. Gutierrez-Urrutia, D. Raabe, Grain size effect on strain hardening in twinning-induced plasticity steels, Scr. Mater. 66 (2012) 992–996. https://doi.org/10.1016/j.scriptamat.2012.01.037.

[116] I. Gutierrez-Urrutia, D. Raabe, Multistage strain hardening through dislocation substructure and twinning in a high strength and ductile weight-reduced Fe–Mn–Al–C steel, Acta Mater. 60 (2012) 5791–5802. https://doi.org/10.1016/j.actamat.2012.07.018.

[117] I. Karaman, H. Sehitoglu, K. Gall, Y.I. Chumlyakov, On the deformation mechanisms in single crystal hadfield manganese steels, Scr. Mater. 38 (1998) 1009–1015. https://doi.org/10.1016/S1359-6462(97)00581-2.

[118] I. Karaman, H. Sehitoglu, K. Gall, Y.I. Chumlyakov, H.J. Maier, Deformation of single crystal hadfield steel by twinning and slip, Acta Mater. 48 (2000) 1345–1359. https://doi.org/10.1016/S1359-6454(99)00383-3.

[119] E.G. Zakharova, I. V. Kireeva, Y.I. Chumlyakov, S.P. Efimenko, H. Sehitoglu, I. Karaman, Deformation mechanisms and strain hardening of Hadfield-steel single crystals alloyed with aluminum, Dokl. Phys. 47 (2002) 515–517. https://doi.org/10.1134/1.1499189.

[120] D. Canadinc, I. Karaman, H. Sehitoglu, Y.I. Chumlyakov, H.J. Maier, The role of nitrogen on the deformation response of hadfield steel single crystals, Metall. Mater. Trans. A Phys. Metall. Mater. Sci. 34 A (2003) 1821–1831. https://doi.org/10.1007/s11661-003-0148-3.

[121] P. Müllner, C. Solenthaler, P. Uggowitzer, M.O.O. Speidel, On the effect of nitrogen on the dislocation structure of austenitic stainless steel, Elsevier, 1993.

[122] Y.I. Chumlyakov, I. V. Kireeva, A.D. Korotaev, E.I. Litvinova, Y.L. Zuev, Mechanisms of plastic deformation, hardening, and fracture in single crystals of nitrogen-containing austenitic stainless steels, Russ. Phys. J. 39 (1996) 189–210. https://doi.org/10.1007/BF02067642.

[123] I. Karaman, H. Sehitoglu, H.J. Maier, Y.I. Chumlyakov, Competing mechanisms and modeling of deformation in austenitic stainless steel single crystals with and without nitrogen, Acta Mater. 49 (2001) 3919–3933. https://doi.org/10.1016/S1359-6454(01)00296-8.

[124] I. Karaman, H. Sehitoglu, Y.I. Chumlyakov, H.J. Maier, The deformation of low-

stacking-fault-energy austenitic steels, JOM. 54 (2002) 31–37. https://doi.org/10.1007/BF02700983.

[125] R. Ueji, N. Tsuchida, D. Terada, N. Tsuji, Y. Tanaka, A. Takemura, K. Kunishige, Tensile properties and twinning behavior of high manganese austenitic steel with fine-grained structure, Scr. Mater. 59 (2008) 963–966. https://doi.org/10.1016/j.scriptamat.2008.06.050.

[126] G. Laplanche, A. Kostka, O.M. Horst, G. Eggeler, E.P. George, Microstructure evolution and critical stress for twinning in the CrMnFeCoNi high-entropy alloy, Acta Mater. 118 (2016) 152–163. https://doi.org/10.1016/j.actamat.2016.07.038.

[127] I. V. Kireeva, Y.I. Chumlyakov, Z. V. Pobedennaya, Y.N. Platonova, I. V. Kuksgauzen, D.A. Kuksgauzen, V. V. Poklonov, I. Karaman, H. Sehitoglu, Slip and Twinning in the [1⁻ 49]-Oriented Single Crystals of a High-Entropy Alloy, Russ. Phys. J. 59 (2016) 1242–1250. https://doi.org/10.1007/s11182-016-0898-1.

[128] W. Abuzaid, H. Sehitoglu, Critical resolved shear stress for slip and twin nucleation in single crystalline FeNiCoCrMn high entropy alloy, Mater. Charact. 129 (2017) 288–299. https://doi.org/10.1016/j.matchar.2017.05.014.

[129] I. V. Kireeva, Y.I. Chumlyakov, Z. V. Pobedennaya, I. V. Kuksgausen, I. Karaman, Orientation dependence of twinning in single crystalline CoCrFeMnNi high-entropy alloy, Mater. Sci. Eng. A. 705 (2017) 176–181. https://doi.org/10.1016/j.msea.2017.08.065.

[130] I. V. Kireeva, Y.I. Chumlyakov, Z. V. Pobedennaya, A. V. Vyrodova, I. Karaman, Twinning in [001]-oriented single crystals of CoCrFeMnNi high-entropy alloy at tensile deformation, Mater. Sci. Eng. A. 713 (2018) 253–259. https://doi.org/10.1016/j.msea.2017.12.059.

[131] I. V. Kireeva, Y.I. Chumlyakov, Z. V. Pobedennaya, A. V. Vyrodova, I. V. Kuksgauzen, D.A. Kuksgauzen, Orientation and temperature dependence of a planar slip and twinning in single crystals of Al0.3CoCrFeNi high-entropy alloy, Mater. Sci. Eng. A. 737 (2018) 47–60. https://doi.org/10.1016/j.msea.2018.09.025.

[132] M. Bönisch, Y. Wu, H. Sehitoglu, Hardening by slip-twin and twin-twin interactions in FeMnNiCoCr, Acta Mater. 153 (2018) 391–403. https://doi.org/10.1016/j.actamat.2018.04.054.

[133] B. Uzer, S. Picak, J. Liu, T. Jozaghi, D. Canadinc, I. Karaman, Y.I.I. Chumlyakov,

I. Kireeva, On the mechanical response and microstructure evolution of NiCoCr single crystalline medium entropy alloys, Mater. Res. Lett. 6 (2018) 442–449. https://doi.org/10.1080/21663831.2018.1478331.

[134] I. V. Kireeva, Y.I. Chumlyakov, A. V. Vyrodova, Z. V. Pobedennaya, I. Karaman, Effect of twinning on the orientation dependence of mechanical behaviour and fracture in single crystals of the equiatomic CoCrFeMnNi high-entropy alloy at 77K, Mater. Sci. Eng. A. 784 (2020) 139315. https://doi.org/10.1016/j.msea.2020.139315.

[135] W. Abuzaid, L. Patriarca, A study on slip activation for a coarse-grained and single crystalline CoCrNi medium entropy alloy, Intermetallics. 117 (2020) 106682. https://doi.org/10.1016/j.intermet.2019.106682.

[136] B.C. De Cooman, Y. Estrin, S.K. Kim, Twinning-induced plasticity (TWIP) steels, Acta Mater. 142 (2018) 283–362. https://doi.org/10.1016/j.actamat.2017.06.046.

[137] V. Gerold, H.P. Karnthaler, On the origin of planar slip in f.c.c. alloys, Acta Metall. 37 (1989) 2177–2183. https://doi.org/10.1016/0001-6160(89)90143-0.

[138] S. Yoshida, T. Ikeuchi, T. Bhattacharjee, Y. Bai, A. Shibata, N. Tsuji, Effect of elemental combination on friction stress and Hall-Petch relationship in face-centered cubic high / medium entropy alloys, Acta Mater. 171 (2019) 201–215. https://doi.org/10.1016/j.actamat.2019.04.017.

[139] S.J. Sun, Y.Z. Tian, H.R. Lin, X.G. Dong, Y.H. Wang, Z.J. Wang, Z.F. Zhang, Temperature dependence of the Hall–Petch relationship in CoCrFeMnNi high-entropy alloy, J. Alloys Compd. 806 (2019) 992–998. https://doi.org/10.1016/j.jallcom.2019.07.357.

[140] B.E.P.P. Beeston, I.L. Dillamore, R.E. Smallman, The Stacking-Fault Energy of Some Nickel-Cobalt Alloys, Met. Sci. J. 2 (1968) 12–14. https://doi.org/10.1179/030634568790443468.

[141] E.H. Köster, A.R. Thölén, A. Howie, Stacking fault energies of Ni–Co–Cr alloys, Philos. Mag. 10 (1964) 1093–1095. https://doi.org/10.1080/14786436408225417.

[142] S. Yoshida, T. Ikeuchi, Y. Bai, A. Shibata, N. Hansen, X. Huang, N. Tsuji, Deformation microstructures and strength of face-centered cubic high/medium entropy alloys, IOP Conf. Ser. Mater. Sci. Eng. 580 (2019) 012053.

[143] H. Schreier, J.J. Orteu, M.A. Sutton, Image correlation for shape, motion and

deformation measurements: Basic concepts, theory and applications, Springer US, Boston, 2009. https://doi.org/10.1007/978-0-387-78747-3.

[144] P.J. Phillips, M.J. Mills, M. De Graef, Systematic row and zone axis STEM defect image simulations, Philos. Mag. 91 (2011) 2081–2101. https://doi.org/10.1080/14786435.2010.547526.

[145] P.J. Phillips, M.C. Brandes, M.J. Mills, M. de Graef, Diffraction contrast STEM of dislocations: Imaging and simulations, Ultramicroscopy. 111 (2011) 1483–1487. https://doi.org/10.1016/j.ultramic.2011.07.001.

[146] Y. Zhu, C. Ophus, M.B. Toloczko, D.J. Edwards, Towards bend-contour-free dislocation imaging via diffraction contrast STEM, Ultramicroscopy. 193 (2018) 12–23. https://doi.org/10.1016/j.ultramic.2018.06.001.

[147] Q. Liu, A simple and rapid method for determining orientations and misorientations of crystalline specimens in TEM, Ultramicroscopy. 60 (1995) 81–89. https://doi.org/10.1016/0304-3991(95)00049-7.

[148] S. Zaefferer, New developments of computer-aided crystallographic analysis in transmission electron microscopy, J. Appl. Crystallogr. 33 (2000) 10–25. https://doi.org/10.1107/S0021889899010894.

[149] J.S. Barnard, J. Sharp, J.R. Tong, P.A. Midgley, High-resolution three-dimensional imaging of dislocations, Science (80-.). 313 (2006) 319. https://doi.org/10.1126/science.1125783.

[150] G.S. Liu, S.D. House, J. Kacher, M. Tanaka, K. Higashida, I.M. Robertson, Electron tomography of dislocation structures, Mater. Charact. 87 (2014) 1–11. https://doi.org/10.1016/j.matchar.2013.09.016.

[151] Z. Feng, R. Fu, C. Lin, G. Wu, T. Huang, L. Zhang, X. Huang, TEM-based dislocation tomography: Challenges and opportunities, Curr. Opin. Solid State Mater. Sci. (2020) 100833. https://doi.org/10.1016/j.cossms.2020.100833.

[152] S. Hata, T. Honda, H. Saito, M. Mitsuhara, T.C. Petersen, M. Murayama, Electron tomography: An imaging method for materials deformation dynamics, Curr. Opin. Solid State Mater. Sci. (2020) 100850. https://doi.org/10.1016/j.cossms.2020.100850.

[153] M. Radermacher, Weighted Back-Projection Methods, in: Electron Tomogr., Springer US, 1992: pp. 91–115. https://doi.org/10.1007/978-1-4757-2163-8_5.

[154] G. Ribárik, Modeling of diffraction patterns based on microstructural properties, Eötvös University Budapest, 2008.

[155] A. Heczel, M. Kawasaki, J.L. Lábár, J. il Jang, T.G. Langdon, J. Gubicza, Defect structure and hardness in nanocrystalline CoCrFeMnNi High-Entropy Alloy processed by High-Pressure Torsion, J. Alloys Compd. 711 (2017) 143–154. https://doi.org/10.1016/j.jallcom.2017.03.352.

[156] H.J. Leamy, H. Warlimont, The Elastic Behaviour of Ni-Co Alloys, Phys. Status Solidi. 37 (1970) 523–534. https://doi.org/10.1002/pssb.19700370203.

[157] D.J.H. Cockayne, A Theoretical Analysis of the Weak-beam Method of Electron Microscopy, Zeitschrift Fur Naturforsch. - Sect. A J. Phys. Sci. 27 (1972) 452–460. https://doi.org/10.1515/zna-1972-0313.

[158] E.B. Tadmor, N. Bernstein, A first-principles measure for the twinnability of FCC metals, J. Mech. Phys. Solids. 52 (2004) 2507–2519. https://doi.org/10.1016/j.jmps.2004.05.002.

[159] L.Y. Tian, R. Lizárraga, H. Larsson, E. Holmström, L. Vitos, A first principles study of the stacking fault energies for fcc Co-based binary alloys, Acta Mater. 136 (2017) 215–223. https://doi.org/10.1016/j.actamat.2017.07.010.

[160] S. Zhao, G.M. Stocks, Y. Zhang, Stacking fault energies of face-centered cubic concentrated solid solution alloys, Acta Mater. 134 (2017) 334–345. https://doi.org/10.1016/j.actamat.2017.05.001.

[161] C. Niu, C.R. LaRosa, J. Miao, M.J. Mills, M. Ghazisaeidi, Magnetically-driven phase transformation strengthening in high entropy alloys, Nat. Commun. 9 (2018) 1–9. https://doi.org/10.1038/s41467-018-03846-0.

[162] S. Huang, H. Huang, W. Li, D. Kim, S. Lu, X. Li, E. Holmström, S.K. Kwon, L. Vitos, Twinning in metastable high-entropy alloys, Nat. Commun. 9 (2018) 2381. https://doi.org/10.1038/s41467-018-04780-x.

[163] M. Considère, L'emploi du fer de l'acier dans les constructions, Memoire no 34, Ann. Des Ponts Chaussées. 9 (1885) 574–775.

[164] D.B. Williams, C.B. Carter, Transmission electron microscopy: A textbook for materials science, Springer US, 2009. https://doi.org/10.1007/978-0-387-76501-3.

[165] P.M. Anderson, J.P. Hirth, J. Lothe, Theory of dislocations, 3rd editio, Cambridge University Press, 2017.

https://www.cambridge.org/jp/academic/subjects/engineering/materials-science/theory-dislocations-3rd-edition?format=HB&isbn=9780521864367.

[166] M. Ojima, Y. Adachi, Y. Tomota, K. Ikeda, T. Kamiyama, Y. Katada, Work hardening mechanism in high nitrogen austenitic steel studied by in situ neutron diffraction and in situ electron backscattering diffraction, Mater. Sci. Eng. A. 527 (2009) 16–24. https://doi.org/10.1016/j.msea.2009.07.066.

[167] Y. Wang, B. Liu, K. Yan, M. Wang, S. Kabra, Y.L. Chiu, D. Dye, P.D. Lee, Y. Liu, B. Cai, Probing deformation mechanisms of a FeCoCrNi high-entropy alloy at 293 and 77 K using in situ neutron diffraction, Acta Mater. 154 (2018) 79–89. https://doi.org/10.1016/j.actamat.2018.05.013.

[168] A.A. Saleh, E. V. Pereloma, B. Clausen, D.W. Brown, C.N. Tomé, A.A. Gazder, Self-consistent modelling of lattice strains during the in-situ tensile loading of twinning induced plasticity steel, Mater. Sci. Eng. A. 589 (2014) 66–75. https://doi.org/10.1016/j.msea.2013.09.073.

[169] B. Cai, B. Liu, S. Kabra, Y. Wang, K. Yan, P.D. Lee, Y. Liu, Deformation mechanisms of Mo alloyed FeCoCrNi high entropy alloy: In situ neutron diffraction, Acta Mater. 127 (2017) 471–480. https://doi.org/10.1016/j.actamat.2017.01.034.

[170] J.S. Jeong, W. Woo, K.H. Oh, S.K. Kwon, Y.M. Koo, In situ neutron diffraction study of the microstructure and tensile deformation behavior in Al-added high manganese austenitic steels, Acta Mater. 60 (2012) 2290–2299. https://doi.org/10.1016/j.actamat.2011.12.043.

[171] S.M. Copley, B.H. Kear, The dependence of the width of a dissociated dislocation on dislocation velocity, Acta Metall. 16 (1968) 227–231. https://doi.org/10.1016/0001-6160(68)90118-1.

[172] B.S. Lee, Y. Koizumi, H. Matsumoto, A. Chiba, Collective behavior of strain-induced martensitic transformation (SIMT) in biomedical Co-Cr-Mo-N alloy polycrystal: An ex-situ electron backscattering diffraction study, Mater. Sci. Eng. A. 611 (2014) 263–273. https://doi.org/10.1016/j.msea.2014.05.071.

[173] S.I. Rao, C. Woodward, T.A. Parthasarathy, O. Senkov, Atomistic simulations of dislocation behavior in a model FCC multicomponent concentrated solid solution alloy, Acta Mater. 134 (2017) 188–194.

https://doi.org/10.1016/j.actamat.2017.05.071.

[174] S.I. Hong, C. Laird, Mechanisms of slip mode modification in F.C.C. solid solutions, Acta Metall. Mater. 38 (1990) 1581–1594. https://doi.org/10.1016/0956-7151(90)90126-2.

[175] S.I. Hong, Criteria for predicting twin-induced plasticity in solid solution copper alloys, Mater. Sci. Eng. A. 711 (2018) 492–497. https://doi.org/10.1016/j.msea.2017.11.076.

[176] J.W. Christian, S. Mahajan, Deformation twinning, Prog. Mater. Sci. 39 (1995) 1–157. https://doi.org/10.1016/0079-6425(94)00007-7.

[177] J.-S. Hong, S. Kang, J.-G. Jung, Y.-K. Lee, The mechanism of mechanical twinning near grain boundaries in twinning-induced plasticity steel, Scr. Mater. 174 (2020) 62–67. https://doi.org/10.1016/j.scriptamat.2019.08.025.

[178] S. Miura, J. Takamura, N. Narita, Orientation dependence of the flow stress for twinning in silver crystals, Trans. JIM. 9 (1968) 555.

[179] N. Narita, J. Takamura, Deformation twinning in f.c.c. and b.c.c. metals, in: F.R.N. Nabarro (Ed.), Dislocations Solids, Vol. 9, 1992: pp. 135–189.

[180] N. Narita, J. Takamura, Deformation twinning in silver- and copper-alloy crystals, Philos. Mag. 29 (1974) 1001–1028. https://doi.org/10.1080/14786437408226586.

[181] S.J. Sun, Y.Z. Tian, H.R. Lin, X.G. Dong, Y.H. Wang, Z.J. Zhang, Z.F. Zhang, Enhanced strength and ductility of bulk CoCrFeMnNi high entropy alloy having fully recrystallized ultrafine-grained structure, Mater. Des. 133 (2017) 122–127. https://doi.org/10.1016/j.matdes.2017.07.054.

[182] P.P. Bhattacharjee, G.D. Sathiaraj, M. Zaid, J.R. Gatti, C. Lee, C.W. Tsai, J.W. Yeh, Microstructure and texture evolution during annealing of equiatomic CoCrFeMnNi high-entropy alloy, J. Alloys Compd. 587 (2014) 544–552. https://doi.org/10.1016/j.jallcom.2013.10.237.

[183] G.D. Sathiaraj, P.P. Bhattacharjee, Analysis of microstructure and microtexture during grain growth in low stacking fault energy equiatomic CoCrFeMnNi high entropy and Ni-60 wt.%Co alloys, J. Alloys Compd. 637 (2015) 267–276. https://doi.org/10.1016/j.jallcom.2015.02.184.

[184] G.D. Sathiaraj, P.P. Bhattacharjee, Materials Characterization Effect of cold-rolling strain on the evolution of annealing texture of equiatomic CoCrFeMnNi

high entropy alloy, Mater. Charact. 109 (2015) 189–197. https://doi.org/10.1016/j.matchar.2015.09.027.

[185] G.D. Sathiaraj, M.Z. Ahmed, P.P. Bhattacharjee, Microstructure and texture of heavily cold-rolled and annealed fcc equiatomic medium to high entropy alloys, J. Alloys Compd. 664 (2016) 109–119. https://doi.org/10.1016/j.jallcom.2015.12.172.

[186] A. Azushima, R. Kopp, A. Korhonen, D.Y. Yang, F. Micari, G.D. Lahoti, P. Groche, J. Yanagimoto, N. Tsuji, A. Rosochowski, A. Yanagida, Severe plastic deformation (SPD) processes for metals, CIRP Ann. - Manuf. Technol. 57 (2008) 716–735. https://doi.org/10.1016/j.cirp.2008.09.005.

[187] R.Z. Valiev, N.A. Krasilnikov, N.K. Tsenev, Plastic deformation of alloys with submicron-grained structure, Mater. Sci. Eng. A. 137 (1991) 35–40. https://doi.org/10.1016/0921-5093(91)90316-F.

[188] O. Renk, R. Pippan, Saturation of Grain Refinement during Severe Plastic Deformation of Single Phase Materials: Reconsiderations, Current Status and Open Questions, Mater. Trans. 60 (2019) 1270–1282. https://doi.org/10.2320/matertrans.MF201918.

[189] K. Edalati, D. Akama, A. Nishio, S. Lee, Y. Yonenaga, J.M. Cubero-Sesin, Z. Horita, Influence of dislocation–solute atom interactions and stacking fault energy on grain size of single-phase alloys after severe plastic deformation using high-pressure torsion, Acta Mater. 69 (2014) 68–77. https://doi.org/10.1016/j.actamat.2014.01.036.

[190] W. Skrotzki, A. Pukenas, E. Odor, B. Joni, T. Ungar, B. Völker, A. Hohenwarter, R. Pippan, E.P. George, Microstructure, texture, and strength development during high-pressure torsion of crmnfeconi high-entropy alloy, Crystals. 10 (2020). https://doi.org/10.3390/cryst10040336.

[191] Koike J., Parkin D.M., N. M., Crystall-to-amorphous transformation of NiTi induced by cold rolling, J. Mater. Res. 5 (1990) 1414–1418.

[192] N.L. Okamoto, S. Fujimoto, Y. Kambara, M. Kawamura, Z.M.T. Chen, H. Matsunoshita, K. Tanaka, H. Inui, E.P. George, Size effect, critical resolved shear stress, stacking fault energy, and solid solution strengthening in the CrMnFeCoNi high-entropy alloy, Sci. Rep. 6 (2016) 35863. https://doi.org/10.1038/srep35863.

[193] F. Otto, A. Dlouhý, K.G. Pradeep, M. Kuběnová, D. Raabe, G. Eggeler, E.P. George, Decomposition of the single-phase high-entropy alloy CrMnFeCoNi after prolonged anneals at intermediate temperatures, Acta Mater. 112 (2016) 40–52. https://doi.org/10.1016/j.actamat.2016.04.005.

[194] F. Montheillet, M. Cohen, J.J. Jonas, Axial stresses and texture development during the torsion testing of Al, Cu and α-Fe, Acta Metall. 32 (1984) 2077–2089. https://doi.org/10.1016/0001-6160(84)90187-1.

[195] Z.R. Zeng, Y.M. Zhu, S.W. Xu, M.Z. Bian, C.H.J. Davies, N. Birbilis, J.F. Nie, Texture evolution during static recrystallization of cold-rolled magnesium alloys, Acta Mater. 105 (2016) 479–494. https://doi.org/10.1016/j.actamat.2015.12.045.

[196] N. Kamikawa, X. Huang, N. Tsuji, N. Hansen, Strengthening mechanisms in nanostructured high-purity aluminium deformed to high strain and annealed, Acta Mater. 57 (2009) 4198–4208. https://doi.org/10.1016/j.actamat.2009.05.017.

[197] X. Huang, N. Hansen, N. Tsuji, Hardening by Annealing and Softening by Deformation in Nanostructured Metals, Science (80-.). 312 (2006) 249–251. https://doi.org/10.1126/science.1124268.

[198] M.C. Iordache, S.H. Whang, Z. Jiao, Z.M. Wang, Grain growth kinetics in nanostructured nickel, Nanostructured Mater. 11 (1999) 1343–1349. https://doi.org/10.1016/S0965-9773(00)00427-X.

[199] W.H. Liu, Y. Wu, J.Y. He, T.G. Nieh, Z.P. Lu, Grain growth and the Hall–Petch relationship in a high-entropy FeCrNiCoMn alloy, Scr. Mater. 68 (2013) 526–529. https://doi.org/10.1016/j.scriptamat.2012.12.002.

[200] Y.-C. Huang, C.-H. Su, S.-K. Wu, C. Lin, A Study on the Hall–Petch Relationship and Grain Growth Kinetics in FCC-Structured High/Medium Entropy Alloys, Entropy. 21 (2019) 297. https://doi.org/10.3390/e21030297.

[201] H. Mehrer, Diffusion in Solids, Springer, Berlin, Heidelberg, 2007. https://doi.org/10.1007/978-3-540-71488-0.

[202] K. Ming, L. Li, Z. Li, X. Bi, J. Wang, Grain boundary decohesion by nanoclustering Ni and Cr separately in CrMnFeCoNi high-entropy alloys, Sci. Adv. 5 (2019) eaay0639. https://doi.org/10.1126/sciadv.aay0639.

[203] Y.J. Li, A. Kostka, A. Savan, A. Ludwig, Phase decomposition in a nanocrystalline CrCoNi alloy, Scr. Mater. 188 (2020) 259–263.

https://doi.org/10.1016/j.scriptamat.2020.07.054.

[204] R.W. Cahn, A new theory of recrystallization nuclei, Proc. Phys. Soc. Sect. A. 63 (1950) 323–336. https://doi.org/10.1088/0370-1298/63/4/302.

[205] T. Yu, N. Hansen, X. Huang, Linking recovery and recrystallization through triple junction motion in aluminum cold rolled to a large strain, Acta Mater. 61 (2013) 6577–6586. https://doi.org/10.1016/j.actamat.2013.07.040.

[206] K. Tanaka, T. Teramoto, R. Ito, Monocrystalline elastic constants of fcc-CrMnFeCoNi high entropy alloy, in: MRS Adv., Materials Research Society, 2017: pp. 1429–1434. https://doi.org/10.1557/adv.2017.76.

[207] K. Jin, Y.F. Gao, H. Bei, Intrinsic properties and strengthening mechanism of monocrystalline Ni-containing ternary concentrated solid solutions, Mater. Sci. Eng. A. 695 (2017) 74–79. https://doi.org/10.1016/j.msea.2017.04.003.

[208] M. Vaidya, K.G. Pradeep, B.S. Murty, G. Wilde, S. V. Divinski, Radioactive isotopes reveal a non sluggish kinetics of grain boundary diffusion in high entropy alloys, Sci. Rep. 7 (2017) 1–11. https://doi.org/10.1038/s41598-017-12551-9.

[209] I. Moravcik, H. Hadraba, L. Li, I. Dlouhy, D. Raabe, Z. Li, Yield strength increase of a CoCrNi medium entropy alloy by interstitial nitrogen doping at maintained ductility, Scr. Mater. 178 (2020) 391–397. https://doi.org/10.1016/j.scriptamat.2019.12.007.

[210] N.D. Stepanov, D.G. Shaysultanov, R.S. Chernichenko, N.Y. Yurchenko, S.V. Zherebtsov, M.A. Tikhonovsky, G.A. Salishchev, Effect of thermomechanical processing on microstructure and mechanical properties of the carbon-containing CoCrFeNiMn high entropy alloy, J. Alloys Compd. 693 (2017) 394–405. https://doi.org/10.1016/j.jallcom.2016.09.208.

[211] N.D. Stepanov, N.Y. Yurchenko, M.A. Tikhonovsky, G.A. Salishchev, Effect of carbon content and annealing on structure and hardness of the CoCrFeNiMn-based high entropy alloys, J. Alloys Compd. 687 (2016) 59–71. https://doi.org/10.1016/j.jallcom.2016.06.103.

[212] G.P.M. Leyson, L.G. Hector, W.A. Curtin, First-principles prediction of yield stress for basal slip in Mg-Al alloys, Acta Mater. 60 (2012) 5197–5203. https://doi.org/10.1016/j.actamat.2012.06.020.

[213] A. Tehranchi, B. Yin, W.A. Curtin, Solute strengthening of basal slip in Mg alloys,

Acta Mater. 151 (2018) 56–66. https://doi.org/10.1016/j.actamat.2018.02.056.

[214] A. Takeuchi, Mixing Entropy of Exact Equiatomic High-Entropy Alloys Formed into a Single Phase, (2020) 1–10. https://doi.org/10.2320/matertrans.MT-M2020141.

[215] A. Takeuchi, K. Amiya, T. Wada, K. Yubuta, Dual HCP structures formed in senary ScYLaTiZrHf multi-principal-element alloy, Intermetallics. 69 (2016) 103–109. https://doi.org/10.1016/j.intermet.2015.10.022.

[216] Y. Bu, Z. Li, J. Liu, H. Wang, D. Raabe, W. Yang, Nonbasal Slip Systems Enable a Strong and Ductile Hexagonal-Close-Packed High-Entropy Phase, Phys. Rev. Lett. 122 (2019) 075502. https://doi.org/10.1103/PhysRevLett.122.075502.

[217] A. Sarkar, B. Breitung, H. Hahn, High entropy oxides: The role of entropy, enthalpy and synergy, Scr. Mater. 187 (2020) 43–48. https://doi.org/10.1016/j.scriptamat.2020.05.019.

[218] Z. Zhang, M.M. Mao, J. Wang, B. Gludovatz, Z. Zhang, S.X. Mao, E.P. George, Q. Yu, R.O. Ritchie, Nanoscale origins of the damage tolerance of the high-entropy alloy CrMnFeCoNi., Nat. Commun. 6 (2015) 10143. https://doi.org/10.1038/ncomms10143.

Acknowledgment

My life as a graduate student has been supported by a countless number of people. First of all, my deepest appreciation goes to my supervisor, Prof. **Nobuhiro Tsuji** of Kyoto University for his excellent scientific guidance, great insight, and for giving me many chances to train myself as an independent researcher. Prof. **Haruyuki Inui** and Prof. **Hideyuki Yasuda** of Kyoto University is preferentially acknowledged for evaluating my works as thesis committee members. I would like to thank Dr. **Akinobu Shibata** of the National Institute of Materials Science, Japan, Prof. **Si Gao**, Prof. **Yu Bai**, and Prof. **Myeong-Hoem Park** of Kyoto University for the valuable discussion and patient assistance in my daily life.

Most of the alloy ingots used in this study were fabricated with the technical help of Prof. **Hideyuki Yasuda**, Prof. **Kohei Morishita**, Prof. **Taka Narumi**, Mr. **Keizo Ono**, and Mr. **Naoki Sei** of Kyoto University. The contents of Chapter 2 are mainly based on the discussion with Prof. **William A. Curtin** and Dr. **Binglun Yin** of École Polytechnique Fédérale de Lausanne (EFPL), Switzerland. I stayed in the Risø campus of Technical University of Denmark (DTU), Denmark, from Nov. 2018 to Mar. 2019 as a side prize of Mazume Research Encouragement Prize, Kyoto University, and studied with the guidance and help of Dr. **Xiaoxu Huang**, Dr. **Niels Hansen**, Prof. **Dorte Juul Jensen**, Dr. **Tianbo Yu**, and Ms. **Gitte Christiansen**. Chapter 3 is mainly based on the results I obtained there. In addition, the experiments in Chapter 3 were performed with the technical assistance of Prof. **Guilin Wu**, Prof. **Zongqiang Feng**, and Mr. **Rui Fu** of Chongqing University, China, Prof. **Mitsuhiro Murayama** of Virginia Polytechnic Institute and State University, USA, Mr. **Akira Yasuhara** of JEOL Ltd., Japan, Dr. **Masugu Sato** of Japan Synchrotron Radiation Research Institute, Japan, and Prof. **Hiroki Adachi** of the University of Hyogo, Japan. Chapter 4 was the summary of the collaborative work with Prof. **Nokeun Park** of Yeungnam University, South Korea, and Prof. **Tomotsugu Shimokawa**, Prof. **Tomoaki Niiyama**, and Mr. **Kohei Shiotani** of Kanazawa University, Japan. All of their supports are greatly and deeply appreciated.

I would like to express my sincerest appreciation to all of my other collaborators for the fruitful discussion, collaboration, and cooperation: Prof. **Hideki Araki**, Prof. **Masataka Mizuno**, Prof.

Jan. 2021 *Shuhei Yoshida*

List of related publications, presentations, and achievements

Peer-reviewed research articles

1) **Shuhei Yoshida**, Tilak Bhattacharjee, Yu Bai, Nobuhiro Tsuji*: Friction Stress and Hall-Petch Relationship in CoCrNi Equi-Atomic Medium Entropy Alloy Processed by Severe Plastic Deformation and Subsequent Annealing, *Scripta Materialia* **134**, pp. 33 - 36 (2017). [DOI: 10.1016/j.scriptamat.2017.02.042]
2) **Shuhei Yoshida***, Takuto Ikeuchi, Tilak Bhattacharjee, Yu Bai, Akinobu Shibata, Nobuhiro Tsuji: Effect of Elemental Combination on Friction Stress and Hall-Petch Relationship in Face-Centered Cubic High / Medium Entropy Alloys, *Acta Materialia* **171**, pp. 201-215 (2019). [DOI: 10.1016/j.actamat.2019.04.017]
3) **Shuhei Yoshida***, Takuto Ikeuchi, Yu Bai, Akinobu Shibata, Niels Hansen, Xiaoxu Huang, Nobuhiro Tsuji: Deformation microstructures and strength of face-centered cubic high/medium entropy alloys, *40th Risø International Symposium on Materials Science, IOP Conference Series: Materials Science and Engineering* **580**, p. 012053 (2019). [DOI: 10.1088/1757-899X/580/1/012053]
4) **Shuhei Yoshida***, Takuto Ikeuchi, Yu Bai, Nobuhiro Tsuji: Effect of Cobalt-Content on Mechanical Properties of Non-Equiatomic Co-Cr-Ni Medium Entropy Alloys, *Materials Transactions* **61**, 4, pp. 587 - 595 (2020). [DOI: 10.2320/matertrans.MT-MK2019004]
5) Binglun Yin*, **Shuhei Yoshida**, Nobuhiro Tsuji, William Curtin: Yield strength and misfit volumes of NiCoCr and implications for short-range-order, *Nature Communications* **11**, p. 2507 (2020). [DOI: 10.1038/s41467-020-16083-1]

Reviews, overviews, and book chapters

1) 辻 伸泰, 朴 魯謹, 李 翔, Rajeshwar Reddy Eleti, 吉田 周平, Tilak Bhattacharjee, 白 玉, Pinaki Prasad Bhattacharjee, 黒川 修: ハイエントロピー合金における ミクロ組織制御の可能性, まてりあ 57, Vol. 7, pp. 317 - 322 (2018). [DOI: 10.2320/materia.57.317]
2) 吉田 周平, 池内 琢人, BHATTACHARJEE Tilak, BAI Yu, 柴田 曉伸, 辻 伸泰 *: ハイエントロピー合金の結晶粒超微細化, 粉体および粉末冶金 67, 3, pp. 113-120 (2020). [DOI: 10.2497/jjspm.67.113]
3) 吉田 周平, 辻 伸泰: 第 5 章プロセッシングと組織制御 5.4.2 完全再結晶超 微細粒組織と力学特性 (pp.205-212), 「ハイエントロピー合金 〜カクテル 効果が生み出す多彩な新物性」乾 晴行 編著, 内田老鶴圃 (2020), ISBN: 978-4-7536-5137-5.

International conferences (Peer-reviewed)

1) **<u>Shuhei Yoshida</u>**, Tilak Bhattacharjee, Yu Bai, Kazuki Sugita, Masataka Mizuno, Hideki Araki, Nobuhiro Tsuji: Positron Annihilation Study on Equiatomic Multicomponent Alloys (L-105), 2017 TMS Annual Meeting and Exhibition, San Diego, USA (2017-02-28) (Poster).

2) **<u>Shuhei Yoshida</u>**, Tilak Bhattacharjee, Yu Bai, Nobuhiro Tsuji: Effect of Elemental Combination on Friction Stress and Hall-Petch Relationship in Medium Entropy Alloys Processed by Severe Plastic Deformation and Subsequent Annealing (B5-O30-015), The 15th International Conference on Advanced Materials (IUMRS-ICAM 2017), Kyoto, Japan (2017-08-30) (Oral).

3) **<u>Shuhei Yoshida</u>**, Tilak Bhattacharjee, Yu Bai, Nobuhiro Tsuji: Effect of Elemental Combination on Lattice Friction and Hall-Petch Relationship in High / Medium Entropy Alloys Processed by Severe Plastic Deformation and Subsequent Annealing (7C-E3-03), JSPM International Conference on Powder and Powder Metallurgy ~ 60th Anniversary ~ (JSPMIC2017), Kyoto, Japan (2017-11-07) (Oral).

4) **<u>Shuhei Yoshida</u>**, Takuto Ikeuchi, Tilak Bhattacharjee, Yu Bai, Akinobu Shibata, Nobuhiro Tsuji: Effect of Elemental Combination on Friction Stress and Hall-Petch Relationship in Face-Centered Cubic High / Medium Entropy Alloys, 18th International Conference on the Strength of Materials (ICSMA-18), Ohio, USA (2018-07-18) (Oral).

5) Nobuhiro Tsuji, Nokeun Park, Tilak Bhattacharjee, **<u>Shuhei Yoshida</u>**, Rajeshwar Eleti, Yu Bai, Shu Kurokawa, Pinaki Bhattacharjee: Microstructure Control and Resultant Change in Mechanical Properties in High Entropy Alloys, 2018 MRS Fall Meeting, Boston, USA (2018-11-26) (Oral) (**Invited**).

6) Takuto Ikeuchi, **<u>Shuhei Yoshida</u>**, Yu Bai, Nobuhiro Tsuji: Effect of Co-contents on mechanical properties of non-equiatomic Co-Cr-Ni Medium entropy alloys, The 2nd International Conference on High-Entropy Materials (ICHEM 2018), Jeju, Korea (2018-12-12) (Oral).

7) Nobuhiro Tsuji, Nokeun Park, Tilak Bhattacharjee, **<u>Shuhei Yoshida</u>**, Rajeshwar Eleti, Yu Bai, Shu Kurokawa, Pinaki Bhattacharjee: Possibility of Microstructure Control by Thermo-mechanically Controlled Processes in High Entropy Alloys, 2019 TMS Annual Meeting & Exhibition, San Antonio, USA (2019-03-11) (Oral) (**Invited**).

8) **<u>Shuhei Yoshida</u>**, Nokeun Park, Nobuhiro Tsuji: Recrystallization behavior of high / medium entropy alloys deformed by high pressure torsion and subsequently annealed (O111), 7th International Conference on Recrystallization and Grain Growth, Ghent, Belgium (2019-08-09) (Oral).

9) **<u>Shuhei Yoshida</u>**, Takuto Ikeuchi, Yu Bai, Akinobu Shibata, Niels Hansen, Xiaoxu Huang, Nobuhiro Tsuji: Deformation microstructures and strength of face-centered cubic high/medium entropy alloys (P12), The 40th Risø International Symposium on Materials Science: Metal Microstructures in 2D, 3D, and 4D, Roskilde, Denmark (2019-09-04) (Poster).

10) Binglun Yin, **<u>Shuhei Yoshida</u>**, Nobuhiro Tsuji, William Curtin: The Role of Short-range-order on Strengthening of NiCoCr: Theory and Experiments(P32),

The World Congress on High Entropy Alloys (HEA 2019), Seattle, USA (2019-11-18) (Poster).

11) **Shuhei Yoshida**, Genki Yamashita, Takuto Ikeuchi, Yu Bai, Akinobu Shibata, Nobuhiro Tsuji: Microstructural origin of high work-hardenability in ultrafine-grained CoCrNi medium entropy alloy (C1-O12-004), Materials Research Meeting 2019 (MRM2019), Yokohama, Japan (2019-12-12) (Oral).

Domestic conferences in Japan (Peer-reviewed)

1) 吉田 周平，BHATTACHARJEE Tilak，BAI Yu，辻 伸泰：巨大ひずみ加工による CoCrNi Medium Entropy Alloy の結晶粒微細化と機械的特性 (P48), 日本金属学会 2017 年春期(第 160 回)講演大会, Tokyo, Japan (2017-03-15) (Poster).

2) 吉田 周平，BHATTACHARJEE Tilak，BAI Yu，辻 伸泰：High / Medium Entropy Alloy における Friction stress とその合金元素依存性 (534)，日本金属学会 2017 年秋期(第 161 回)講演大会, Sapporo, Japan (2017-09-07) (Oral).

3) 池内 琢人，吉田 周平，BHATTACHARJEE Tilak，BAI Yu，辻 伸泰：Co-Cr-Ni Medium Entropy Alloy の力学的特性に及ぼす Co 量の影響 (P89)，日本金属学会 2018 年春期(第 162 回)講演大会, Chiba, Japan (2018-03-19) (Poster).

4) 吉田 周平，池内 琢人，BHATTACHARJEE Tilak，BAI Yu，柴田 曉伸，辻 伸泰：High / Medium entropy alloy の摩擦応力に及ぼす元素の組合せの影響 (S2. 20)，S2 ハイエントロピー合金の材料科学，日本金属学会 2018 年秋期(第 163 回) 講演大会, Sendai, Japan (2018-09-20) (Oral).

5) 辻 伸泰, 吉田 周平, Bai Yu: ハイエントロピー合金の結晶粒超微細化 (3-21), 粉体粉末冶金協会 2019 年度春季大会 (第 123 回講演大会), Tokyo, Japan (2019-06-05) (Oral) (**Invited**).

6) 吉田 周平，朴 魯謹，辻 伸泰：完全再結晶超微細粒組織を有する高・中エントロピー合金の作製とその力学特性 (S1.10), S1 ハイエントロピー合金の材料科学Ⅱ, 日本金属学会 2019 年秋期(第 165 回)講演大会, Okayama, Japan (2019-09-11) (Oral).

7) 池内 琢人，吉田 周平，BAI Yu，柴田 曉伸，辻 伸泰：Co-Cr-Ni Medium Entropy Alloy の室温変形挙動と積層欠陥エネルギー，摩擦応力の関係 (S1.2), S1 ハイエントロピー合金の材料科学Ⅱ, 日本金属学会 2019 年秋期 (第 165 回)講演大会, Okayama, Japan (2019-09-11) (Oral).

8) 吉田 周平, Fu Rui, Gong Wu, 池内 琢人, Bai Yu, 柴田 曉伸, Feng Zongqiang, Wu Guilin, Hansen Niels, Huang Xiaoxu,·辻 伸泰: 高・中エントロピー合金における変形組織の方位依存性と力学特性の関係(S1.3), 日本金属学会 2020 年春期(第 166 回)講演大会, Tokyo, Japan (2020-03-17) (Oral).

9) 山崎 直人, 吉田 周平, Bai Yu, Bhattacharjee Pinaki, 辻 伸泰: $Co_{20}Cr_{40}Ni_{40}$ Medium Entropy Alloy における圧延変形組織の発達とその結晶方位依存性

(P30), 日本金属学会 2020 年春期(第 166 回)講演大会, Tokyo, Japan (2020-03-17) (Poster).

10) 山崎 直人, <u>吉田 周平</u>, Bai Yu, Pinaki Prasad Bhattacharjee, 辻 伸泰: FCC 単相 Medium Entropy Alloy における圧延変形組織の発達とその結晶方位依存性, 日本金属学会 2020 年秋季(第 167 回)講演大会 (Online conference), Japan (2020-09) (Oral).

Other research meetings (Non-peer-reviewed)

1) <u>吉田 周平</u>, Bhattacharjee Tilak, Bai Yu, 辻 伸泰: 高/中エントロピー合金における Friction stress とその組成依存性, 高温変形の組織ダイナミクス研究会「平成 29 年度 夏の学校」, Gamagori, Japan (2017-09-20) (Oral).

2) <u>吉田 周平</u>, 池内 琢人, BHATTACHARJEE Tilak, BAI Yu, 柴田 曉伸, 辻 伸泰 : 高・中エントロピー合金の摩擦応力と Hall-Petch 関係に及ぼす合金元素の影響, 高温変形の組織ダイナミクス研究会「平成 30 年度 夏の学校」, Saga, Japan (2018-09-06) (Oral).

3) <u>吉田 周平</u>, 山崎 直人, 池内 琢人, BAI Yu, 柴田 曉伸, Pinaki Prasad Bhattacharjee, Niels Hansen, Xiaoxu Huang, 辻 伸泰: 高・中エントロピー合金における変形組織発達, 高温変形の組織ダイナミクス研究会「2019 年度 夏の学校」, Kanazawa, Japan (2019-09-23) (Oral).

Achievements

1) 日本学生支援機構大学院第一種奨学金 特に優れた業績による返還免除 (全額免除) (2018, 05)
2) Mazume Research Encouragement Prize, Kyoto University (2018, 07)
3) Yoshida Research Encouragement Prize, Kyoto University (2020, 06)